Australian Government
Geoscience Australia

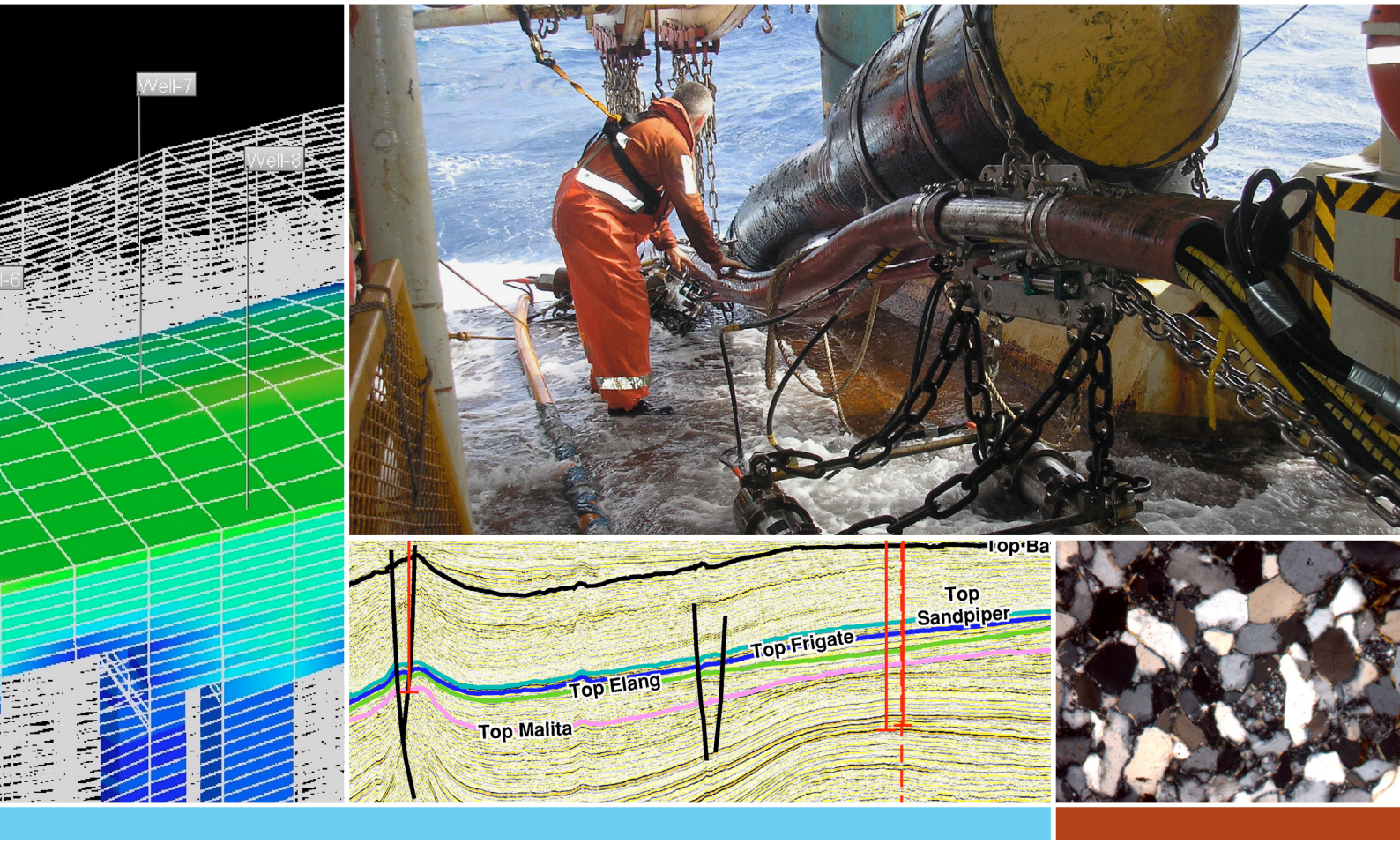

Record 2014/11 | **GeoCat** 76510

Regional assessment of the CO_2 storage potential of the Mesozoic succession in the Petrel Sub-basin, Northern Territory, Australia

Summary report

Christopher Consoli, Karen Higgins, Diane Jorgensen, Kamal Khider, David Lescinsky, Robbie Morris and Victor Nguyen

Regional assessment of the CO_2 storage potential of the Mesozoic succession in the Petrel Sub-basin, Northern Territory, Australia

Summary report

GEOSCIENCE AUSTRALIA
RECORD 2014/11

Christopher Consoli, Karen Higgins, Diane Jorgensen, Kamal Khider, David Lescinsky, Robbie Morris and Victor Nguyen

Australian Government
Geoscience Australia

Department of Industry
Minister for Industry: The Hon Ian Macfarlane MP
Parliamentary Secretary: The Hon Bob Baldwin MP
Secretary: Ms Glenys Beauchamp PSM

Geoscience Australia
Chief Executive Officer: Dr Chris Pigram
This paper is published with the permission of the CEO, Geoscience Australia

ISSN 2201-702X (PDF)

ISBN 978-1-925124-00-2 (PDF)

GeoCat 76510

Bibliographic reference: Consoli, C.P., Higgins, K., Jorgensen, D., Khider, K., Lescinsky, D. T., Morris, R. and Nguyen, V., 2013, *Regional assessment of the CO_2 storage potential of the Mesozoic succession in the Petrel Sub-basin, Northern Territory, Australia: summary report*. Record 2014/11. Geoscience Australia, Canberra. http://dx.doi.org/10.11636/Record.2014.011

Contents

Summary

The Petrel Sub-basin is suitable for the geological storage of carbon dioxide (CO_2). Acquisition of pre-competitive data and a comprehensive analysis of the sub-basin geology identified two Mesozoic reservoir-seal pairs over the central axis and eastern flank of the sub-basin suitable for CO_2 storage.

The oldest reservoir-seal pair includes the Jurassic reservoir, comprising the Plover and Elang formations and the lower Frigate Shale, sealed by the Jurassic upper Frigate Shale. The youngest reservoir-seal pair comprises the Cretaceous Sandpiper Sandstone reservoir and the Cretaceous Bathurst Island Group regional seal.

Geomechanical analysis revealed that fault reactivation in the reservoir-seal pairs could result from changes in reservoir pore pressure, however the risk of failure along identified faults within the areas of highest potential for CO_2 injection and storage is low. Outside this area, fault reactivation risk is increased for high angle faults orientated E-W and for shallow faults on the margins of the sub-basin.

Dynamic reservoir simulations indicate that predicted CO_2 emissions from the region of 14 million tonnes per year by 2020 can be injected into the main Jurassic reservoir. During 30 years of injection the simulated plume migrated only 5 km and after the cessation of injection, migration slowed to around 12 m per year. After 100 years, over 50% of the CO_2 was permanently stored through residual and dissolution trapping. CO_2 injection scenarios rely on migration-assisted storage, with long migration paths (50-70 km) in the two reservoirs. The two reservoirs have a large total effective CO_2 storage capacity of 15.9 gigatonnes (300 trillion cubic feet; P50).

The combined results of this study were used to identify an area highly suitable for CO_2 storage in the centre of the sub-basin, making up 27% of the total study area and extending between 50-70 km to the north, east and south of the Petrel gas field.

Key datasets from the study include:

- 4091 line kilometres of 2D seismic reflection data (seismic survey GA336). These data were acquired over a data poor area in the southeast, a critical location for understanding the CO_2 storage.
- Comprehensive suite of multibeam sonar, sub-bottom profiler, seabed samples, and seabed video and stills for targeted environments. These data were collected in two areas during a marine reconnaissance survey (SOL5463/GA335) undertaken to investigate evidence for potential leakage from the deep basin to the seabed to asses seal quality. No evidence of deep fluid leakage was found. The data also provided an environmental baseline for this part of Joseph Bonaparte Gulf.

All datasets collected as part of this study are publicly available and can be obtained from Geoscience Australia (www.ga.gov.au).

1 Introduction

The capture and geological storage of carbon dioxide (CO_2) is one of a suite of technologies the Australian Government has identified to assist in reducing Australia's greenhouse gas emissions. Defining the national geological storage potential requires a detailed understanding of Australia's sedimentary basins and their pore space. Furthermore, suitable storage sites are a prerequisite to the deployment of large-scale commercial carbon capture and storage (CCS) technologies. This report provides a summary of the comprehensive analyses undertaken as part of a Petrel Sub-basin CO_2 storage study. It also provides an evaluation of the CO_2 geological storage potential of the sub-basin.

1.1 Project Details

The Australian Government, through the Department of Industry, has supported Geoscience Australia in undertaking a series of regional-scale, geological studies to assess the CO_2 storage potential of sedimentary basins, including the Petrel Sub-basin, northern Australia (Figure 1.1). The studies form part of the National Low Emissions Coal Initiative designed to accelerate the development of CO_2 transport and storage infrastructure near the sources of major energy and industrial emissions. The Petrel Sub-basin was identified as a high-priority region for a future pre-competitive work program by the Carbon Storage Taskforce, who published the National Carbon Mapping and Infrastructure Plan in 2009 (Carbon Storage Taskforce, 2009). The Carbon Storage Taskforce also recommended release of greenhouse gas assessment permits. Two permits were released over the Petrel Sub-basin in 2009 (Figure 1.1). This study provides pre-competitive data and an assessment of the Petrel Sub-basin for CO_2 geological storage to support the decision making process of the Australian Government. It also assists both government and industry to ultimately assess the geological storage potential of Australia's offshore basins.

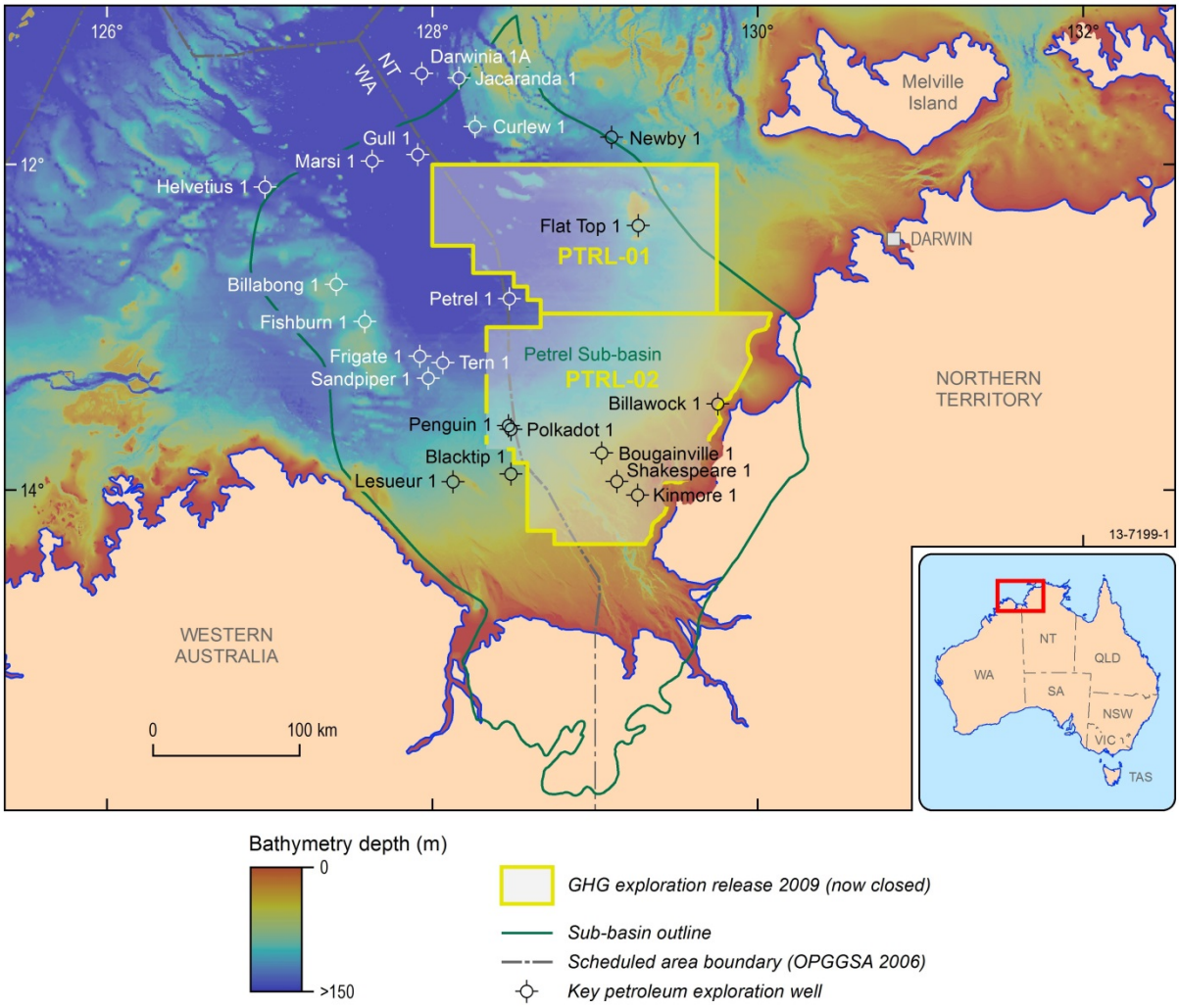

Figure 1.1 Location map showing study region. PTRL-01 and PTRL-02 refer to the two exploration blocks released in 2009 under the Offshore Petroleum and Greenhouse Gas Storage Act, 2006 (now closed).

1.2 Carbon Capture and Storage

This section provides a brief outline of CCS technologies. More detailed information can be found in Cook (2012). In the CCS technology chain, CO_2 emissions are captured as part of a CO_2 separation process associated with the production of energy for power, or other products, including cement and steel. The technology behind CO_2 capture is widely used today during the production of sales gas, which requires CO_2 to be removed. The next step in the CCS process is transportation of compressed or uncompressed CO_2 via pipeline, ship or road / rail tanker. Geological storage of CO_2 in the subsurface is the final stage of the CCS chain. Storage sites are typically composed of reservoirs with good porosity and permeability and an impermeable trap/seal. Major targets for large-scale commercial CCS projects include depleted oil or gas fields and formations containing non-potable saline water.

Operational CCS projects and the use of CO_2 for enhanced oil and gas recovery demonstrate that the geological storage of CO_2 is an established, technologically achievable process. An important component of an operational CCS storage site involves measurement, monitoring and verification (MMV) that includes quantifying the amount of CO_2 sequestered and verifying that the movement of

CO_2 sequestered and verifying that the movement of CO_2 is within pre-injection predictions. MMV is crucial for accounting, safety and community assurance and can include geophysical techniques, as well as direct fluid and pressure measurements.

As with all emerging technologies, the development of large scale CCS into a commercial reality has major hurdles, predominantly surrounding the up-scaling of each of the technologies and a lack of economic incentives. Nevertheless, worldwide CCS projects have been operational since the mid-1990s, with eight large-scale integrated projects in operation and another eight under construction (Global CCS Institute, 2013).

1.3 CO_2 Properties and Subsurface Behaviour

CO_2 exists as a gas at ambient pressure and temperature on the Earth's surface. In the subsurface, CO_2 becomes a supercritical gas due to an increase in temperature (above 31.1 °C) and pressure (above 7.39 megapascal, MPa;

Figure 1.2). The depth of transition from one state to another can vary between 600 and 1000 km, depending on the geothermal gradient and reservoir pressure, but is commonly considered to be around 800 m (Holloway, 2007; Figure 1.2). For example, in the Petrel Sub-basin, the geothermal gradient is relatively high (30.5 °C/km and 25 °C at the surface) and therefore the CO_2 critical point is likely to be at around 750 m. Supercritical CO_2 has a higher density and decreased volume relative to the gas phase, and during geological storage has higher injection and storage efficiencies in the reservoir. Since supercritical CO_2 is less dense than water or brine, and only slightly miscible with water, it is relatively buoyant.

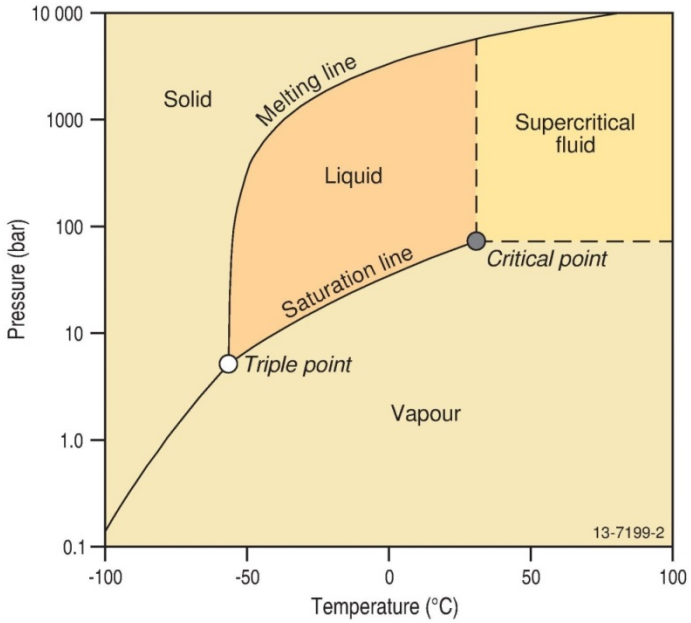

Figure 1.2 CO_2 phase diagram.

The trapping of CO_2 in a saline formation is a complex interplay of capillary, viscous, and buoyancy forces that evolve over time (Figure 1.3). There are four main trapping mechanisms and all four occur in a typical reservoir injection scenario, as follows:

1. *Structural or stratigraphic trapping*. Initially on injection into the storage reservoir the CO_2 rises due to buoyancy until it reaches an impermeable barrier (i.e., a seal), it then moves laterally up dip until it is trapped by either structural or stratigraphic closures.
2. *Dissolution trapping*. In saline aquifers, CO_2 dissolves into the saline water (brine) causing it to become denser and sink, exposing the supercritical CO_2 to additional brine.
3. *Residual or dissolution trapping*. As the CO_2 plume moves through the formation, residual trapping occurs in the saline formation pores due to capillary forces (hysteresis). Residual and dissolution trapping are the most important trapping mechanisms in CO_2 storage in saline aquifers (Szulczewski et al., 2012).
4. *Mineral trapping*. Over very long timeframes (thousands of years), geochemical reactions between the CO_2, brine and reservoir minerals result in the precipitation of minerals through interaction with the rock matrix.

There are three types of geological storage plays that rely on a porous medium (reservoir) paired with a non-porous medium (seal). These include structural, stratigraphic and migration-assisted storage (MAS; Figure 1.3b). In structural storage, the reservoir is within a geological feature such as a sealed anticline, or adjacent to an impermeable fault or impermeable geobody (e.g. salt diapir) that provides the storage site. Stratigraphic storage occurs when there is reservoir pinch-out between two impermeable layers. In MAS, the reservoir is an open system where an extensive, competent sealing unit overlies the reservoir and the processes of residual gas saturation and dissolution result in permanent storage. Due to the longevity of the trapping mechanisms and the large-scale CO_2 footprint, a robust CO_2 geological storage prospectivity assessment should include a detailed understanding of the reservoirs and seals in a prospective basin at a regional scale.

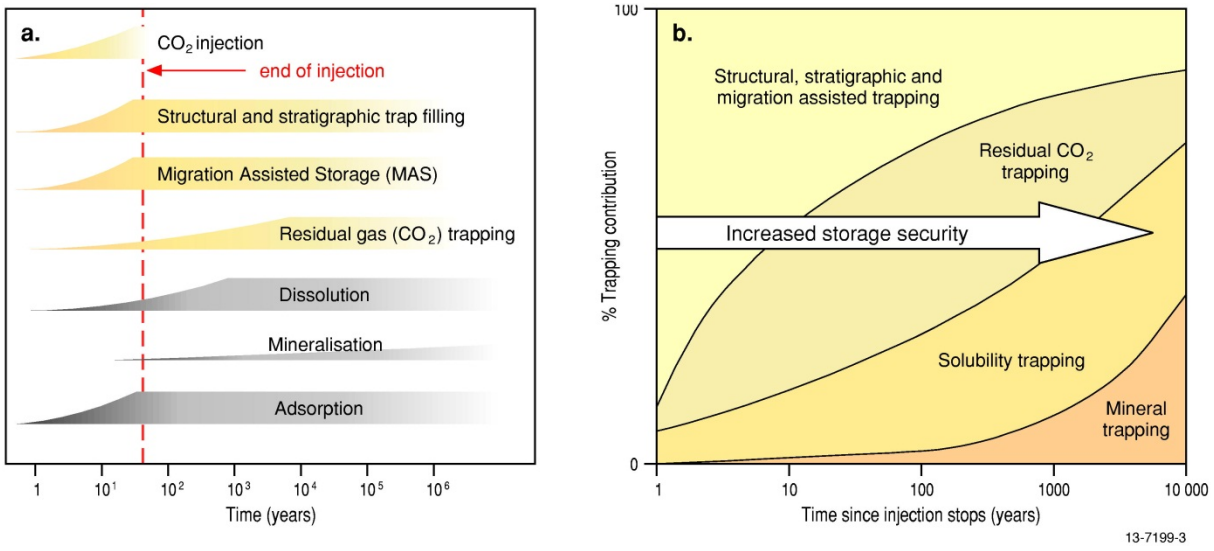

Figure 1.3 Time dependency of processes involved in CO_2 geological storage (a) operating time frame; and (b) storage security (modified from IPCC, 2005 and Bradshaw et al., 2009).

1.4 Aim

The principal aim of this study is to assess the CO_2 geological storage potential of the Petrel Sub-basin (Figure 1.4). This was achieved through the completion of four major activities:

1. Acquisition and analysis of new pre-competitive data, including 2D seismic data and seabed information.
2. Key formation mapping and characterisation.
3. Assessment of potential seal containment.
4. Assessment of reservoir injectivity and capacity.

An initial assessment and literature review identified the Mesozoic strata comprising the Malita and Plover Formations (Troughton Group); the Elang Formation, the Frigate Shale and the Sandpiper Sandstone (Flamingo Group) and the Echuca, Darwin and Wangarlu formations (Bathurst Island Group) as the focus of this study (Figure 1.5). These Mesozoic strata were selected as there were no current overlaps with hydrocarbon resources and they comprise a series of good reservoirs and seals, as defined by the Carbon Storage Taskforce (2009).

Figure 1.4 Location of the study area, including the focus area which roughly equates to the extent of the geological model. It also shows the reservoir simulation model area, key wells and major pre-competitive data acquired as part of this study.

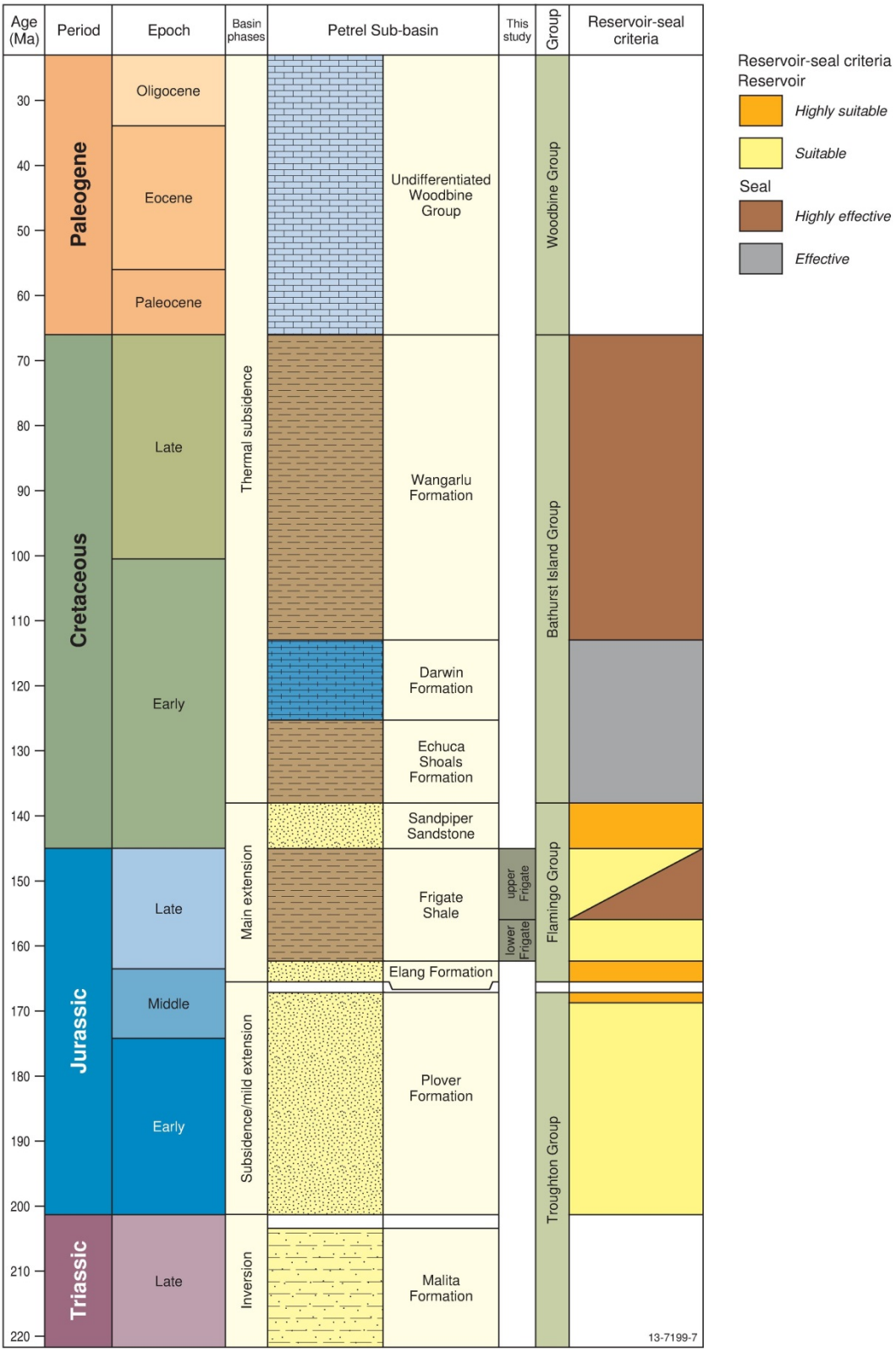

Figure 1.5 Mesozoic and Cenozoic stratigraphy of the offshore Petrel Sub-basin based on the Bonaparte Basin Biozonation and Stratigraphy Chart 33 (Nicoll et al., 2009). Geologic Time Scale after Gradstein et al. (2012). Basin phases specific to the Petrel Sub- basin after Colwell and Kennard (1996). The seismic horizons and reservoir and seal characteristics were completed in this study. Note: the formally defined Frigate Shale is divided informally into the upper Frigate Shale and lower Frigate Shale in this study.

2 Regional Geology

The Petrel Sub-basin forms the southern part of the Bonaparte Basin. The Bonaparte Basin is the northernmost depocentre of the Westralian Superbasin on the North West Shelf that also includes the Browse, Roebuck and Carnarvon basins (Bradshaw et al., 1998; Longley et al., 2002). The Bonaparte Basin is located mainly offshore covering 270,000 km^2 (Figure 2.1). It is partly located in the Joseph Bonaparte Gulf, west of the city of Darwin, and straddles both the jurisdictions of the Northern Territory and Western Australia, extending north to Australia's territorial border with Indonesia and Timor-Leste. The basin merges with the Money Shoal Basin to the northeast and joins with the Browse Basin along the southwest margin.

The Bonaparte Basin has been the focus of numerous tectonostratigraphic studies (Gunn, 1988; Lee and Gunn, 1988; Veevers, 1988; Pattilo and Nicholls, 1990; O'Brien, 1993; AGSO, 1994; Ballie et al., 1994; Colwell and Kennard, 1996; Whittam et al., 1996; Borel and Stampfli, 2002; Kennard et al., 2002; and Longley et al., 2002). It is outside the scope of this report to provide a detailed summary of them all. Instead we focus on a detailed summary of the tectonic and stratigraphic evolution of the Petrel Sub-basin (Figure 2.2).

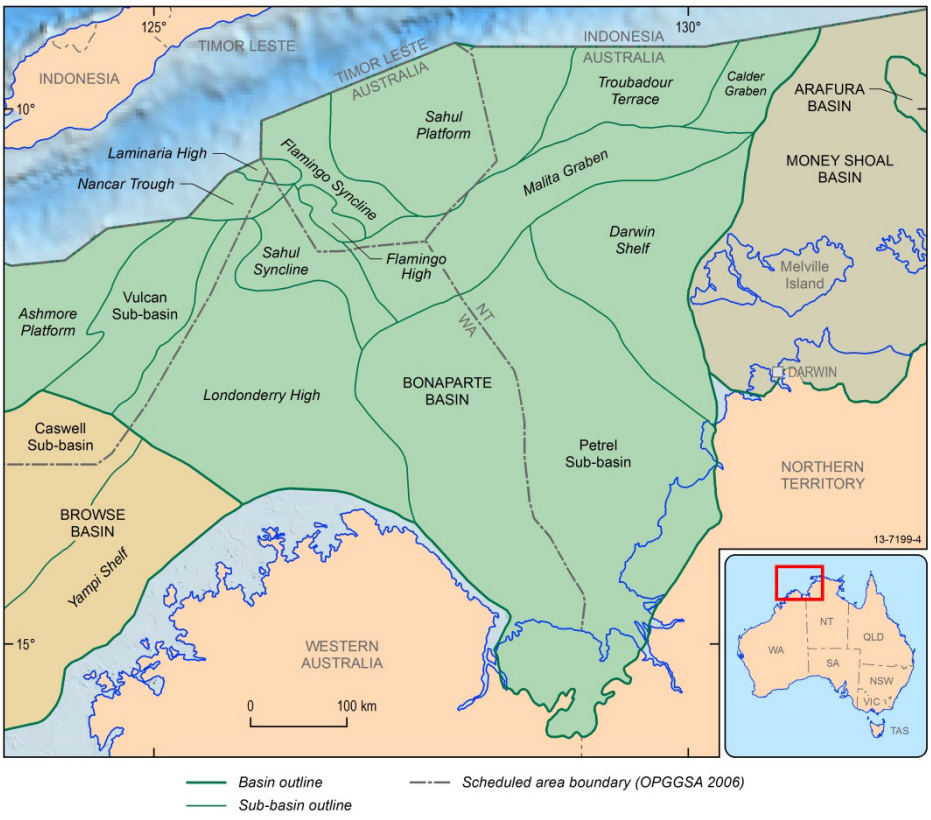

Figure 2.1 Map of the Bonaparte Basin, including the major tectonic components and adjoining offshore sedimentary basins.

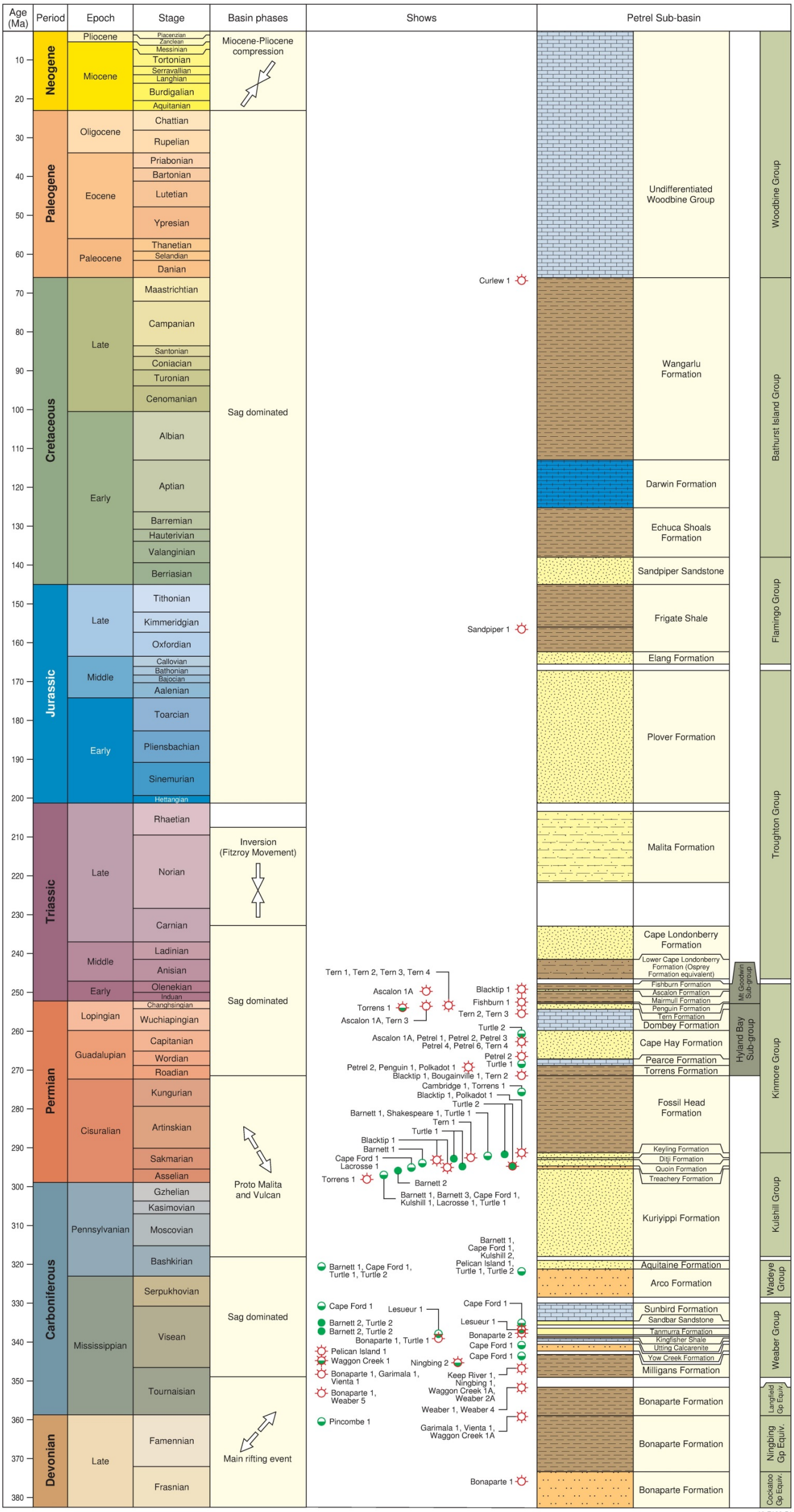

Figure 2.2 Stratigraphy of the southern Bonaparte Basin (Petrel Sub-basin) based on the Bonaparte Basin Biozonation and Stratigraphy Chart 33 (Nicoll et al., 2009). Geologic Time Scale after Gradstein et al. (2012). Basin phases specific to the Petrel Sub-basin after O'Brien (1993), Colwell and Kennard (1996), Borel and Stampfli (2002) and Frankowicz and McClay (2010).

This page has intentionally been left blank.

2.1 Tectonic Evolution

The Petrel Sub-basin dominates the southern part of the Bonaparte Basin, extending from onshore to offshore in water depths up to 100 m (Figure 1.1). The sub-basin is bounded by the Londonderry High / Berkley Platform in the west, the Malita Graben to the north, and the Darwin Shelf / Moyle Platform to the east (Figure 2.3). The sub-basin forms an asymmetric, northwest trending syncline and the eastern and western faulted margins converge to the south (Figure 2.3).

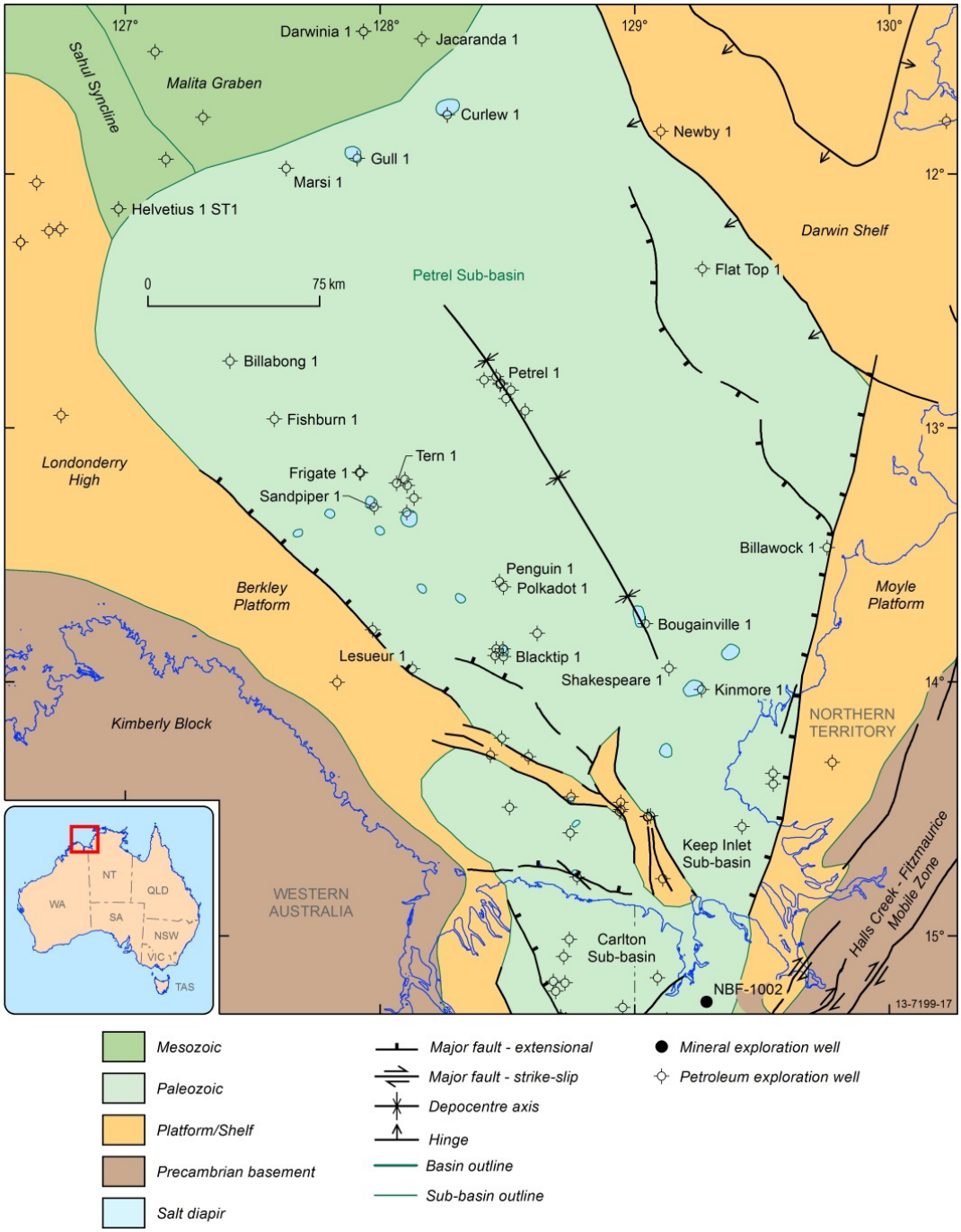

Figure 2.3 Structural elements of the Petrel Sub-basin (after Colwell and Kennard, 1996).

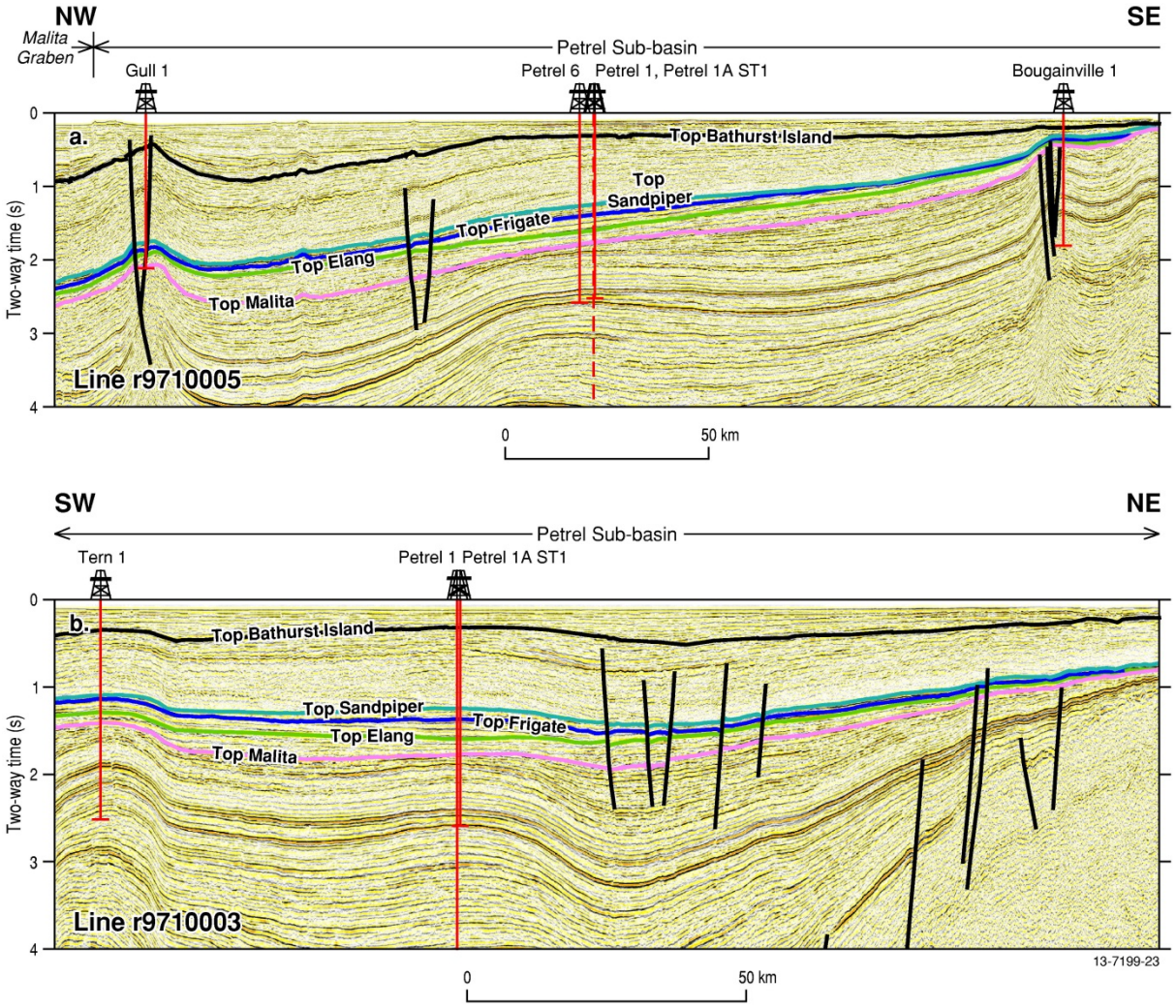

Figure 2.4 Geoscience Australia seismic lines (a) r9710005 (also known as AGSO Regional 2D seismic line 100/5) and (b) r9710003 (AGSO Regional 2D seismic line 100/3). Seismic lines showing the seismic horizons and tectonic faults interpreted in this study, as well as the general trend of the Petrel Sub-basin including effects of salt diapirism. See Figure 4.4 for the location of the seismic lines.

The tectonic evolution of the Petrel Sub-basin has previously been discussed by Mory and Beere (1988), Mory (1990, 1991), O'Brien (1993), O'Brien et al. (1995), Colwell and Kennard (1996), Lemon and Barnes (1997), Goncharov et al. (1999), Mildren et al. (2000), Keep et al. (2002), Kennard et al. (2002), Baldwin et al. (2003), Frankowicz and McClay (2010) and Bourget et al. (2012). Below, we summarise the key findings from these previous studies:

- Late Devonian to Early Carboniferous northwest trending rifting related to the opening of the Neo-Tethys Ocean (Borel and Stampfli, 2002).
- Late Triassic to Early Jurassic major north–south to north-northwest–south-southeast compressional Fitzroy event, which reactivated faults and created a number of inversion features in the Petrel Sub-basin. This event is linked to the closure of the Paleo-Tethys (O'Brien, 1993; Borel and Stampfli, 2002; Kennard et al., 2002).
- A period of northwest directed extension associated with the break-up of Gondwana in the Middle Jurassic (Longely et al., 2002).

- Full continental breakup and cessation of rifting in the Valanginian (Colwell and Kennard, 1996).
- Thermal subsidence that persisted until the Cenozoic.
- The Miocene to Pliocene east-northeast directed collision of the Indo-Australian plate with the South East Asian microplates that resulted in regional compression, deformation and fault reactivation (Colwell and Kennard, 1996).

2.2 Stratigraphy

The stratigraphy of the Petrel Sub-basin has been described by Mory (1988, 1991), Messent et al. (1994), Blevin et al. (1996a, 1996b), Colwell and Kennard (1996), Gorter (1998), Lang and Gibson-Poole (2001), Cadman and Temple (2004), Gibson-Poole (2009), Gorter et al. (2009) and Nicoll et al. (2009). Figure 2.2 is a culmination of the findings from these studies and shows the major stratigraphic units and tectonic phases that have dominated the evolution of the sub-basin and the distribution of major reservoir and sealing units.

There is a regional northwest dip due to the northwest plunging synclinal axis (Figure 2.4). The sub-basin contains up to 15 km of Paleozoic to Mesozoic sediments, which thicken towards the northwest, with a relatively thin (several hundred metres) veneer of Cenozoic sediments. The oldest units identified in the offshore Bonaparte Basin are Late Devonian, although according to Mory (1991) Cambrian volcanic and sedimentary rocks are present onshore and probably extend offshore. Thick evaporate sequences were deposited from the Late Ordovician to Early Silurian, which were subsequently mobilised throughout the Phanerozoic resulting in several salt-induced structures and salt-withdrawal features.

Significant deposition occurred during the Paleozoic as a result of regional extension and subsequent subsidence. Fine-grained clastic and carbonate sediments were deposited in a shallow marine to non-marine setting during Late Devonian rifting forming the Cockatoo, Ningbing and Langfield groups. Throughout the Carboniferous, post-rift subsidence resulted in the deposition of thick sequences of marine, fluvial and deltaic sediments, defined as the Weaber and Wadeye groups. Late Carboniferous to Early Permian sediments were deposited during a largely sag-dominated regressive cycle and comprised thick, shallow marine, deltaic, and fluvial sediments of the Kulshill Group. In the Permian, thick transgressive sequences of marine mudstones and siltstones were deposited in a tidal shelf environment that was succeeded by shallow marine sandstones, mudstones, and carbonates of the Kinmore Group. The upper formation of the Kinmore Group is represented by a succession of transgressive marine shales and siltstones. The mudstones of the Kinmore Group form an extensive seal across the region that separates the Paleozoic and Mesozoic stratigraphic sequences in the Petrel Sub-basin.

A regressive sequence of deltaic to fluvial sediments defined as the Troughton Group was deposited across the sub-basin in the Early Triassic. A Late Triassic compressional event, the Fitzroy Movement, resulted in a major erosional event across the southern margins of the Petrel Sub-basin. The deposition of Upper Triassic to Lower Jurassic fluvio-deltaic sediments and localised red beds of the Troughton Group formed after this widespread tectonic event. Middle Jurassic sediments of the Troughton Group were deposited as a series of fluvial and deltaic sediments, with increasing shallow marine influence. The Callovian unconformity, which represents the initiation of the Mesozoic extensional regime, is preserved as an unconformity between the Troughton and Flamingo groups. The sediments of the Flamingo Group accumulated after the Callovian event. Basin-wide subsidence resulted in deposition of a sequence of deepening sediments, from fluvial-shallow marine fine- to coarse-grained clastic sediments in the lower units to predominantly open marine mudstones in the upper units.

The sand-rich lower Flamingo Group (Elang Formation), collectively with the Troughton Group sandstones (Plover Formation) form the major CO_2 storage reservoir for this study and are sealed by the mudstones of the upper Flamingo Group (Frigate Shale). The uppermost sequence of the Flamingo Group (Sandpiper Sandstone) represents a shallowing marine environment and resulted in the deposition of fluvial to shoreface environments and forms the second reservoir of this study. The cessation of the extensional event is marked by the Valanginian unconformity and the deposition of fine-grained clastics and carbonates. Collectively these sediments are defined as the Bathurst Island Group. These sediments were deposited after a widespread marine transgression over the Petrel Sub-basin. The Paleocene to Pliocene was dominated by progradational carbonates that were succeeded by fine-grained clastics and carbonates deposited in a passive continental margin setting.

2.3 Petroleum Potential

An understanding of the hydrocarbon history of the Petrel Sub-basin is important for assessing the potential for CO_2 storage because it provides insights into prospective formations for storage and capacity of the associated seals.

The Petrel Sub-basin is an established petroleum province. Offshore there are a several gas discoveries including the Petrel, Tern, Frigate and Blacktip gas fields and the Fishburn 1, Polkadot 1 and Penguin 1 wells (Figure 2.2; Figure 2.5). There are also significant oil accumulations identified in the south of the offshore Petrel Sub-basin. Currently, the Blacktip gas field is the only operating field.

The petroleum potential of the Bonaparte Basin, including the Petrel Sub-basin, has been the subject of many detailed studies (Loutit et al., 1996; McConachie et al., 1996; Colwell and Kennard, 1996; Miyazaki, 1997; Kennard et al., 2002; Barrett et al., 2003; Cadman and Temple, 2004; and Zhixin et al., 2012). These studies have revealed that, to date, all significant accumulations of hydrocarbons are restricted to two active petroleum systems: The Hyland Bay / Keyling-Hyland Bay petroleum system of the Kulshill and Kinmore groups, which occurs in the central Petrel Sub-basin, and the Milligans-Kuriyippi / Milligans petroleum system of the Weaber Group, which occurs in the southern Petrel Sub-basin. Below, we discuss the Hyland Bay / Keyling-Hyland Bay petroleum system as it is most relevant to this study.

Petroleum system modelling by Kennard et al. (2002) indicates that gas expulsion from the Early Permian Keyling Formation peaked in the Early Triassic with minor expulsion in the Late Triassic to Early Cretaceous. Expulsion from the Permian Hyland Bay Sub-group was limited to the northern Petrel Sub-basin and occurred from the Jurassic until the Cretaceous, peaking in mid-Late Cretaceous. Despite the expulsion history extending into the Mesozoic, no hydrocarbon accumulations have been found within the Mesozoic reservoirs. Kennard et al. (2002) attribute the failure of tested traps and potential Mesozoic plays to a lack of mature. These workers also suggest that poor reservoir quality or seal capacity, which are relevant to CO_2 storage, are unlikely reasons for a lack of hydrocarbon accumulations in the Mesozoic units.

Figure 2.5 Petrel Sub-basin gas fields and pipeline infrastructure including the hydrocarbon shows of the petroleum exploration wells. Key wells for petroleum exploration in the Petrel Sub-basin labelled.

3 Previous CO_2 Storage Studies

The Bonaparte Basin, and in particular the Petrel Sub-basin, was originally proposed as a potential location for CO_2 storage as part of the Australian Petroleum Cooperative Research Centre for Geological Disposal of Carbon Dioxide (GEODISC) Project during an Australian-wide assessment to identify Environmentally Sustainable Sites for CO_2 Injection (ESCCI) (Cook et al., 2000; Bradshaw and Rigg, 2001; Rigg et al., 2001). This four-year study firstly identified the CO_2 storage potential of suitable basins nation-wide by identifying storage sites and corresponding emission nodes. The basins/sub-basins were ranked on a national scale identifying potential ESSCIs with optimal geology and considered the existence of available infrastructure and proximity to major emission sources. During the first phase of the study (Project 1), GEODISC identified the Sandpiper Sandstone and Plover and Elang formations ESSCI plays in the offshore Petrel Sub-basin (Bradshaw et al., 2000) as highly suitable CO_2 geological storage plays. In all assessment elements (e.g., geology and infrastructure) these ESCCIs were ranked highly except for proximity to a major CO_2 source. The ongoing development of LNG processing proximal to the city of Darwin would now, under the GEODISC criteria, represent a significant source of CO_2 emissions. Although the entire sub-basin was evaluated, the final assessment, including the capacity estimation, focussed on the Sandpiper Sandstone and the Plover and Elang formations ESSCI plays within the Tern 1 anticline structural closure (Table 3.1).

*Table 3.1 Previous storage capacity estimates of the Petrel Sub-basin (Carbon Storage Taskforce, 2009). *Note: For Carbon Storage Taskforce (2009) assessment, the sub-basin was divided by the Western Australia and Northern Territory boundary, splitting it lengthwise. This method, used throughout the assessment enabled stakeholders to obtain a state and territory breakdown of emissions and storage capacity.*

Author	Scale/Formation	Storage Potential (Mt)	Methodology
Carbon Storage Taskforce (2009)	Basin scale; Plover and Elang formations and Sandpiper Sandstone.	55,300 (P50, best estimate)	Input data: Published datasets. Capacity method: DOE (2007); 4% of total pore volume, static CO_2 density and basin-specific static temperature and pressure.
Gibson-Poole (2009)	Formation scale; Plover and Elang formations; Sandpiper Sandstone.	193,464	Input data: geological model Capacity method: DOE (2007); 4% of total pore volume, static CO_2 density and basin-specific static temperature and pressure.
Lang and Gibson-Poole (2001)	Regional scale; Plover and Elang formations; Sandpiper Sandstone.	~4,919,462	Input data: geological model Capacity method: Total pore volume with static CO_2 density and basin-specific static temperature and pressure and assumed fill to spill.
Bradshaw et al. (2000)	Formation-scale; Plover and Elang formations; Sandpiper Sandstone.	~1288*	Input data: Published datasets. Capacity method: Total pore volume with static CO_2 density and basin-specific static temperature and pressure for the structure at Tern 1.

The second phase of the GEODISC Project (Project 2) further assessed the four most highly-ranked ESCCI sites, which included the Petrel Sub-basin (Lang and Gibson-Poole, 2001; Gibson-Poole et al., 2002). The Petrel Sub-basin ESCCI study characterised the Sandpiper Sandstone and the Plover and Elang formations over the entire sub-basin and progressed to the construction of a geological model. The study completed a sequence stratigraphic analysis of the sub-basin focussing on the two ESCCIs and also characterised the reservoirs for their storage potential and seals for their sealing capacity. The Petrel Sub-basin ESSCIs were modelled as large-scale, open aquifer systems without structural or lateral closure, focussing on the thick, laterally extensive but homogeneous reservoirs and seals. GEODISC identified a total theoretical capacity exceeding 4.9 million tonnes (MT) for both formations (Lang and Gibson-Poole, 2001; Table 3.1). This estimate used a total pore volume derived from a geological model and basin-wide parameters (CO_2 density, temperature, pressure) to calculate the total capacity. The authors then estimated that only 1% of the total storage capacity was available for CO_2 storage. Finally, it was recommended that the geological model undergo refinement, numerical simulations should be performed and that a geomechanical study be undertaken.

Utilising the findings of the previous GEODISC studies, Gibson-Poole (2009) completed a doctoral thesis detailing an assessment of the Petrel Sub-basin ESCCIs and progressed to the completion of numerical simulations of the reservoirs and incorporated the findings of a geomechanical study. Gibson-Poole also completed a detailed sequence stratigraphic analysis defining the systems tracts in key wells across the sub-basin (Table 3.2), and within the sequence stratigraphic framework identified key stratigraphic units in the Mesozoic section of the Petrel Sub-basin. The reservoir units of the ESCCIs, including the Sandpiper Sandstone and the Plover and Elang Formations, all comprise basal thick lowstand systems tracts (LST) succeeded by transgressive-regressive cycle(s) of thin transgressive systems tract (TST)-highstand systems tracts (HST).

In contrast, the Bathurst Island Group and the Frigate Shale, the seals of the ESSCIs, lack the LST and represent transgressive-regressive cycle(s) of thick TST-HST (Gibson-Poole, 2009). In the Bathurst Island Group, the HST is a supersequence produced during a prolonged period of relatively high sea level. The Sandpiper Sandstone and the Plover and Elang formations ESSCI reservoirs were characterised as thick and extensive sand-rich sequences with moderate to very good reservoir quality. The Plover and Elang formations were estimated to have an average porosity of 19% and permeability of 285 millidarcy (mD) and the Sandpiper Sandstone was estimated to have an average porosity of 22% and an average permeability of 1675 mD (Gibson-Poole, 2009). The sealing capacity of the Bathurst Island Group was rated as good to excellent and capable of providing secure containment. As a result, Gibson-Poole (2009) concluded that a lack of structural trapping in the sub-basin promoted hydrodynamic trapping as the likely storage mechanism, with fluid migration towards the southeast. Both the Lang and Gibson-Poole (2001) and Gibson-Poole (2009) studies modelled the reservoirs and seals using a 5 x 5 km cell size. The properties of the cells were populated using the averaged Vshale and porosity values of each layer at the wells and extrapolated throughout the model using a sequential Gaussian simulation method.

The general conclusion of the GEODISC studies of the Petrel Sub-basin was that the Plover and Sandpiper ESSCIs were likely to be good sites for CO_2 geological storage (Lang and Gibson-Poole, 2001; Gibson-Poole et al., 2002). Gibson-Poole (2009) utilised the United States Department of Energy methodology (DOE, 2007) to calculate a total CO_2 storage capacity of 193,464 MT, assuming only 4% of pore space was available.

Based in large part on the work described above, the Carbon Storage Taskforce ranked the sub-basin as a Highly Suitable basin for CO_2 storage (Carbon Storage Taskforce, 2009). This assessment was

part of a nation-wide screening of Australia's sedimentary basins that ranked them based solely on their geological potential for CO_2 storage. The ranking was achieved using a modified Bachu et al. (2007) methodology, only assessing the geology and not taking into account the influences of economic plans, existing infrastructure or proximity to significant emission sources, making it separate from the ranking of the GEODISC Project. The probabilistic theoretical CO_2 geological storage capacity of 55,300 MT (P50, or best estimate; i.e., that 50% of the estimates/outcomes are expected to be larger than this value) reported by the Carbon Storage Taskforce for the Petrel Sub-basin is very large. This calculation was based on the DOE (2007) method (see Table 3.1 for results). As stated in Section 1.4, the present study aims to refine and improve the theoretical storage capacity of the Petrel Sub-basin through a more detailed geological analysis, as well as identify data and knowledge gaps through an evaluation of existing literature and data coverage from publically available datasets.

*Table 3.2 Sequence stratigraphic framework after Colwell and Kennard (1996) and Gibson-Poole (2009) and the formation top interpretation of this study. *Note: Formation biostratigraphy was based on the Bonaparte Basin Biozonation and Stratigraphy Chart 33 (Nicoll et al., 2009).*

Colwell and Kennard (1996) Sequence boundaries	Gibson-Poole (2009) Sequences and system tracts		Biostratigraphy (This study)*	Formation (This study)	Reservoir and seal (This study)
Bathurst Island Sequence	SEQUENCE 8	HST	*Muderongia tetracantha* to *Manumiella druggii*	Wangarlu Formation	Cretaceous seal
	SEQUENCE 7	HST TST	*Systematophora areolata* to *Dinconodinium davidii*	Darwin Formation	Cretaceous seal
				Echuca Shoals Formation	Cretaceous seal
Flamingo Sequence	SEQUENCE 6	HST TST LST	*Pseudoceratium iehiense* to *Egmontodinium torynum*	Sandpiper Sandstone	Cretaceous reservoir
	SEQUENCE 5	HST TST LST			
	SEQUENCE 4	HST TST HST TST	*Wanaea spectabilis,* middle *Murospora florida* to *Dingodinium jurassicum,* middle *Retitriletes watherooensis*	upper Frigate Shale (informal)	Jurassic seal
	SEQUENCE 3	HST TST		lower Frigate Shale (informal)	Jurassic reservoir
Plover Sequence	SEQUENCE 2	HST TST HST TST LST	*Wanaea digitata, Ternia Balmei* to *Rigaudella aemula, Ctenidodinium ancorum*	Elang Formation	Jurassic reservoir
	SEQUENCE 1	HST TST LST	*Corollina torosa* to *Contignisporites cooksoniae*	Plover Formation	Jurassic reservoir

4 Datasets and Methodology

The current assessment focuses on the geological aspects of the sub-basin for CO_2 geological storage and does not include economic suitability, or details any potential impacts or overlaps or coincidences with other natural resources. A regional sub-basin assessment methodology, typical of those commonly used by the petroleum industry for the exploration of oil and gas, was adapted for a CO_2 storage assessment and is summarised in Figure 4.1. Static geological modelling and dynamic reservoir simulations were key steps in this appraisal. The modelling workflow is defined in Figure 4.2.

4.1 Datasets

The study examined a 300 x 300 km area, much larger than the main area of interest of 80 x 100 km, to prevent possible geological model boundary issues for the dynamic modelling stage (Figure 1.4). Within the study area all publically available data were used, including 2D and 3D seismic, wireline logs, core, sidewall core and cuttings samples, as well as borehole data extracted from well completion reports and Geoscience Australia's national data holdings (biostratigraphy, lithological assessments, reservoir porosity, pressure and temperature data, etc.).

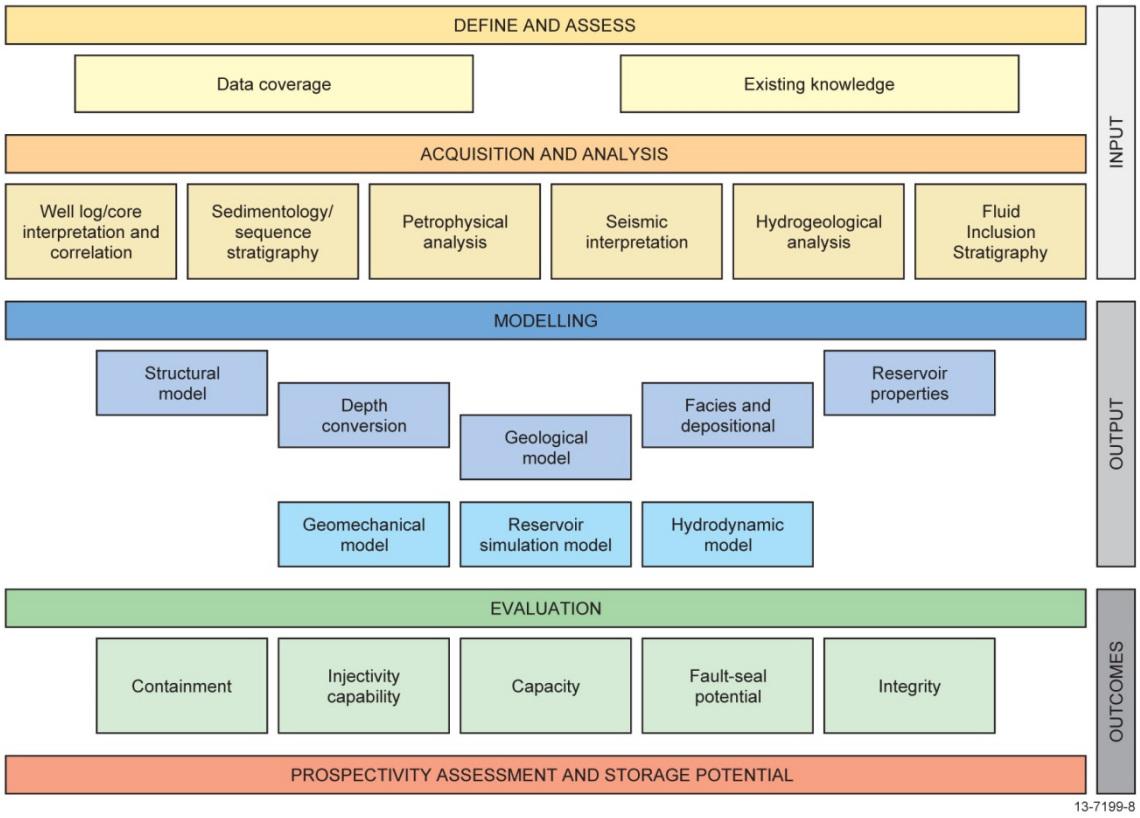

Figure 4.1 The overall workflow undertaken as part of the Petrel Sub-basin CO_2 storage study.

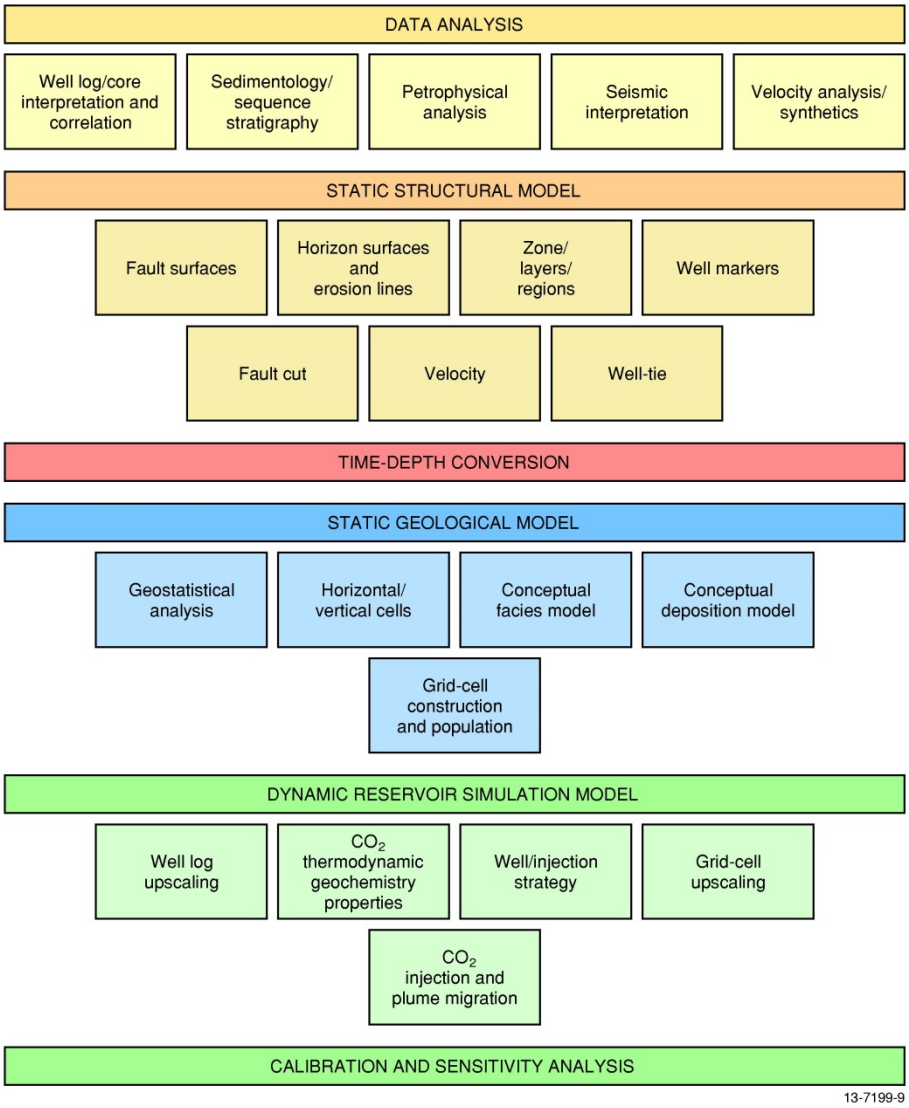

Figure 4.2 The modelling workflow undertaken as part of the Petrel Sub-basin CO_2 storage study.

Seismic data coverage over the sub-basin is highly variable in quality and spacing (Figure 4.4); coverage was moderate over the central and eastern regions of the sub-basin, and very low in the southeast, with only a few lines available (Appendix A). The Petrel Sub-basin also has five 3D seismic surveys located over the Petrel gas field, Shakespeare 1, Blacktip 1 and Barnett 1 wells, and the Thresher 3D seismic volume to the immediate west of the Barnett 1 well. As they are located outside the main area of interest for this study, the Barnett, Blacktip and Thresher 3D seismic data were not used. A total of 34 wells intersected the Mesozoic formations in the offshore Petrel Sub-basin and of these 18 had sufficient datasets that could be utilised for both the petrophysical (Appendix B) and sedimentological (Appendix C) studies (Figure 4.3; Table 4.1; Supplementary Report 1).

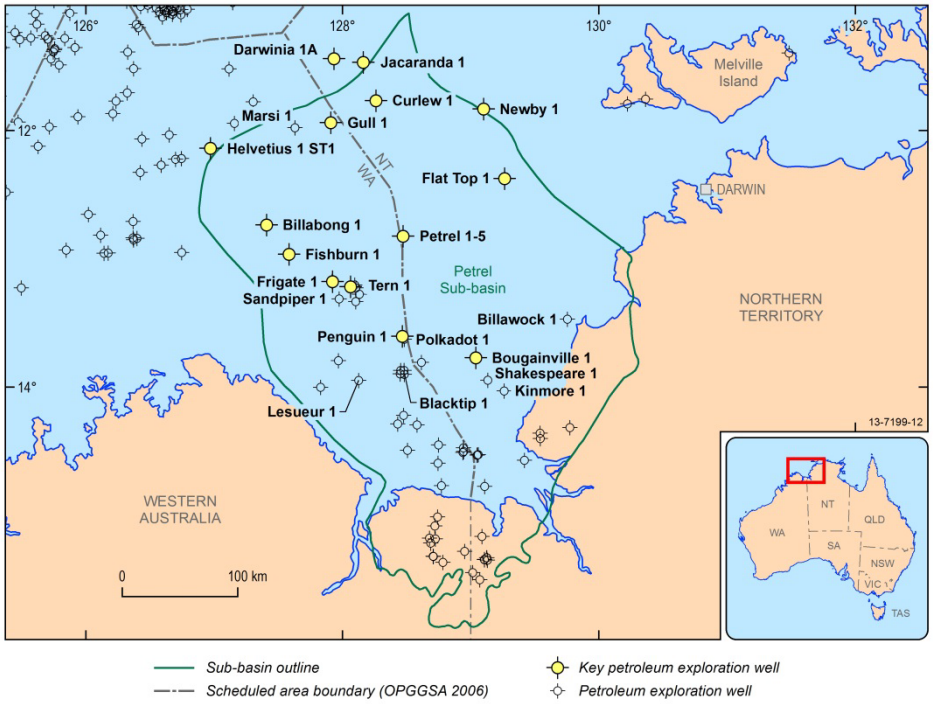

Figure 4.3 Wells of Petrel Sub-basin. Key wells for the petrophysical and sedimentological analyses as part of the Petrel Sub-basin CO2 storage study are highlighted in yellow. See Appendices A, B and C for further information.

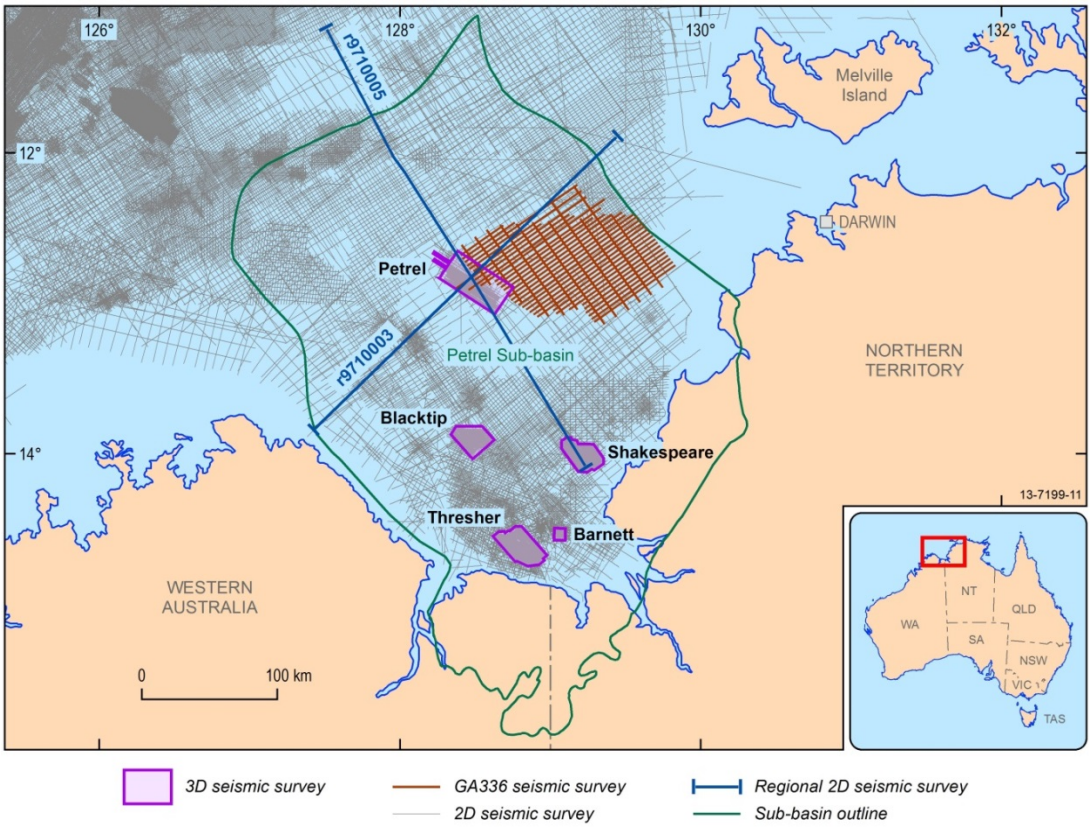

Figure 4.4 The seismic coverage over the Petrel Sub-basin. The seismic survey, GA336, acquired as pre-competitive data in this study is shown in red. Key 3D seismic surveys are labelled. See Appendix A for further information.

Table 4.1 Names, record numbers and data available for key wells used in this study. Formation tops in these wells were used for the seismic interpretation and palaeogeographic analysis. Databases RESFACS and STRATDAT, refer to Geoscience Australia well databases. For further detail regarding petrography (PETROG) mineral mapping (MM), bulk volatile chemistry from fluid inclusions (FIS) and hyperspectral spectroradiometer analysis (HAS), Petrophysics (PETROP) and Sedimentology (SED); Refer to Appendices C, E, D, F, B and C respectively.

WELL NAME	RESFACS	STRATDAT	CORE	PETROG	MM	FIS	HAS	PETROP	SED
Billabong 1	26	32						●	●
Bougainville 1	74	37			●	●		●	●
Curlew 1	74	28						●	●
Fishburn 1	151	88						●	●
Flat Top 1	55	84			●	●		●	●
Frigate 1	77	25						●	●
Gull 1	120	74	●	●	●		●	●	●
Helvetius 1 ST2	5							●	●
Jacaranda 1	88	67	●	●				●	●
Newby 1	9	12				●		●	●
Penguin 1	94	84				●		●	●
Petrel 1	120	46	●	●	●		●	●	●
Petrel 1A	20	50						●	●
Petrel 2	149	53						●	●
Petrel 3	460	7						●	●
Petrel 4	535	16						●	●
Petrel 5	492	3						●	●
Tern 1	131	93	●	●				●	●

4.2 Methodology

Reservoir-seal pairs in the Mesozoic section were identified from previous studies as having the highest potential for CO_2 storage (Bradshaw et al., 2000; Lang and Gibson-Poole, 2001; Gibson-Poole et al., 2002; Carbon Storage Taskforce, 2009; Gibson-Poole, 2009). In the current study, seismic and well data were reinterpreted for this section focussing on characterisation and geographic distribution of the reservoirs and seals. Initially, Mesozoic strata were defined within a sequence stratigraphic framework in order to place the reservoirs and seals in a basin depositional context, thus enabling facies prediction and seismic interpretation between wells.

The sequence stratigraphic framework developed by Colwell and Kennard (1996) and Gibson-Poole (2009), including the supersequences as defined by Colwell and Kennard (1996) (Table 3.2), was used for interpretation purposes. This decision was made on the basis of their key work in describing the target sequences for CO_2 storage. Using a “basement up” sequence stratigraphic approach, these workers interpreted the entire sub-basin rift sequence on the regional 100R seismic survey, as part of a petroleum prospectivity assessment. Each sequence was named according to the major stratigraphic unit it encompassed, which resulted in a similar nomenclature to this study. The Mesozoic strata of the sub-basin was further refined by Gibson-Poole (2009) who identified eight major,

unconformity-bound sequences, as well as system-tracts, based on the integration of seismic data correlated to wells using biostratigraphy, well log analysis, and stratigraphic surfaces (Table 3.2).

Chronostratigraphic and sedimentological assessment of the Petrel Sub-basin Mesozoic stratigraphic units and sequence boundaries was performed using integrated biostratigraphic and depositional environment datasets from Geoscience Australia's Databases (STRATDAT, RESFACS) and correlated with the regional biozonation and stratigraphic chart of the Bonaparte Basin (Nicoll et al., 2009). Further core analysis and petrographic evaluation, wireline log and seismic facies analyses were employed to establish the stratigraphic picks, reservoir and seal lithofacies type and depositional environments. Seismic data were used to correlate between wells and define seismic packages. This formed the basis of a series of palaeogeographic / palaeoenvironmental maps for the Petrel Sub-basin for each of the major time intervals corresponding to the formational boundaries (Appendix C).

Reservoir-seal characterisation – for CO_2 storage – involved applying a series of criteria to the well logs (porosity, permeability, Vshale) together with a sedimentological evaluation. The sedimentological criteria considered a variety of geological constraints, for example, bedding type, thickness, mineralogy, grain size, etc. (Appendix C). The reservoir-seal analysis was further supported by destructive and non-destructive techniques, including:

- Petrography (Appendix C);
- Bulk volatile chemistry from fluid inclusions (FIS; Appendix D);
- Automatic Scanning Electron Microscope (SEM) and Electron Dispersive Spectroscopy (EDS), known as mineral mapping using QEMScan (Appendix E);
- Hyperspectral spectroradiometer analysis (using HyLogger; Appendix F); and
- Rock analysis in the form of porosity, permeability and threshold pressures (Appendix G).

These analyses were completed for four wells: Gull 1, Jacaranda 1, Petrel 1 and Tern 1 (Table 4.1). These wells have cored intervals that preserve the Mesozoic section and available cuttings. The results of the stratigraphic analysis in this study, including the updated stratigraphic picks and biozonation and a breakdown of analyses for each well, are described in Supplementary Report 1, where they are presented in a series of well composites.

The new formation-boundary markers in the wells were then used for seismic interpretation (Table 4.2). To enable well-seismic data integration, well synthetics were generated to match well data in the depth domain accurately against seismic data in the time domain. Check-shot data were used to calibrate an integrated sonic log, before generating a synthetic seismic trace with a zero phase Ricker wavelet. An analytical wavelet was preferred over extracting wavelets from different vintages of seismic data with different phase relationships. The final time-depth relationship was established by matching the synthetic trace to the best seismic data, usually with a small bulk time shift. The formation intervals from the water bottom to the top of the Malita Formation were interpreted in the open-file 2D seismic survey data. The 3D seismic data were only broadly interpreted over the same section.

More than 30,000 line-km of seismic data were interpreted across the sub-basin, identifying nine seismic horizons and 42 major faults (Appendix A). The seismic horizons mapped the distribution of the formations extending from the wells to create a series of seismic packages. The interpreted fault set was restricted to the faults that intersected the Mesozoic–Cenozoic section (Appendix H). Geomechanical analyses were conducted on each major structure to assess their potential for reactivation and leakage (Appendix I). A hydrodynamic study of the sub-basin was also undertaken to evaluate the reservoir pressure and existing fluid flow patterns (Appendix J).

Table 4.2 Key wells of the Petrel Sub-basin with formation tops and seismic picks used in measured depth (m) from rotary table (RT) or Kelly bush (KB) and two-way time (TWT) in this study.

Well	Depth /Time	Wangarlu Formation	Intra-Wangarlu Formation	Darwin Formation	Echuca Shoals Formation	Sandpiper Sandstone	Frigate Formation	Intra-Frigate Formation	Elang Formation	Malita Formation
Billabong 1	mRT	579	748	1380	1400	1490	1600	1790	1835	n/a
	TWT (ms)	540	707	1259	1272	1326	1389	1498	1523	n/a
Bougainville 1	mKB	190	262	280	300	315	365	395	400	465
	TWT (ms)	201	269	289	309	324	370	396	400	456
Curlew 1	mKB	325	771	1686	1705	1730	1910	1950	2001	n/a
	TWT (ms)	325	744	1444	1456	1470	1561	1580	1603	n/a
Fishburn 1	mKB	385	494	1175	1175	1190	1340	1510	1575	1895
	TWT (ms)	363	467	1089	1089	1099	1188	1294	1331	1494
Flat Top 1	mRT	146	272	725	740	784	790	813	826	985
	TWT (ms)	148	283	716	729	758	762	779	787	890
Frigate 1	mKB	309	390	975	1000	1005	1120	1230	1330	1575
	TWT (ms)	330	408	983	1002	1006	1079	1157	1219	1356
Gull 1	mKB	436	1039	2074	2091	2122	2324	2415	2420	2769
	TWT (ms)	448	964	1738	1750	1765	1875	1923	1926	2102
Helvetius 1 ST2	mRT	654	1181	2100	2225	2265	2400	2490	2540	n/a
	TWT (ms)	639	1054	1753	1827	1847	1912	1953	1977	n/a
Jacaranda 1	mRT	800	1500	2850	2870	2880	3250	3530	3620	n/a
	TWT (ms)	670	1200	2077	2088	2093	2259	2384	2423	n/a
Newby 1	mRT	185	328	905	940	960	1050	1075	1100	n/a
	TWT (ms)	194	344	877	908	922	975	988	1001	n/a

Well	Depth /Time	Wangarlu Formation	Intra-Wangarlu Formation	Darwin Formation	Echuca Shoals Formation	Sandpiper Sandstone	Frigate Formation	Intra-Frigate Formation	Elang Formation	Malita Formation
Penguin 1	mKB	298	365	760	780	800	810	865	930	1130
	TWT (ms)	298	348	760	777	792	799	840	885	1019
Petrel 1	mKB	304	546	1300	1315	1330	1575	1830	1900	2230
	TWT (ms)*	306	553	1246	1256	1266	1407	1562	1600	306
Petrel 2	mKB	290	529	1229	1246	1264	1472	1719	1778	2138
	TWT (ms)	309	538	1191	1206	1221	1350	1497	1537	1728
Petrel 3	mKB	321	527	1190	1225	1240	1415	1655	1740	2070
	TWT (ms)	304	530	1157	1187	1197	1305	1449	1496	1674
Petrel 4	mKB	279	516	1207	1225	1244	1471	1706	1770	2136
	TWT (ms)	304	536	1175	1189	1205	1343	1488	1528	1727
Petrel 5	mRT	298	485	1320	1350	1370	1610	1870	1945	2315
	TWT (ms)	335	513	1263	1285	1299	1440	1596	1636	1819
Tern 1	mKB	334	496	1090	1110	1110	1225	1335	1440	1660
	TWT (ms)	357	519	1079	1093	1093	1163	1239	1298	1420

The interpreted seismic horizons and faults were used to build a static geological model (Appendix K) and two dynamic reservoir simulation models (Appendix L). The static model (150 x 250 km) was composed of eight major surfaces and 42 faults and focussed on an area that largely outlines the central to eastern drainage cell of the Petrel Sub-basin (Figure 1.4; Table 4.2). The complete structural static model was then depth converted using regional-based time-depth algorithms. The depth-conversion methodology was based on Goncharov et al. (1999) and Johnston and Goncharov (2012) and adapted to the available data, including incorporating stacking velocities from multi-channel seismic data, ocean bottom seismographs, and well velocities. The velocity modelling was effective at this regional scale, as comparisons of interval velocities calculated independently using two models from refraction and reflection data, respectively, were good for the key geological horizons when matched to well data over a large part of the area (Figure 4.5). However, local discrepancies in depths to these horizons and corresponding well markers calculated using the two alternative velocity models exceeded 10% in some cases. The depth converted structural model could be utilised as a base case for future geological models and represents the major features of the eastern flank of the sub-basin within the bounds of the data resolution (Figure 4.6). This structural model was used for the geomechanical analysis (Appendix I) and hydrodynamic study (Appendix J).

The depth converted static structural model was used to construct a gridded 3D geological model reflecting the local stratigraphy and geological heterogeneity. The geological model contained nine stratigraphic units at a cell resolution of 300 x 300 m horizontally and 1-4 m vertically, comprising approximately 2 billion cells, and populated with porosity estimates derived from the petrophysical analysis (Appendix K).

A fill-spill analysis was completed on the two reservoir surfaces to define probable fluid migration and accumulation pathways using Permedia™ software (Appendix L). A number of CO_2 point sources were located at the down-dip northwest region of the top reservoir surface map. Depth uncertainty was set at ±30 m for which the analysis created randomly 1,000 different realisations of the top reservoir surface map. For each realisation, CO_2 migrated from the point sources according to the surface topography, filled in and spilled from any structural closures reached on its migration path and continued migrating until reaching the edge of the map. The combination of 1,000 realisations gave a frequency distribution of migration pathways. The results of this analysis were used in selecting a representative injection site for dynamic reservoir simulation.

A dynamic reservoir simulation was then undertaken for a small area within the geological grid using the computer software package CMG-GEM™ (Appendix L). The site for the CO_2 injection simulation was located 30 km to the north-northeast of the Petrel gas field (Figure 1.4), and was selected based on the following criteria:

1. The location was representative of the stratigraphy and in a region with high quality reservoirs with good porosity and permeability values;
2. The reservoirs were at a depth to test the effects of injection and plume migration for supercritical CO_2.

Finally, the model was positioned to incorporate two faults that could provide insights as to the pressure effects of CO_2 injection on their behaviour.

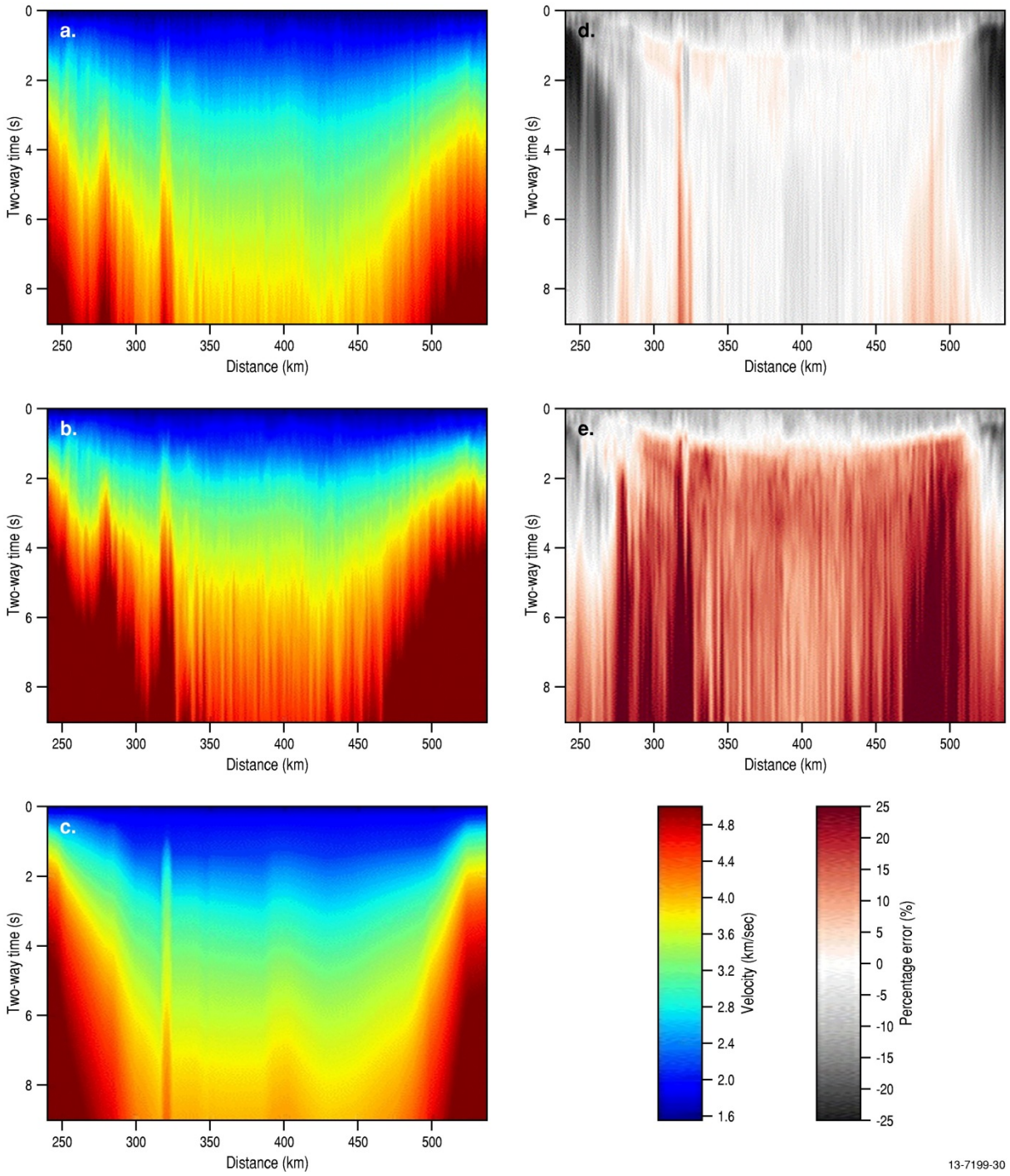

Figure 4.5 Comparison of average seismic velocities derived from final stacking RMS velocities using the inverse Dix equation (a), final stacking RMS velocities (b), and refraction seismic velocities from the OBS data (c) along coincident reflection/refraction line r9710003 (AGSO Regional 2D seismic line 100/03). The percentage in error velocity residuals is shown in d. and e. (d.) represents the percentage of error between (a) and (c), and in (e) between (b) and (c). See Appendix K for further information. See Figure 4.4 for seismic line location.

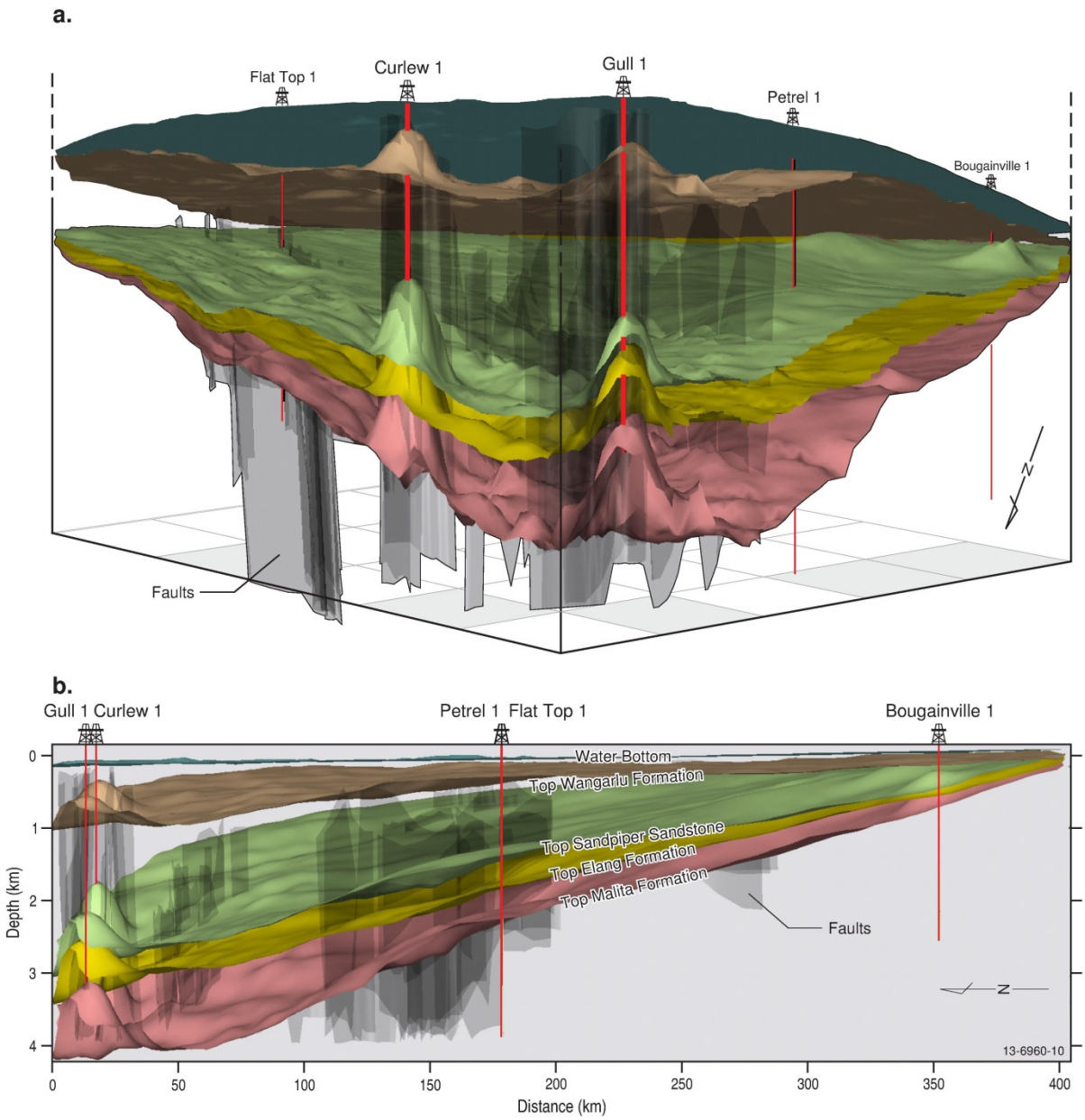

Figure 4.6 The static structural model of this study, showing some of the key surfaces and faults looking towards the southeast (a) and the east (b). See Figure 1.4 for location of the model which is defined by the focus area outline in that figure. See Appendix K for further information.

The simulation was completed using a CO_2 injection rate of 14 million tonnes per annum (MTPA) over 30 years. This was based on the predicted 2020 CO_2 emissions from the Darwin Hub, as defined by the Carbon Storage Taskforce (2009), which is the closest major emission source to the study area. The CO_2 was injected using nine hypothetical vertical wells over a regular grid with 3 km spacing (Figure 4.7). The simulation sets a maximum of 1.556 MTPA of CO_2 per well, and a perforated interval in each well of 300 m. It is important to note that well design optimisation was beyond the scope of this study as well design is site specific and configured to specific reservoir intervals. The number of wells required, their placement and construction, as well as injection parameters are all products of economics, reservoir architecture and even drilling rig availability. Given the regional-scale of this

project, a detailed well design plan would not significantly add to the overall aims of the study. Therefore, the number of wells, well spacing and perforation interval were not optimised in the simulation: the number of wells could be reduced by increasing injection rate per well or by increasing perforation length using deviated wells.

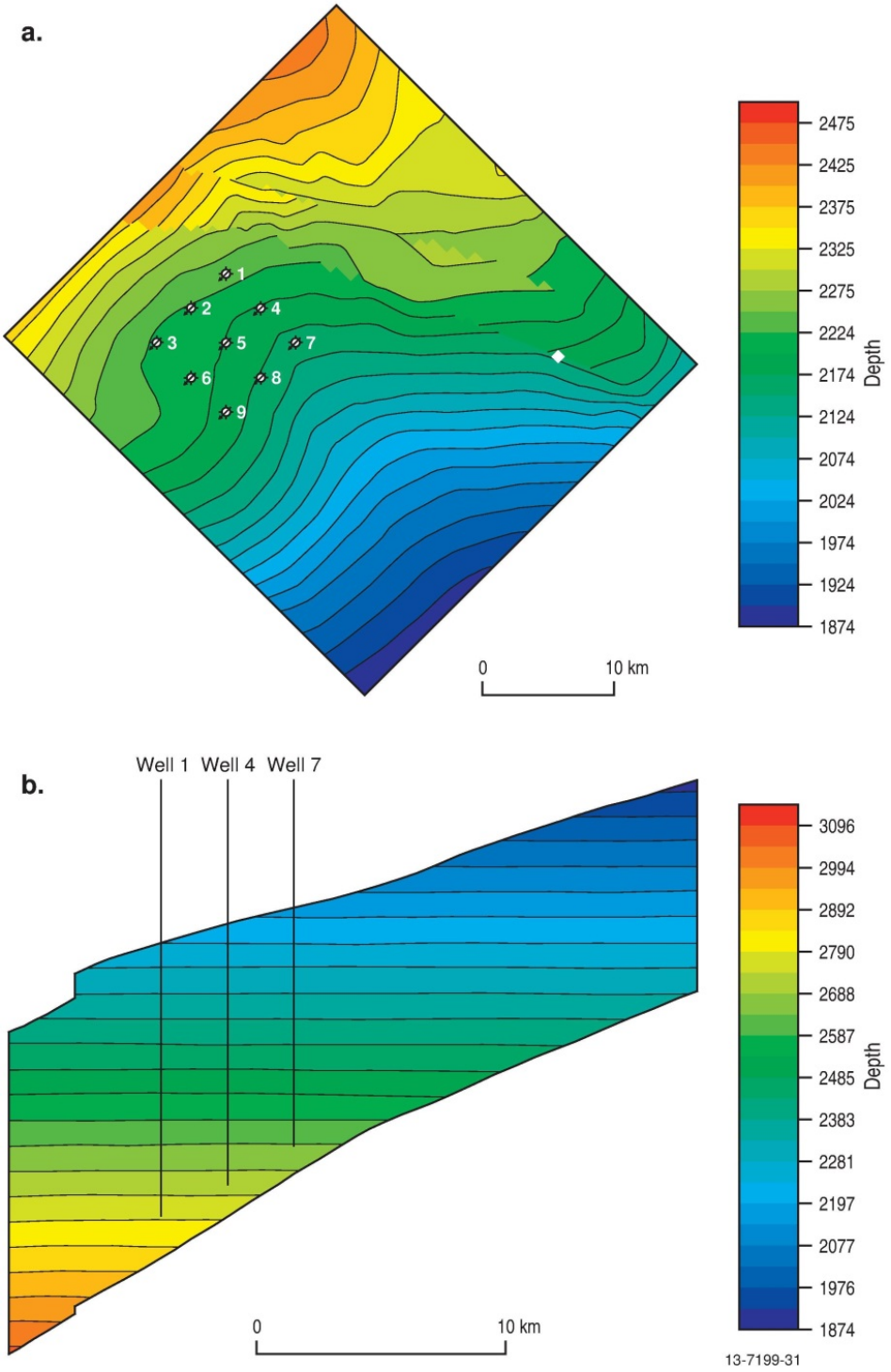

Figure 4.7 Top view (a) and sliced side view (b) of the Jurassic reservoir model with grid top depth. Top of page is north direction. See Figure 1.4 for location. See Appendix L for further information.

5 Pre-competitive Data Acquisition

5.1 Seismic Survey GA336

In May 2012, the Gardline CGG Pte Ltd seismic vessel MV Duke, acquired 4091 km of high-resolution 2D seismic refraction (GA336) and sub-bottom profiler (SBP) data (Figure 5.1). The location was selected to increase 2D seismic data density in the southeastern part of the Petrel Sub-basin, previously only covered by a few lines. The spacing between the 10 km-long lines was 3 km providing ties to existing 2D seismic surveys in the north and south, as well as the Petrel 3D seismic volume, and to the key exploration wells of Petrel 1, Petrel 4 and Flat Top 1. The acquisition and processing, undertaken by Fugro Seismic Imaging Pty, focussed on enhancing the Mesozoic formations. Four key lines, including well-line ties, were depth converted using post-stack depth migration (PSDM) that ensured good ties to well data. In addition, 2D simultaneous inversion analysis was completed on these four lines to assist in reservoir characteristic quantification (porosity, sand percentage, etc.). The results of the PSDM and inversion are detailed in Appendix M.

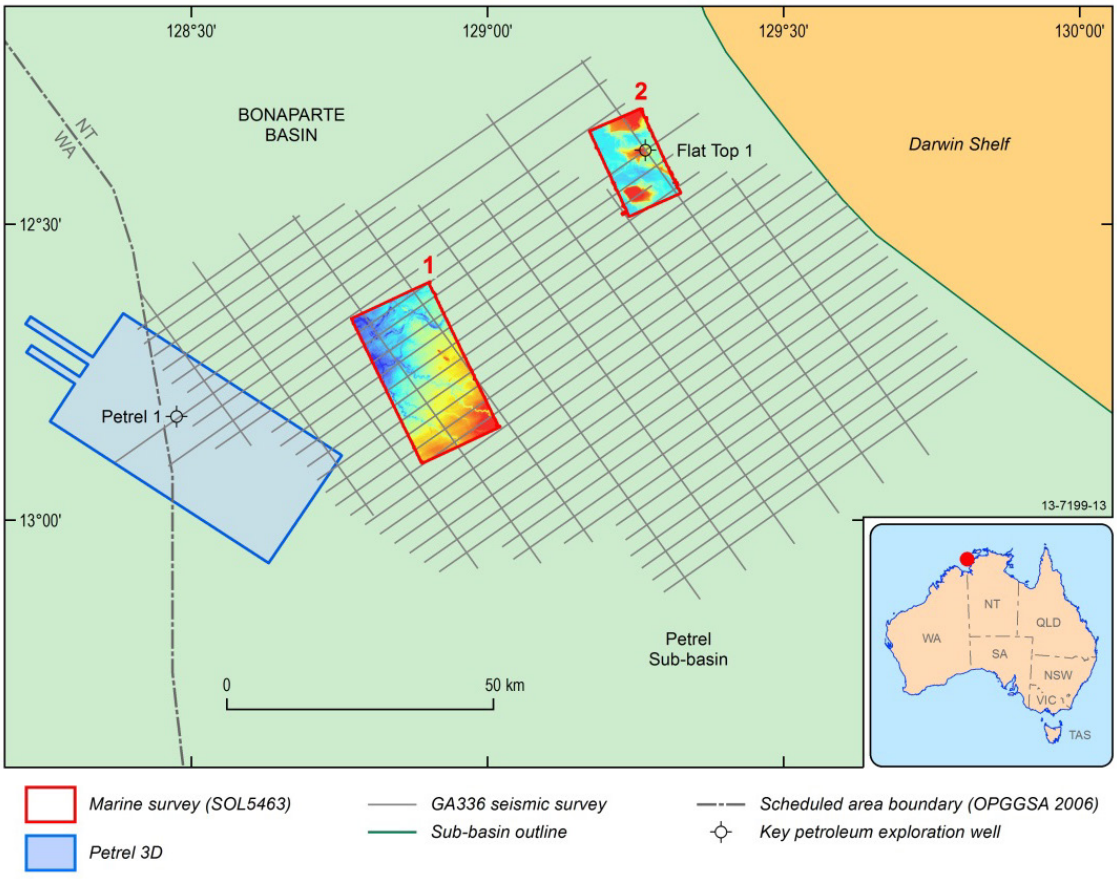

Figure 5.1 Location map for pre-competitive data acquired as part of this study, including GA336 and SOL5436/GA335 surveys. Petrel 3D seismic survey is shown for further spatial reference. See Figure 4.4 for location.

5.2 Marine Study SOL5463/GA335

In May 2012, Geoscience Australia, in collaboration with the Australian Institute of Marine Science (AIMS), carried out a seabed and shallow subsurface mapping and characterisation survey (SOL5463/GA335) of two key areas in the Petrel Sub-basin. This survey was designed to investigate evidence for potential fluid leakage to the seafloor as part of an evaluation of the regional seal quality (Figure 5.1).

The AIMS vessel, the RV *Solander*, collected geophysical, sedimentological and biological data including 652 km^2 of multibeam bathymetry, backscatter and water column data, 655 line-km of multi-channel SBP data, as well as 33 grab samples, 13 towed-video transects, 12 conductivity-temperature-depth profiles and nine vibrocores from the two areas. The survey characterised the shallow subsurface stratigraphy (top 100 m) and provided baseline data for two representative seafloor environments of the Joseph Bonaparte Gulf. See Carroll et al. (2012) for further information on the 2012 Bonaparte Marine Survey.

Survey Area 1 is located on the southeast margin of the central Petrel Sub-basin (Figure 5.1) and lies in water depths of between 78 and 102 m (Figure 5.2). This site was selected to determine the effectiveness of the seals and to identify the presence of any faults in the shallow subsurface through the identification of any seafloor seepage, or subsurface fluid migration.

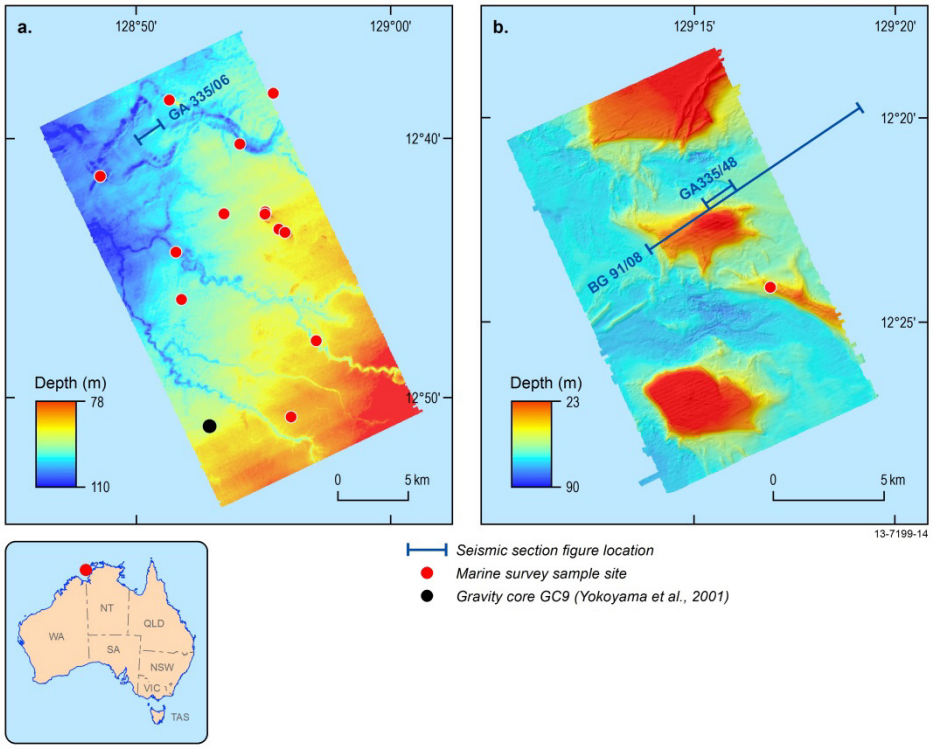

Figure 5.2 Bathymetry images of Area 1 (a) and Area 2 (b) in the Petrel Sub-basin from marine survey SOL5463/GA335 that show the location of sampling stations and the sub-bottom profile and seismic lines GA335/06 (Figure 5.3b), GA335/48 (Figure 5.4b) and BG91/08 (Figure 5.4).

Area 1 occurs over a series of major faults that were identified from pre-existing 2D seismic data. The faults are observed to intersect the formations targeted for CO_2 geological storage, terminating in the

Bathurst Island Group. Discontinuous and / or faded amplitude traces in the 2D seismic data suggest that there might have been fluid migration associated with these faults from depth to the near-surface. However, detailed analysis of the high-resolution bathymetry and SBP data from Area 1 did not identify any seafloor or shallow subsurface geophysical evidence of shallow faults extending to the surface, or evidence of seepage from deeper geological sources (Figure 5.3b).

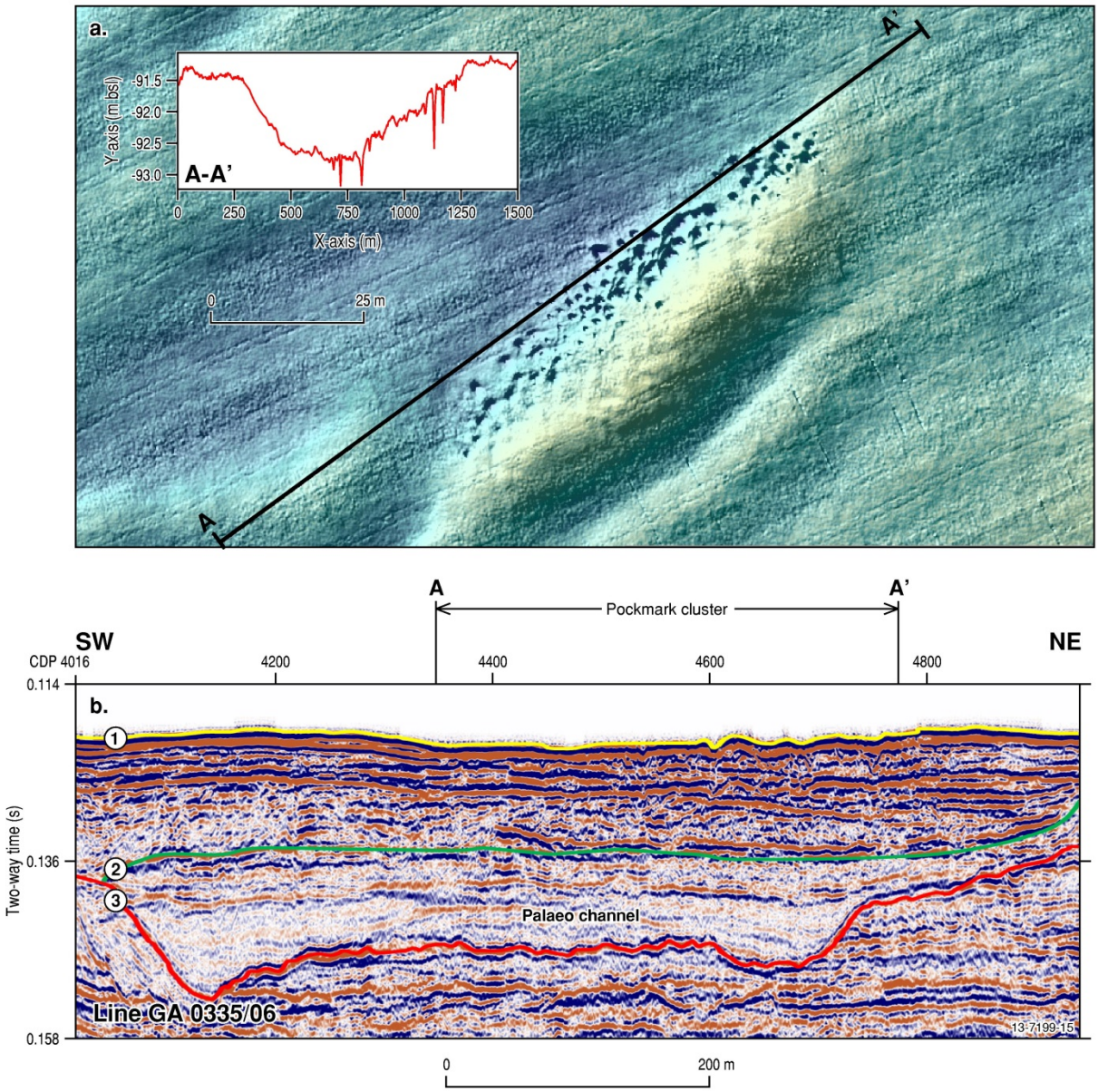

Figure 5.3 Evidence of pockmarks in SOL5463/GA335 survey Area 1. (a) High resolution bathymetry showing a pockmark cluster field in detail over GA335/06. Inset graph show the profile over the pockmark cluster in an overall depression with deeper spikes coinciding with individual pockmarks. (b) Multi-channel SBP line GA335/06 shows the build-up of sediment in the shallow subsurface including a pockmark cluster field, a number of superimposed palaeo-channel cut-and-fill features and unconformities numbered.

Survey Area 2 is located on the eastern margin of the Petrel Sub-basin (Figure 5.1). Here the seafloor environment is dominated by linear carbonate banks and ridges, located in water depths of between 23 and 90 m (Figure 5.2b). This area was selected to investigate whether large sub-basin-bounding

faults identified from the 2D seismic data extended to the seafloor (Figure 5.4c). The high-resolution bathymetry and SBP survey data indicate that faulting occurred during the Neogene to Quaternary. Associated faded and disrupted seismic amplitudes may be evidence of fluid migration in the shallow subsurface of the banks (Figure 5.4a, b). While this could be related to the deeper sub-basin-bounding faults, masking and attenuation of the acoustic sub-bottom signal deep in the section did not allow this to be determined conclusively. Moreover, the carbonate banks and ridges that are present in this area may be related to late-stage faulting, which we infer from their linear morphology. The linear shape of the banks could also be related to the development of reefal environments during periods of lower sea level and to erosion by tidal currents.

Pockmarks on the seafloor are found throughout both Area 1 and Area 2, concentrated in the valleys (up to 2 m depth) and plains (up to 1 m depth) (Figure 5.3a). In Area 2, clusters of pockmarks also occur on the margins of the linear banks and ridges (Figure 5.4a). In both Area 1 and Area 2, the pockmarks commonly occur in spatially distinct clusters and occasionally in relatively linear chains. Discordant and discontinuous reflectors in the SBP data immediately beneath the pockmarks indicate that they occur wholly within the shallow (<7 s two-way-time) sub-surface sediments, and do not have any direct links with deeper basin sources (Figure 5.3b). This suggests that the pockmarks are relatively recent features, most likely formed during and after the latest post-glacial marine transgression.

The two dominant processes forming the pockmarks are inferred to be from the breakdown of Pleistocene- to Holocene-aged organic matter and dewatering in the shallow subsurface sediments. Isotopic geochemical analysis on core and seabed sediment samples recovered from pockmarks in Area 1 support this finding, with all samples having $\delta^{13}C$ and $\delta^{18}O$ values consistent with a seawater carbonate source. No thermogenic isotopic signatures were measured. Analysis of the organic compounds present in the core samples did not indicate any active oil and gas signatures, with compounds related to the bacterial consumption of late Quaternary organic matter, including wood and leaf matter, both of which were contained in the sediment samples.

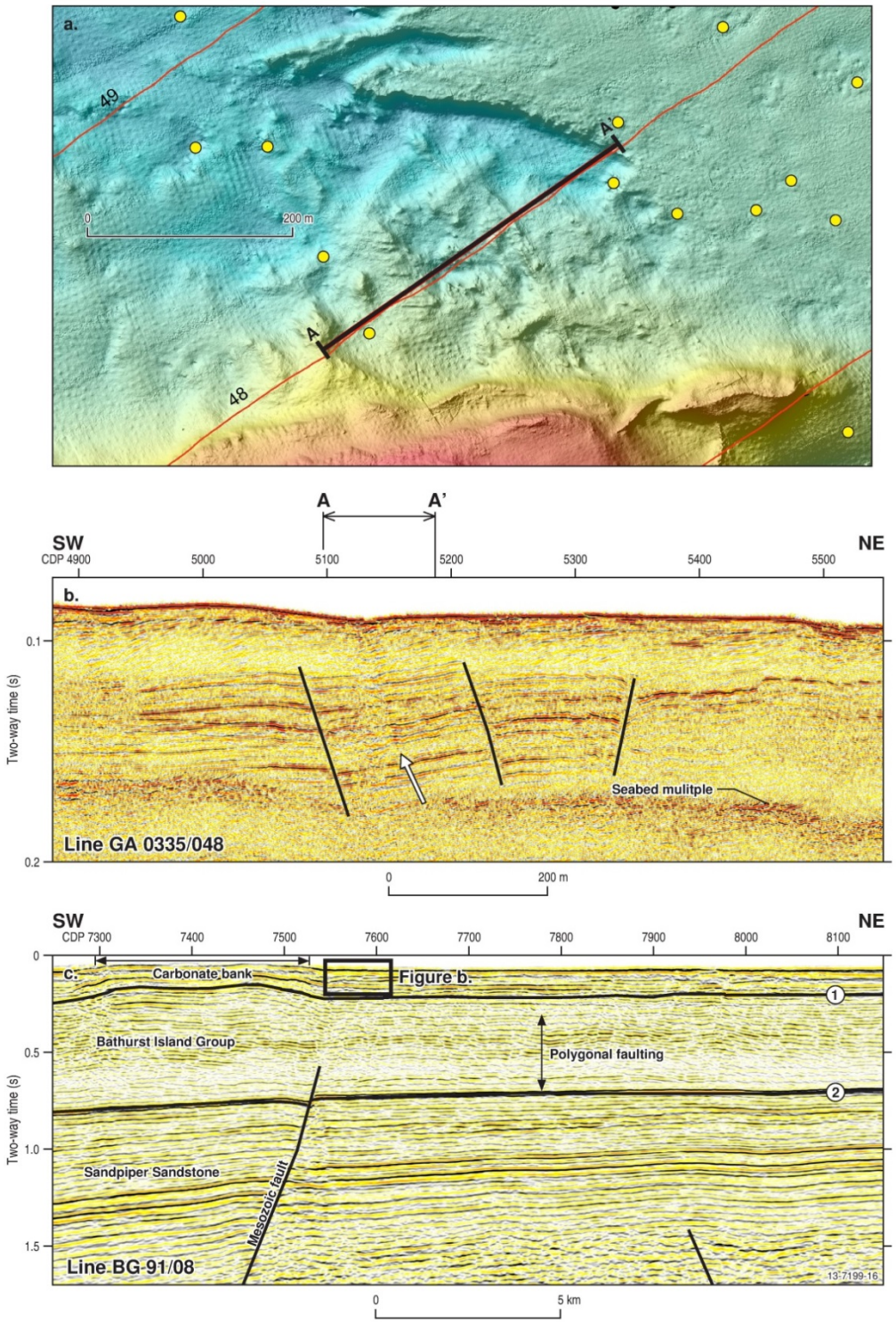

Figure 5.4 Evidence of faults and possible indicators of fluid leakage in SOL5463/GA335 survey Area 2. (a) High resolution bathymetry over GA0335/048, the site of possible fluid leakage indicators and faulting showing a distinct absence of pockmark clusters at this location. Individual pockmarks, in yellow, are unevenly distributed over this section of the seabed. (b) SBP line GA335/048 showing the Quaternary faults (vertical black lines) and a faded amplitude trace suggesting possible leakage features (arrowed). Faults are located next to a large carbonate bank (see Figure 5.2). (c) Shows that Figure (b) sits above deeper sub-basin-bounding faults and polygonal faulting in the Bathurst Island Group interpreted in 2D seismic line BG91/08. Seismic interpretation and well data shows the top of the Bathurst Island Group (Horizon 1) is located approximately 200 m under the present seafloor of Area 2 and that the top of the Sandpiper Sandstone (Horizon 2) is intersected by major Mesozoic faults.

6 Petrel Sub-basin CO_2 Storage

With the exception of the Frigate Shale (see below) the stratigraphic nomenclature follows Colwell and Kennard (1996), Lang and Gibson-Poole (2001) and Nicoll et al. (2009). In this study, the Frigate Shale has been informally designated into the upper and lower Frigate Shale. This is to clearly separate the sandstone-dominated lower Frigate Shale reservoir and the mudstone-dominated upper Frigate Shale seal.

6.1 Reservoir and Seal Characterisation

This study has identified two distinct Mesozoic reservoir-seal pairs suitable for CO_2 storage. The Jurassic reservoir comprises the Plover and Elang formations and the lower Frigate Shale with a Jurassic seal, the upper Frigate Shale. The second reservoir-seal pair comprises the Cretaceous reservoir of the Sandpiper Sandstone with a regional Cretaceous seal in the Bathurst Island Group. The regional seal overlies both upper and lower reservoirs across the entire sub-basin (Figure 1.5). Table 6.1 presents a summary of the sedimentology, lithofacies and depositional environment for these formations. The petrophysical analysis of the reservoirs in key wells is shown in Table 6.2. The distribution of the formations across the study area is shown in the well sections (Figure 6.1) and a composite of Petrel 1 provides a standard well analysis (Figure 6.2). The summary of the sedimentology and stratigraphy presented below is based on the contents of Appendices A, B, C, D, E, F, G and M.

Table 6.1 Sedimentology, facies and depositional environment of the formations for this study. See Appendix C for full details.

Fm.	Lithofacies	Facies description	Depositional Environment
Wangarlu	Massive mudstone	Dark grey to black, very hard massive blocky, mudstone, 90-95% medium/dark grey argillaceous material, minor quartz silt, trace calcareous material, trace white mica, nil visible porosity.	Offshore marine shelf
	Mudstone with shell fragments	Light grey mudstone hard and blocky texture, occasionally calcareous with shell fragments and pyrite blebs.	
	Silty mudstone	Mudstone with small siltstone lenses, medium/ dark grey, very hard massive, blocky, 80-90% medium grey argillaceous, 10-20% silt to very fine quartz grains. Minor calcareous material, trace very fine glauconite pellets with few pyrite aggregates, nil visible porosity.	
	Mudstone interbedded with siltstone	Mudstone interbedded with siltstone and / or very fine-grained sandstone.	

Fm.	Lithofacies	Facies description	Depositional Environment
	Siltstone /fine-grained sandstone interbedded with shale	Argillaceous siltstone interlaminated with mudstone, mottled medium grey/ brown to light greenish-grey, moderately hard to hard, blocky, predominantly silt (trace to 50%), to very fine quartz, 20-50 % very fine to fine glauconite pellets, trace white mica,, trace carbonaceous material, nil to very poor visible porosity.	Offshore marine shelf
	Glauconitic argillaceous siltstone	Mottled medium to dark olive green, moderately hard to hard, blocky, 50-60 % silt to very fine/ fine sandstone, clear translucent, angular to sub-rounded, slightly elongate to slightly spherical, moderately sorted, 25-30% fine to medium glauconite pellets, 20-25% light/medium grey argillaceous material, trace calcareous material, no to very poor visible porosity.	
	Packstone limestone	Brown limestone composed of shell fragment packstone and micritic matrix.	
	Fine- to coarse-grained sandstone	Quartz white to light tan, sub-angular –sub-rounded, fine to coarse-grained sandstone, occasionally silty, fairly sorted, friable with trace of kaolin.	Marine shelf/ offshore bar
Darwin	Glauconitic mudstone	Mudstone slightly silty in part, medium olive grey/ green to medium/ dark olive green, moderately hard to hard, 80-90 % medium to medium dark grey argillaceous material, 10-20% silt to very fine quartz, glauconitic to very glauconitic, trace white mica, trace calcareous material.	Shoreface-offshore
	Glauconitic siltstone interbedded with mudstone	Medium to dark olive green, hard, massive, blocky, predominantly siltstone 20-30%, very fine to fine glauconite pellets, 10-20% medium/dark grey argillaceous material, trace of white mica, nil to very poor visible porosity.	
Echuca Shoals	Mudstone with glauconitic sandstone.	Dark olive green, hard, massive, blocky, 75-85 % dark olive green argillaceous material, 15-25% glauconite pellets, trace fine/ medium to coarse/ very coarse sand grains, trace carbonaceous specks, nil visible porosity.	Shoreface
	Mudstone interbedded with glauconitic siltstone/ sandstone	Glauconitic siltstone thinly interlaminated with mudstone. White to brown, moderately hard to hard, blocky, predominantly silt to very fine sand grains with 20-30 %, light/ medium grey to light brown argillaceous material interbedded with silty mudstone of medium/dark brown, soft to firm, laminated, 80-90 % light brown argillaceous material, 10-20% silt to very fine sand, with glauconite and trace of white mica.	
	Medium-grained glauconitic sandstone with shale	Light grey sandstone, medium to coarse grained with coarse glauconite, occasionally very glauconitic and/or shaly, calcareous with crystalline calcite. Some rounded chert grains. Poor to fair porosity.	
Sandpiper Sandstone	Fine- to coarse-grained sandstone	Fine/ medium to medium/coarse grained sandstone, sub-angular to sub-rounded, slightly elongate to slightly spherical, moderate to well sorted. Medium glauconite pellets good visible porosity.	Lower to middle shoreface
	Massive fine-grained sandstone	Massive sandstone, fine grained, glauconitic with flaser bedding, about 90% sand grains, fine, sub-angular to rounded, well sorted, 0-10% siliceous cement, non-calcareous, good visible porosity.	

Fm.	Lithofacies	Facies description	Depositional Environment
	Fine-grained sandstone interbedded with shale	Glauconitic fine-grained sandstone interbedded with parallel or wavy shale laminations.	
	Mudstone	Medium to light grey- brownish firm mudstone, fissile, with micro micaceous and small amount of slightly calcareous silt.	
Frigate Shale	Bioturbated Fine-grained sandstone	Fine grained sandstone with shale streaks, very glauconitic, bioturbated, medium grey/ brown faintly streaky, up to 80% quartz grains, very fine to fine, angular to sub-rounded, moderately sorted 5-20% siliceous cement silty in part, poor visible porosity.	Middle shoreface -offshore
	Bioturbated siltstone with shell fragments	Siltstone with fine to very fine sandstone, bioturbated, with shell fragments and calcareous nodules. Medium grey/ brown, moderately hard, massive, 20-40% silt to very fine grained sandstone, 60-80% medium grey/ brown argillaceous material, rare to minor calcareous material, trace pyrite aggregates and streaks, no visible porosity.	
	Mudstone	Medium grey/ brown moderately hard massive, bioturbated, 0-10% silt, 90-100% medium grey/brown argillaceous material, trace to common calcareous material, trace pyrite.	
Elang	Medium- to coarse-grained sandstone	Off-white to light grey, brownish grey firm to moderately hard, massive, clear to translucent quartz grains, medium to medium/ coarse sub-angular to sub-rounded, minor angular, slightly elongate to slightly spherical, well sorted, 10-20% quartz cement, common quartz overgrowths, trace medium black lithic fragments, trace pyrite aggregates, non-calcareous, fair to good visible porosity.	Delta plain-shoreface
	Siltstone/ fine-grained sandstone	Siltstone with very fine to fine/medium sandstone, slightly bioturbated, argillaceous in part especially adjacent to coal laminae, moderately sorted with 10-20 % siliceous cement, nil to 20% medium grey argillaceous matrix, trace to 5% coal up to 2 mm laminae thinner laminae discontinuous, black, hard, sub-conchoidal fracture, silty in part, fair visible porosity.	
	Mudstone	Very thin beds of dark grey mudstone.	
Plover	Very fine- to fine-grained sandstone	White very fine to fine grained laminated sandstone, well sorted; with sub-angular to sub-rounded grains with some argillaceous matrix.	
	Fine- to coarse-grained sandstone	Fine to coarse grained sandstone, sub-angular to sub-rounded, poorly to fairly sorted, in places poorly consolidated, with pyrite nodules.	Fluvial
	Massive pebbly Sandstone.	Light to dark brown massive pebbly medium to coarse-grained sandstone, grains sub-rounded to rounded, with some quartz granules, coal streaks and pyrite.	Delta plain-shoreface
	Siltstone interbedded with fine-grained sandstone	Light grey siltstone interbedded with fine sandstone with some fining upward structure.	
	Mudstone	Very thin beds of dark grey mudstone.	

Table 6.2 Summary of the petrophysical analysis results of the reservoirs in key wells. See Appendix B for full details.

Well	Reservoir	Net thickness (m)	Net Sand (fraction)	Sand thickness (m)	Gross (fraction)	Log Porosity (%)	Log Permeability (mD)
Bougainville 1	Cretaceous	66.1	0.94	66.1	0.94	30.4	1181
	Jurassic	65	0.97	65	0.97	29.8	4022
Curlew 1	Cretaceous	145.2	0.77	145.2	0.77	18.5	127
	Jurassic	35.8	0.83	35.1	0.82	11.6	12
Flat Top 1	Cretaceous	34	1	34	1	23.8	345
	Jurassic	178.4	0.91	178.4	0.91	23.9	622
Frigate 1	Cretaceous	108.2	0.81	108.2	0.81	20.6	189
	Jurassic	323.7	0.95	323.7	0.95	18.4	106
Gull 1	Cretaceous	238.3	0.88	237.2	0.88	12.8	44
	Jurassic	572.2	0.85	477.9	0.71	11.3	11
Jacaranda 1	Cretaceous	115.3	0.58	111.6	0.56	8	18
	Jurassic	204.6	0.86	136.3	0.58	8.5	4
Newby 1	Cretaceous	85	0.85	85	0.85	20.5	186
	Jurassic	19.1	0.91	19.1	0.91	20.7	221
Penguin 1	Cretaceous	10.5	0.91	10.5	0.91	21.4	219
	Jurassic	228	0.85	228	0.85	23.7	572
Petrel 1	Cretaceous	168.5	0.97	167.1	0.97	19.7	159
	Jurassic	370.6	0.9	356.4	0.87	16.9	65
Tern 1	Cretaceous	91.7	0.83	91.4	0.82	20.8	197
	Jurassic	322.2	0.97	322.2	0.97	22.1	342

a.

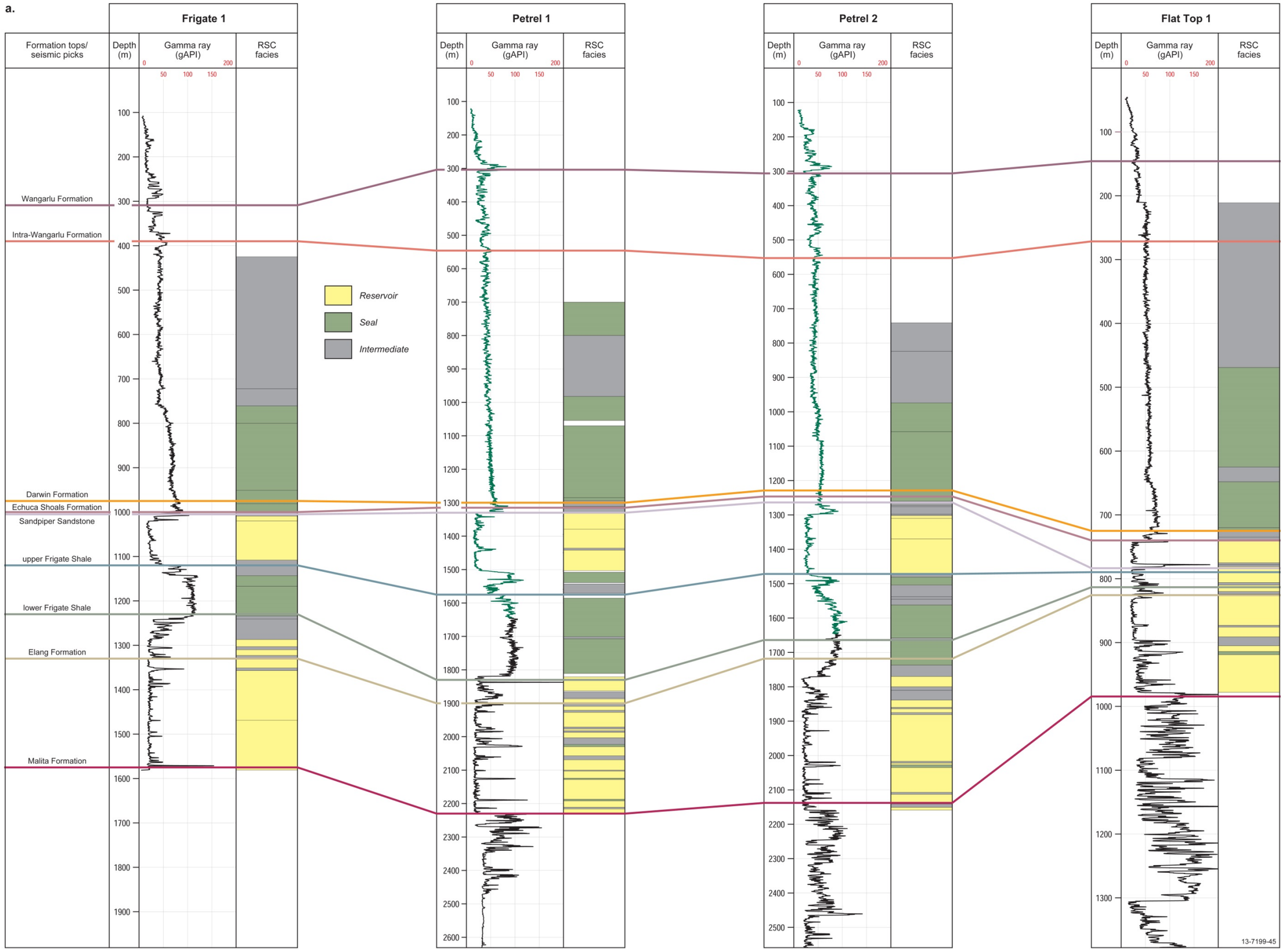
Frigate 1
Petrel 1
Petrel 2
Flat Top 1
Formation tops/ seismic picks
Depth (m)
Gamma ray (gAPI)
RSC facies
Wangarlu Formation
Intra-Wangarlu Formation
Darwin Formation
Echuca Shoals Formation
Sandpiper Sandstone
upper Frigate Shale
lower Frigate Shale
Elang Formation
Malita Formation
Reservoir
Seal
Intermediate
13-7199-45

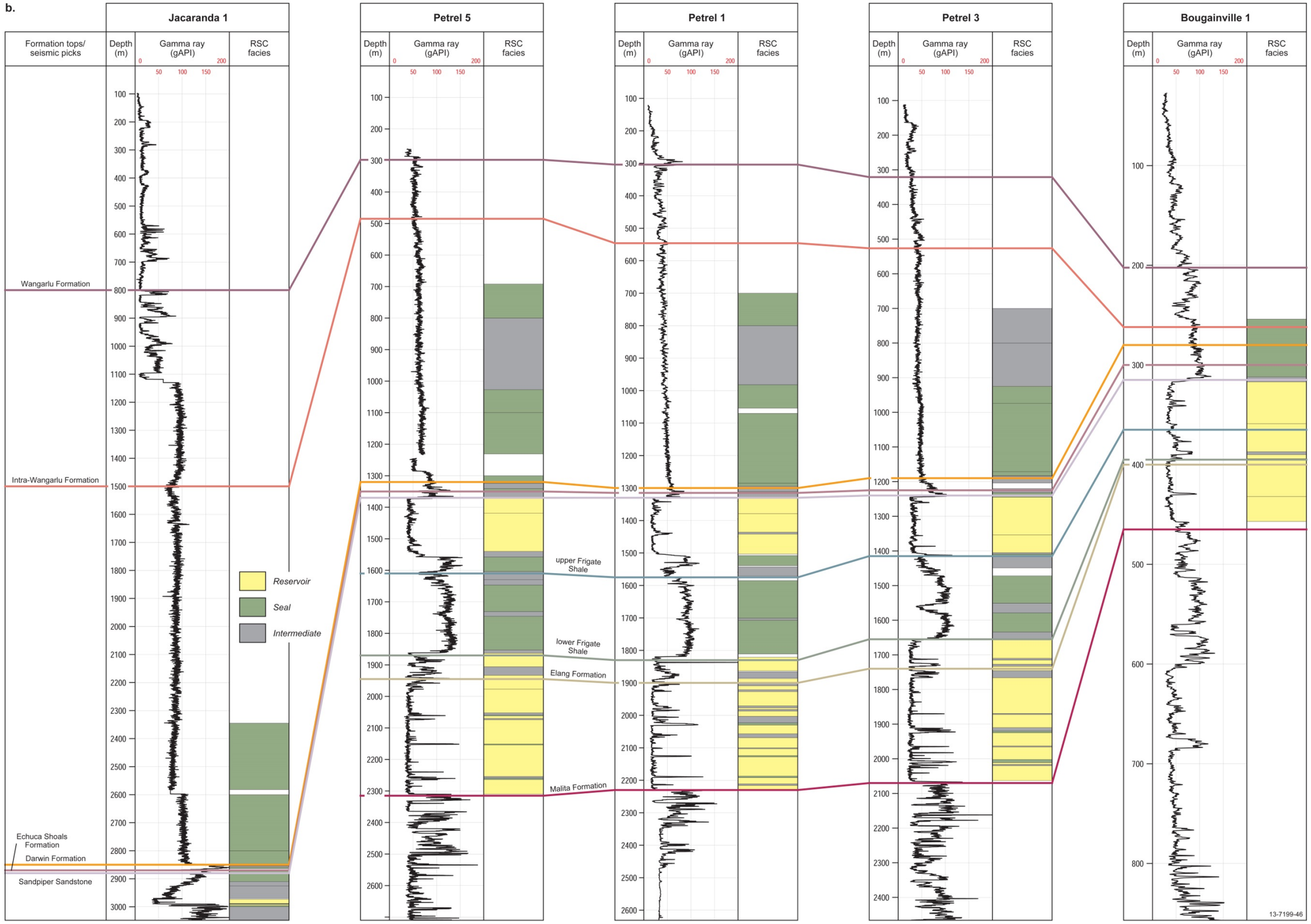

Figure 6.1 Schematic well-section of the study area from (a) the west to east, and (b) south to north. See Figure 2.3 for well locations.

.

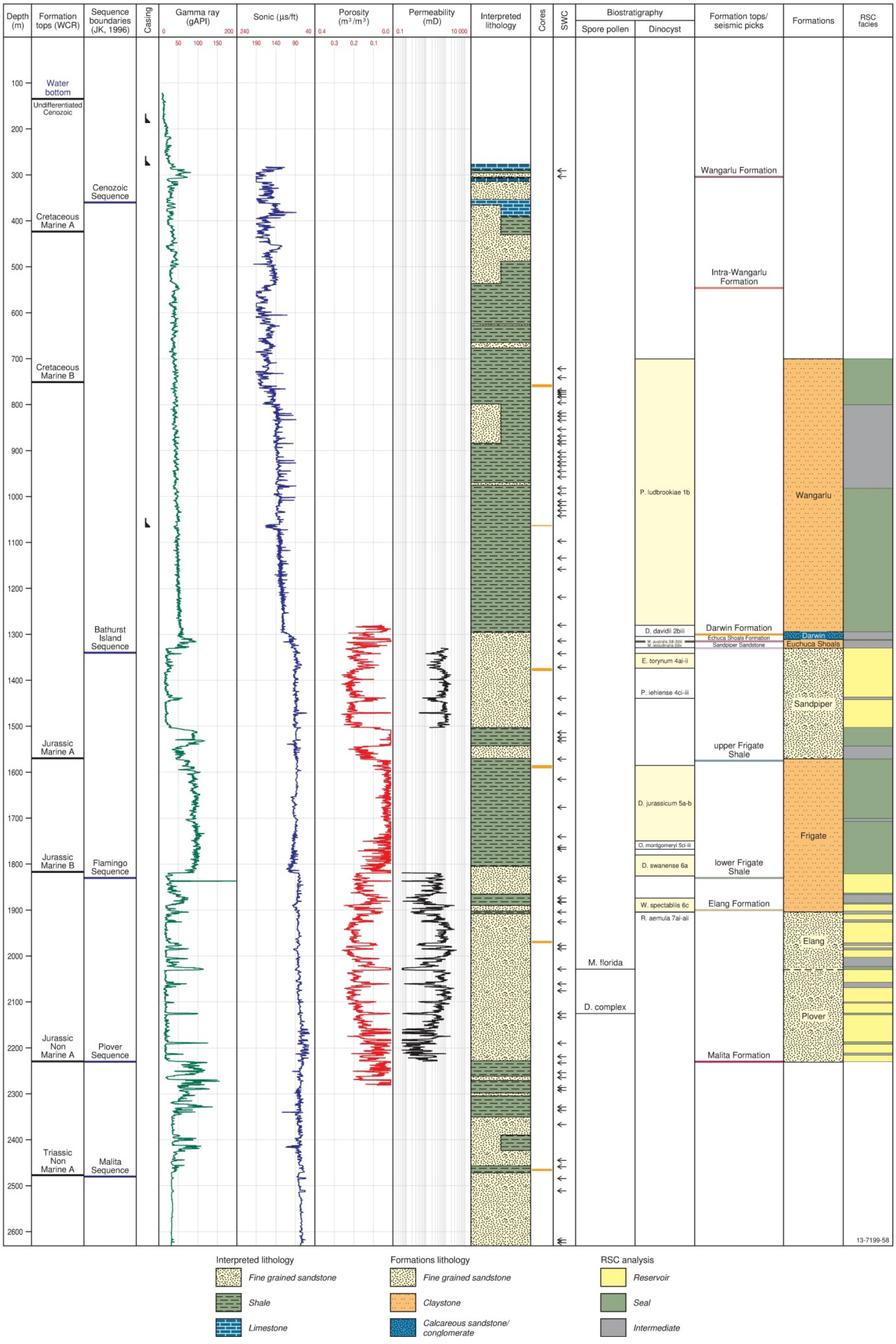

Figure 6.2 Well composite from Petrel 1 from Supplementary Report 1, showing the petrophysical analysis, seismic horizons, formations, and reservoir and seal criteria of this study. Sequence boundaries were taken from Colwell and Kennard (1996), biostratigraphy taken from the Geoscience Australia well database, and WCR formation tops and all other data derived from well completion reports. Note: the formally defined Frigate Shale is informally defined as the upper and lower Frigate Shale in this study. RSC analysis: Reservoir unit is characterised by a low clay content (Vshale range 4-21%), porosity range 12-32% and permeability ranging from <1 to1087 mD. Intermediate unit was characterised by an increase in clay content (Vshale range of 15-56%), low permeability (median range 1-259 mD) and good porosity (median 12-25%). Seal was characterised by very high clay content (Vshale median ranges from 54-84%) with very low permeability (<0.001 mD). For more information about these subdivisions see Appendix C

This page is intentionally blank.

Jurassic Reservoir – Plover, Elang formations and lower Frigate Shale

The Jurassic reservoir is identified as highly prospective with good petrophysical attributes for CO_2 geological storage. The lowermost formation of the Jurassic reservoir is the Plover Formation (Hettangian to Bathonian, *Corollina torosa* to *Contignisporites cooksoniae* zones). It is a predominantly massive, fine- to medium-grained sandstone of fluvial-deltaic origin. The Callovian to Early Oxfordian Elang Formation (spanning the *Wanaea digitata, Ternia Balmei* to *Rigaudella aemula, Ctenidodinium ancorum* dinocyst zones) overlies the Plover Formation and comprises a massive medium- to coarse-grained sandstone deposited in a delta plain-shoreface environment. The uppermost formation of the Jurassic reservoir is a sand-rich unit, here designated as the lower Frigate Shale (Oxfordian-Tithonian; *Wanaea spectabilis,* middle *Murospora florida* to *Dingodinium jurassicum,* middle *Retitriletes watherooensis* zones) and lies disconformably over the Elang Formation. The lower Frigate Shale was deposited in a middle shoreface setting and comprises thinly bedded, bioturbated, very fine-grained sandstone. There was a south and southeast source of sediment supply for the lower formations, however, sediments in the lower Frigate Shale were sourced predominantly from the south and west of the sub-basin. According to petrologic analysis and mineral abundances, the Plover and Elang formations are classified as quartzarenite to sublitharenite, whereas the lower Frigate Shale is determined to be a litharenite to lithic wacke (Figure 6.3; Appendix C). Seismic and stratigraphic interpretation shows that the formations of the Jurassic reservoir are widely distributed across the study area (Figure 6.1 and Figure 6.4). As with most formations in the Petrel Sub-basin, the lower reservoir thickens towards the northwest. The gross thickness of the reservoir averages around 300 m and is thickest at the Petrel gas field, thinning towards the flanks (Figure 6.1, Figure 6.2, and Figure 6.4). Petrophysical well data indicate a high sand content (average 85%; Table 6.2) and evidence from the geological model and seismic facies interpretation indicates that reservoir connectivity is good to excellent. The petrophysical data confirm the depositional environment interpretation for the Jurassic reservoir where the fluvial to deltaic-coastal environments would result in the deposition of successive, amalgamated sand units. The identification of local but laterally continuous layers of siltstone and mudstones, especially in the Plover Formation and lower Frigate Shale, would potentially act as baffles and provide vertical barriers to CO_2 plume migration. These intra-formational seals make the lower reservoir an attractive target as they laterally distribute the CO_2 plume after injection, increasing the solubility of the CO_2 in saline water and residual trapping. The interpretation of thick, laterally continuous sand units and minor mudstones and siltstones in the well log and seismic data is supported by the seismic inversion study (Appendix M). The thick, massive sand units of the Jurassic reservoir were distributed continuously across the sub-basin although minor, locally distributed sealing units are also occasionally present (Figure 6.5).

The Jurassic reservoir has well-log calculated porosities from 20-30% on the shallow margin of the sub-basin to around 17% in the centre. Permeabilities range from 65 to 4022 mD, with higher values found on the basin margin (Table 6.2; Appendix B). The petrophysical results are comparable to the averaged measured core values of the Elang and Plover formations with measurements of 10% in Gull 1 and 21% in Petrel 1 (Table 6.2; Appendix G). These values are consistent with the visual porosity estimates from petrographic analysis (Appendix B). Overall, the porosity and permeability increases up-section throughout the reservoir, with excellent reservoir properties in the Elang Formation and decreasing slightly in the lower Frigate Shale.

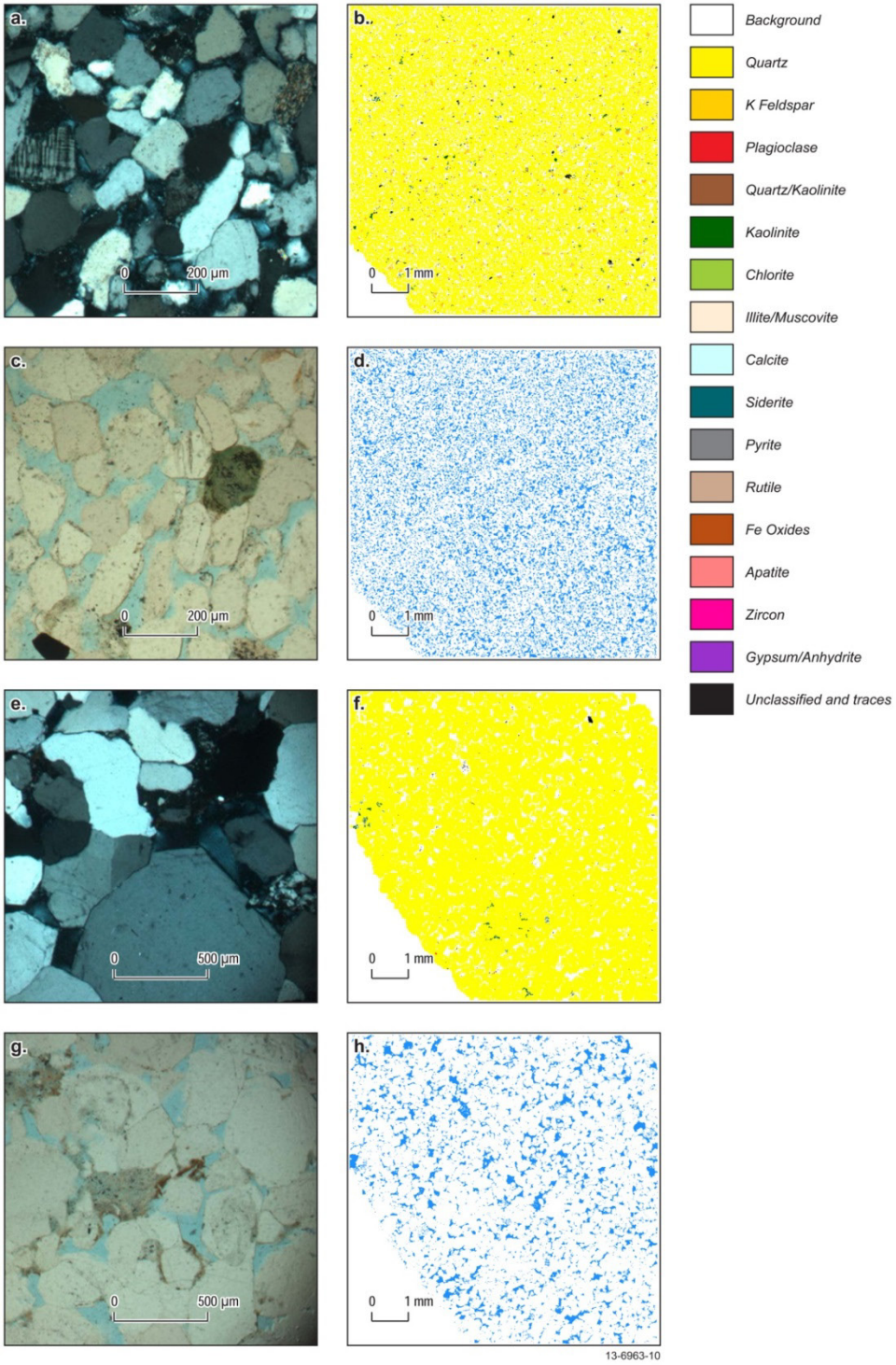

Figure 6.3 Key petrographic sections and mineral maps of the Jurassic reservoir. (a-b) Elang Formation, Petrel 1, 1967.5 m. (a) Thin section photomicrograph illustrating the occurrence of overgrowth silica cement and K-feldspar microcline grain, cross polarised light. (b) Mineral map and legend. (c-d) Elang Formation, Petrel 1, 1967.5 m. (c) Thin section photomicrograph illustrating the visible porosity, pyrite and glauconite grains, polarised light. (d) Porosity maps, defined by regions with no minerals, blue equates to open pores (porosity). (e-f) Plover Formation, Gull 1, 2692.3 m. (e) Thin section photomicrograph illustrating poorly sorted quartz grains with microcrystalline rock fragment of chert, cross polarised light. (f) Mineral map and legend. (g-h) Plover Formation, Gull 1, 2692.3 m. (g) Thin section photomicrograph illustrating the visible porosity, polarised light. (h) Porosity maps, defined by regions with no minerals, blue equates to open pores (porosity). Thin sections taken from Appendix C and mineral maps are taken from Appendix E. Note: Mineral Maps defining quartz/kaolinite and unclassified and traces categories may include some smectitic components that are not resolvable.

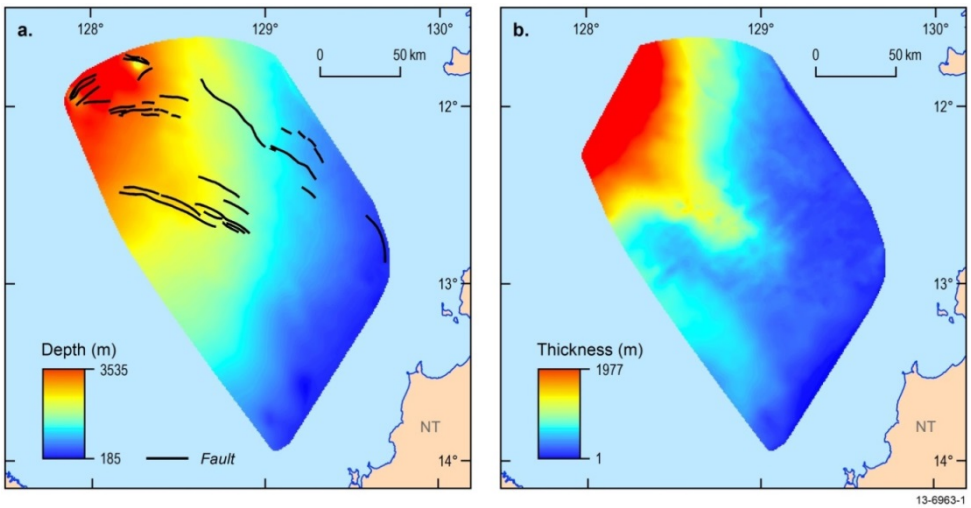

Figure 6.4 Depth (a) and thickness (b) maps of the reservoir Plover and Elang formations. Note: for the purposes of this study the two units were amalgamated.

Jurassic Seal – upper Frigate Shale

The upper Kimmeridgian to Tithonian Frigate Shale forms an effective seal for the underlying Elang Formation reservoir. The upper Frigate Shale was deposited in a range of sedimentary environments from low energy, open marine settings in the central, deeper parts of the sub-basin transitioning to a middle shoreface setting on the shallow flanks towards the south and east (Figure 6.6; Table 6.1). Data from the Petrel gas field wells show the upper Frigate Shale consists of a mudstone facies dominated by micaceous and kaolinitic clays with minor beds of siltstone (Appendices B, F, G) that indicate they were deposited in a marine environment (Figure 6.7). The upper Frigate Shale is inferred to be distributed across the entire study area, with an average thickness of 148 m, from seismic interpretations, as described in Section 4 (Figure 6.1, Figure 6.2, and Figure 6.6). The mudstone facies of the upper Frigate Shale is present in the Petrel wells and its extent can be traced outwards using the existing seismic data. It is inferred, given the marine depositional environment of the facies, that the seismically-defined progrades would be mud-rich and therefore the mudstone facies could be mapped to the top of the progrades (Figure 6.8). The top of the progrades represents the probable maximum extent of the mudstone facies and the toe defines its minimum extent. The results of the seismic inversion analysis verified that the mud-rich interpretation of the progrades is valid (Figure 6.5; Appendix M). The upper Frigate Shale extends north to Curlew 1 and Gull 1, but in these two wells, the mudstone facies transitions to a siltstone-dominated facies. To the east and south of the Petrel gas field, the mudstone facies extends up to 70 km (Figure 1.4).

The potential seal capacity of the upper Frigate Shale measured from the limited core data is shown to be relatively poor (Figure 6.9; Table 6.3). Low threshold pressures were observed based on calculated CO_2 column heights of approximately 65-143 m using mercury injection capillary pressure (MICP) (Appendix G). This measurement corresponds to the only recovered core preserving the upper Frigate Shale in Petrel 1. The sample was collected from the top of the unit, a sandier part of the upper Frigate Shale, near the transition to the overlying reservoir of the Sandpiper Sandstone so the measurements probably indicate a minimum calculated column height. In contrast, petrology and sedimentological facies analysis of cuttings and side wall core found that in the lower section of the upper Frigate Shale the mudstone was clay-rich and fissile (Appendix C). Furthermore, the thickness and lateral extent indicates that the mudstone-facies would act as an effective caprock to the reservoir

below. According to Kaldi et al. (2013) understanding the lithology, thickness and lateral extent of the seal can be used to support the effectiveness of the unit to act as a seal in the absence of a comprehensive suite of CO_2 column height measurements. Therefore, based on the mapping of the seal extent and the petrology, and contrary to the calculated column height measurements, it is concluded that the upper Frigate Shale is most likely an effective seal. Finally, additional evidence of the FIS analysis of the Frigate Shale in the Newby 1 and Penguin 1 wells demonstrates that fluid migration has not occurred, and from this and an adequate sealing capacity can be inferred for this upper unit.

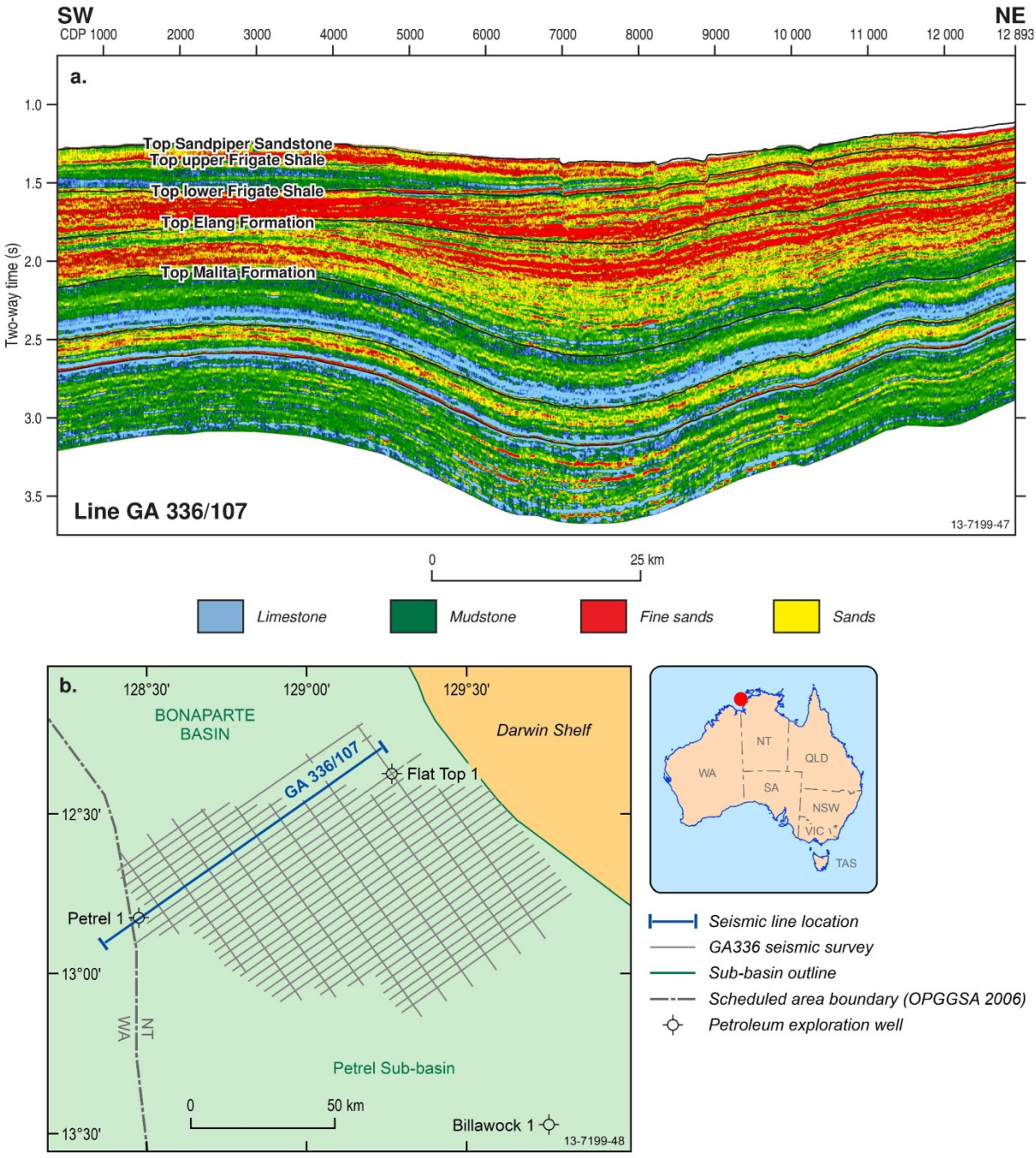

Figure 6.5 Seismic inversion analysis of GA336-107 showing sand distribution across the study area. Also note the presence of the upper Frigate Shale mudstone terminating towards the flanks. See Appendix M for full details.

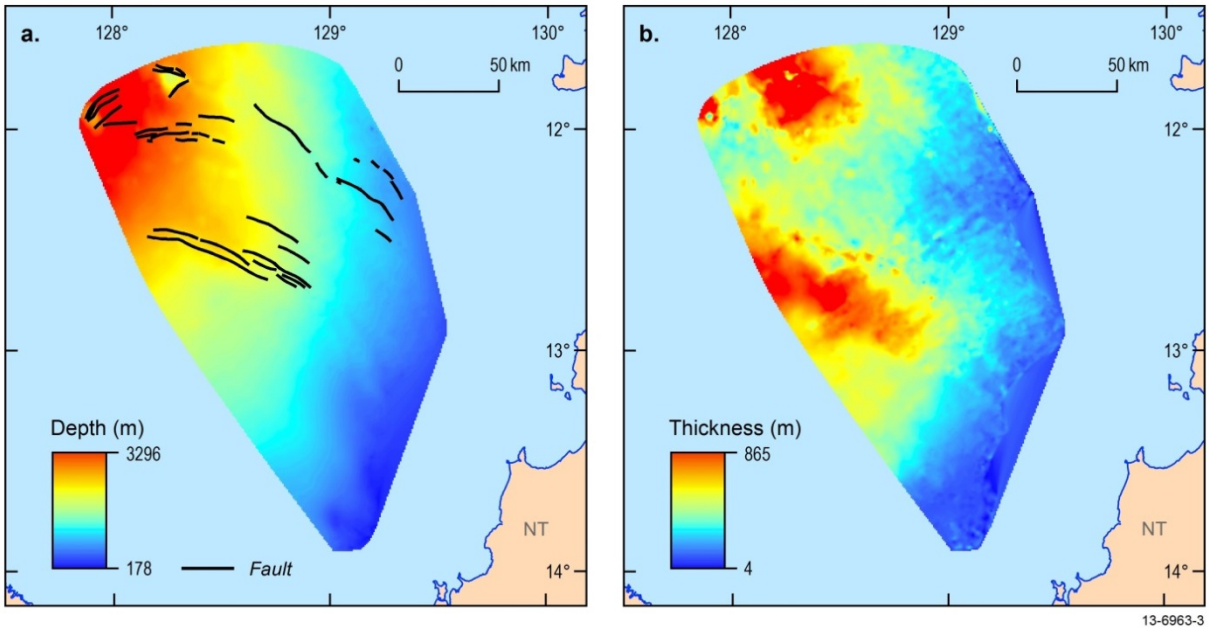

Figure 6.6 Depth (a) and thickness (b) maps of the Frigate Shale. Note: the total extent of the upper and lower Frigate Shale was combined in this figure.

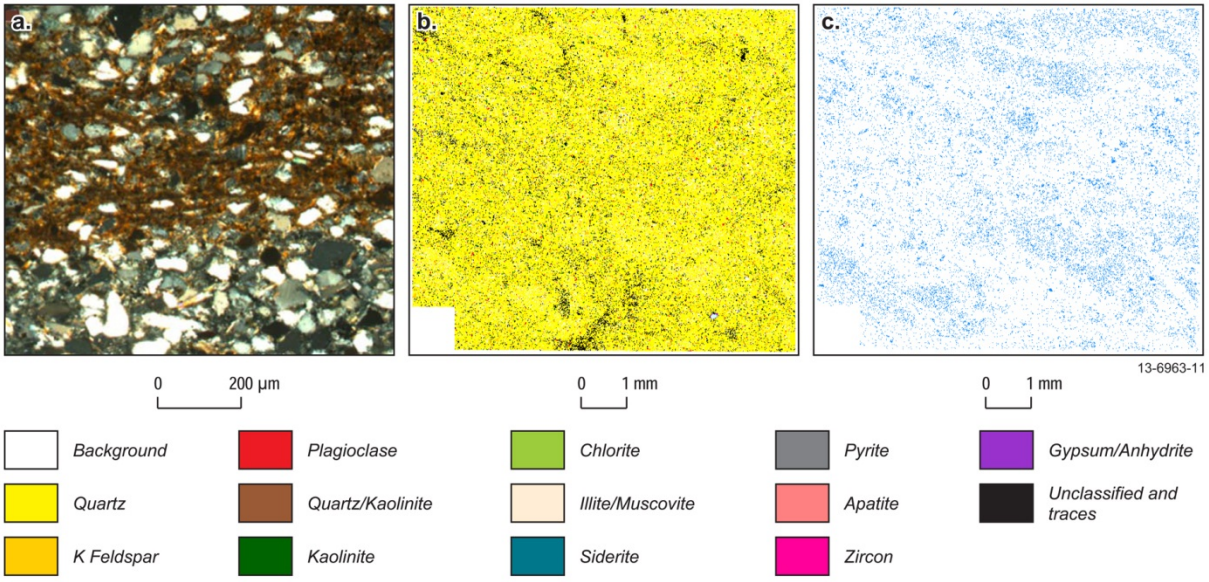

Figure 6.7 Photomicrograph and mineral and porosity maps for selected core sample of the upper Frigate Shale. (a-c) Upper Frigate Shale, Petrel 1, 1587.2 m. (a) Thin section photomicrograph illustrating the occurrence of very fine to fine quartz grains with mica flakes. It also shows silt and clay rich zones, cross polarised light. (b) Mineral map. (c) Porosity maps, defined by regions with no minerals, blue equates to open pores (porosity). Mineral legend applies to (b). Thin sections taken from Appendix C and mineral maps are taken from Appendix E. Note: Mineral Maps defining quartz/kaolinite and unclassified and traces categories may include some smectitic components that are not resolvable.

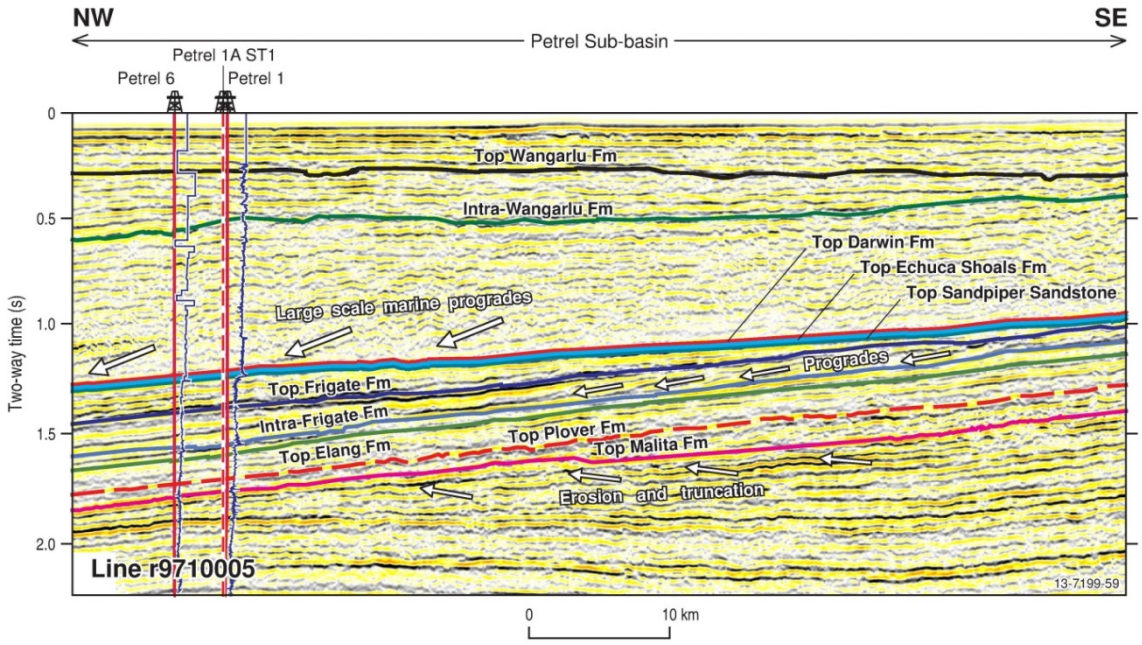

Figure 6.8 Seismic facies analysis of seismic line r9710005 (AGSO Regional 2D seismic line 100-05) showing seismic character of the formations. Also note the presence of the prograde in the upper Frigate Shale mudstone terminating towards the flanks (right). See Figure 4.4 for seismic line location. See Appendix A for full details.

Table 6.3 Summary of the core analysis results of the seals in key wells. Results from this study are combined with results of Lang and Gibson-Poole (2001) and Gibson-Poole (2009). See Appendix G for full details.

Well	Formation	Brine-CO_2 Injection Threshold Pressure (psi)	MICP Threshold Pressure (psi)	MICP CO_2 Column Height (m)		
				This Study	Gibson Poole (2009)	Lang and Gibson Poole (2001)
Gull 1	upper Wangarlu		286	340	310	500
					309	500
	mid Wangarlu		115	137	799	800
Jacaranda 1	base Darwin-top Echuca Shoals	26.1	141	168		
Petrel 1	upper Wangarlu		155	184	176	240
					249	200
	mid Wangarlu	15.1	307	365	251	305
					175	305
					250	400
	upper Frigate Shale	9.4	55	65	34	52
Tern 1	mid-lower Wangarlu		135	161		

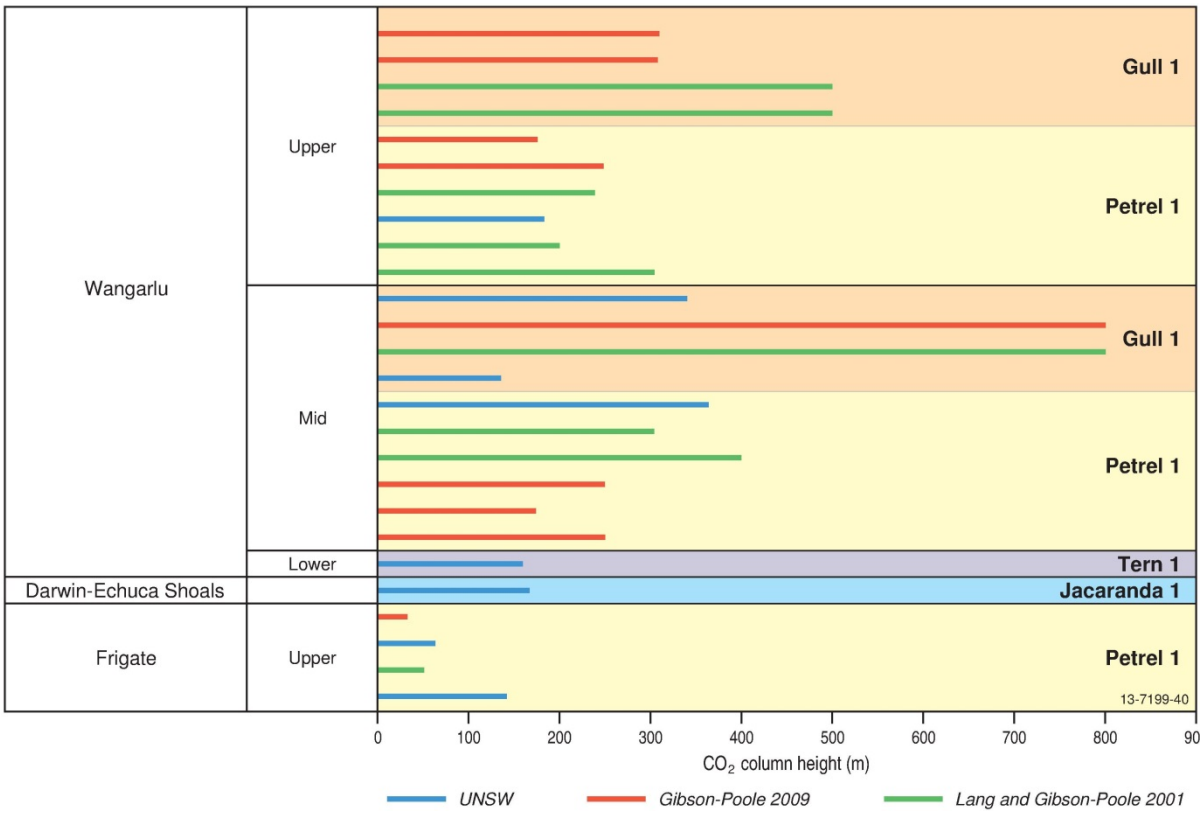

Figure 6.9 Seal capacity column heights. Results from this study are combined with results of Gibson-Poole (2009) and Lang and Gibson-Poole (2001). See Appendix G for full details.

Cretaceous Reservoir – Sandpiper Sandstone

The Cretaceous reservoir comprises the Late Tithonian-Early Valanginian Sandpiper Sandstone (*Pseudoceratium iehiense* to *Egmontodinium torynum* palynological zones). It is identified as highly prospective with good to excellent properties for CO_2 geological storage. Petrophysical and mineralogical analysis show that the reservoir consists of massive, fine- to coarse-grained, glauconitic and pyritic sandstones with minor to rare siltstone and mudstone interbeds (Appendices C, E and F). Petrological analysis and mineral abundances were used to classify the Sandpiper Sandstone as quartzarenite to sublitharenite (Figure 6.10). According to the interpreted seismic data and geological modelling, the formation is present across much of the Petrel Sub-basin (Figure 6.11). The sandstone is thickest along the basin axis (e.g. Petrel 1, 255 m) (Figure 6.2), averaging 164 m in thickness. Towards the southeast, as well as over the salt diapirs, the unit thins with an average thickness of around 50 m (Figure 6.1 and Figure 6.11). The sandstone represents a transition from a lower shoreface to a shallower middle shoreface setting with progradational deposits sourced from the northeast and south.

Well logs show that the Sandpiper Sandstone has porosities of 20-30% on the shallow margin of the sub-basin and around 20% in the centre with permeabilities ranging from 44 to 1181 mD (Table 6.2; Appendix B). Core measurements are slightly lower than the petrophysical data with measurements from Petrel 1 indicating a permeability of 65 mD and porosity of 14.7%, which are comparable to those recorded at Gull 1 with measurements of 58 mD and 11.7%, respectively (Appendix G).

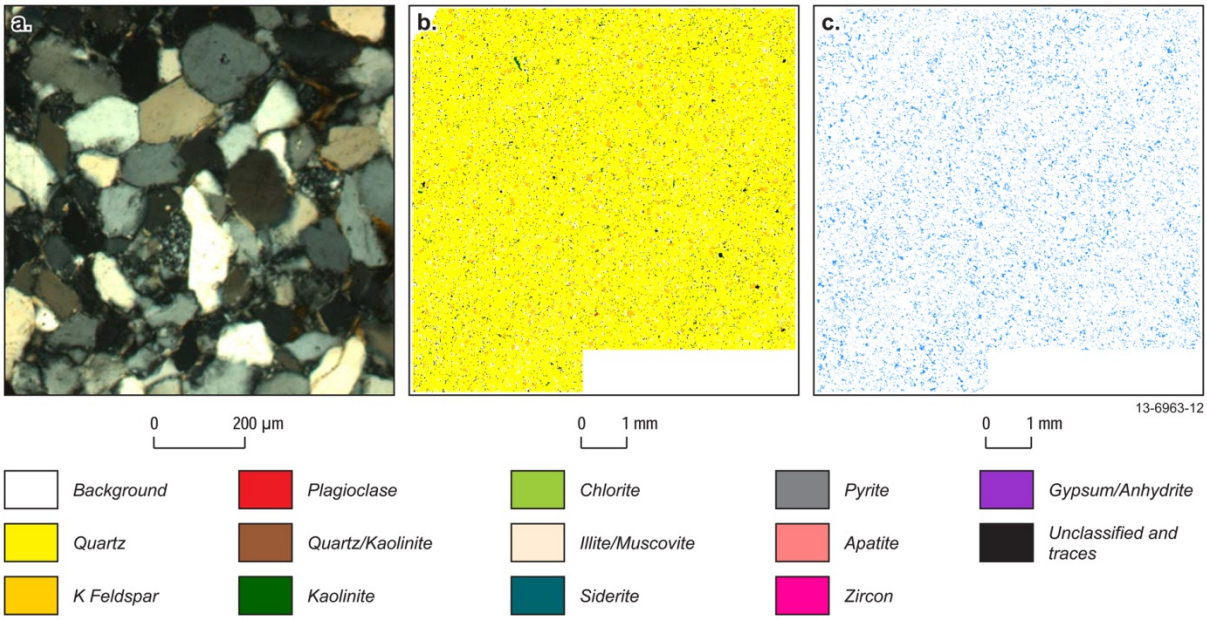

Figure 6.10 Photomicrograph and mineral and porosity maps for selected core sample of the Sandpiper Sandstone. (a-c) Sandpiper Sandstone, Petrel 1, 1375.6 m. (a) Thin section photomicrograph illustrating the occurrence of quartz grains surrounded with clay films. It also shows microcrystalline rock fragment of quartzite, cross polarised light. (b) Mineral map. (c) Porosity maps, defined by regions with no minerals, blue equates to open pores (porosity). Mineral legend applies to (b). Thin sections taken from Appendix C and mineral maps are taken from Appendix E. Note: Mineral Maps defining quartz/kaolinite and unclassified and traces categories may include some smectitic components that are not resolvable.

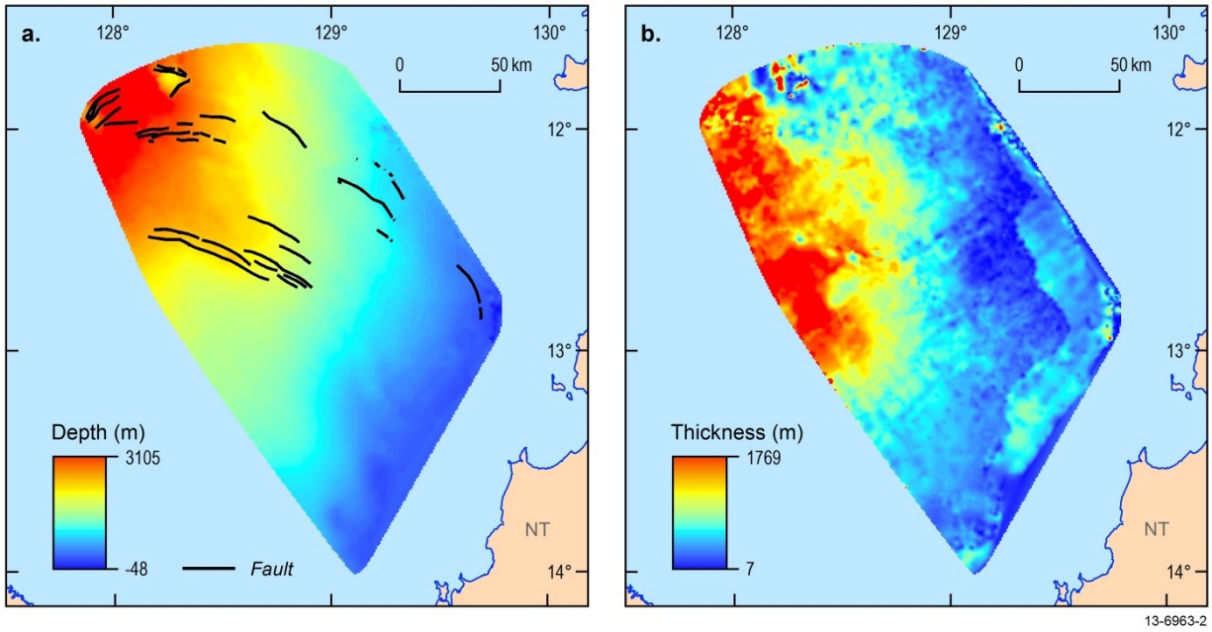

Figure 6.11 Depth (a) and thickness (b) maps of the Sandpiper Sandstone.

Regional Cretaceous Seal – Bathurst Island Group

The Bathurst Island Group (Valanginian to Maastrichtian) represents the effective seal of the Sandpiper Sandstone and flanks of the Elang and Plover formations and lower Frigate Shale. It is defined in this study as a plausible regional, conventional seal with effective sealing capacity. The sedimentology varies from condensed, thin, basal transgressive glauconitic mudstones and siltstones (Echuca Shoals Formation) to glauconitic, calcareous mudstones and sandstones with a basal conglomerate (Darwin Formation). Palynological data from these formations span the *Systematophora areolata* to *Dinconodinium davidii* dinocyst zones and both were deposited on a shallow marine shelf. These formations were succeeded by the Wangarlu Formation (*Muderongia tetracantha* to *Manumiella druggii* zones), which is a very thick micaceous mudstone, with minor marl, siltstone, fine sandstone and limestone units deposited in an open marine setting (Table 6.1). According to mineralogical abundances and petrology, the Wangarlu Formation is typically a mudstone (Figure 6.12). Hyperspectral spectroradiometer analysis indicates that the mudstones are dominated by smectitic clays (Appendix F). Seismic interpretation, as described in Section 4, indicates that the Bathurst Island Group is distributed ubiquitously across the Petrel Sub-basin with thicknesses ranging from 100 m on the flanks (e.g. Bougainville 1) to over 1000 m in the centre and northern flanks (Figure 6.13).

Threshold pressure measurements obtained from limited core data in the Echuca Shoals, Darwin and Wangarlu formations vary widely, depending on the techniques used; the threshold pressure from saline water-CO_2 injection giving lower values than MICP (Figure 6.9 and Table 6.3). However, the mudstones in the Bathurst Island Group were calculated to retain a CO_2 column height of around 137-365 m, averaging 225.8 m (Appendix G). Due to a lack of structural closure over the majority of the Petrel Sub-basin, it is unlikely that a CO_2 column height greater than the estimated threshold pressures measured would be reached in the reservoirs below. Finally, FIS analysis of Bougainville 1, Flat Top 1, Newby 1, and Penguin 1 show that the Wangarlu Formation is an effective seal (Appendix D).

6.2 Geomechanics and Fault Characterisation

A comprehensive assessment of the CO_2 geological storage potential requires an assessment of the fault-seal potential of the Petrel Sub-basin. A comprehensive report containing the methodology and a description of the faults in the Petrel Sub-basin are detailed in Appendix H. This was achieved through a geomechanical study and characterisation of polygonal faulting, which is a widespread feature of the Petrel Sub-basin. The findings of this report are supported by the results of the fault geomechanics (Appendix I) and polygonal fault (Appendix N) studies. The geomechanical analysis did not include the polygonal faulting due to their spatial complexity. These studies are summarised below.

The Neotectonic record of the Petrel Sub-basin has not been studied specifically and seismicity risk or hazard maps have not been extended to offshore northern Australia. Historical earthquake data indicate that the southern Timor Sea and Joseph Bonaparte Gulf have recorded only rare instances of seismicity (magnitudes <3), but there are Neogene faults present in the sub-basin indicating recent tectonic movement (Clark et al., 2011; Burbidge, 2012). Moreover, Quaternary fault movement was identified by the offset of strata in the shallow subsurface sediments imaged in the SBP data (Figure 5.4a). These Quaternary faults have not been linked to any known tectonism. Overall, the impact of neotectonism on the prospectivity of the basin for CO_2 storage is unknown, but seismic activity is very rare in this region and therefore the impact is assumed to be low. Recent tectonism aside, the Petrel Sub-basin does have a long history of tectonism with major structural features throughout the sub-basin.

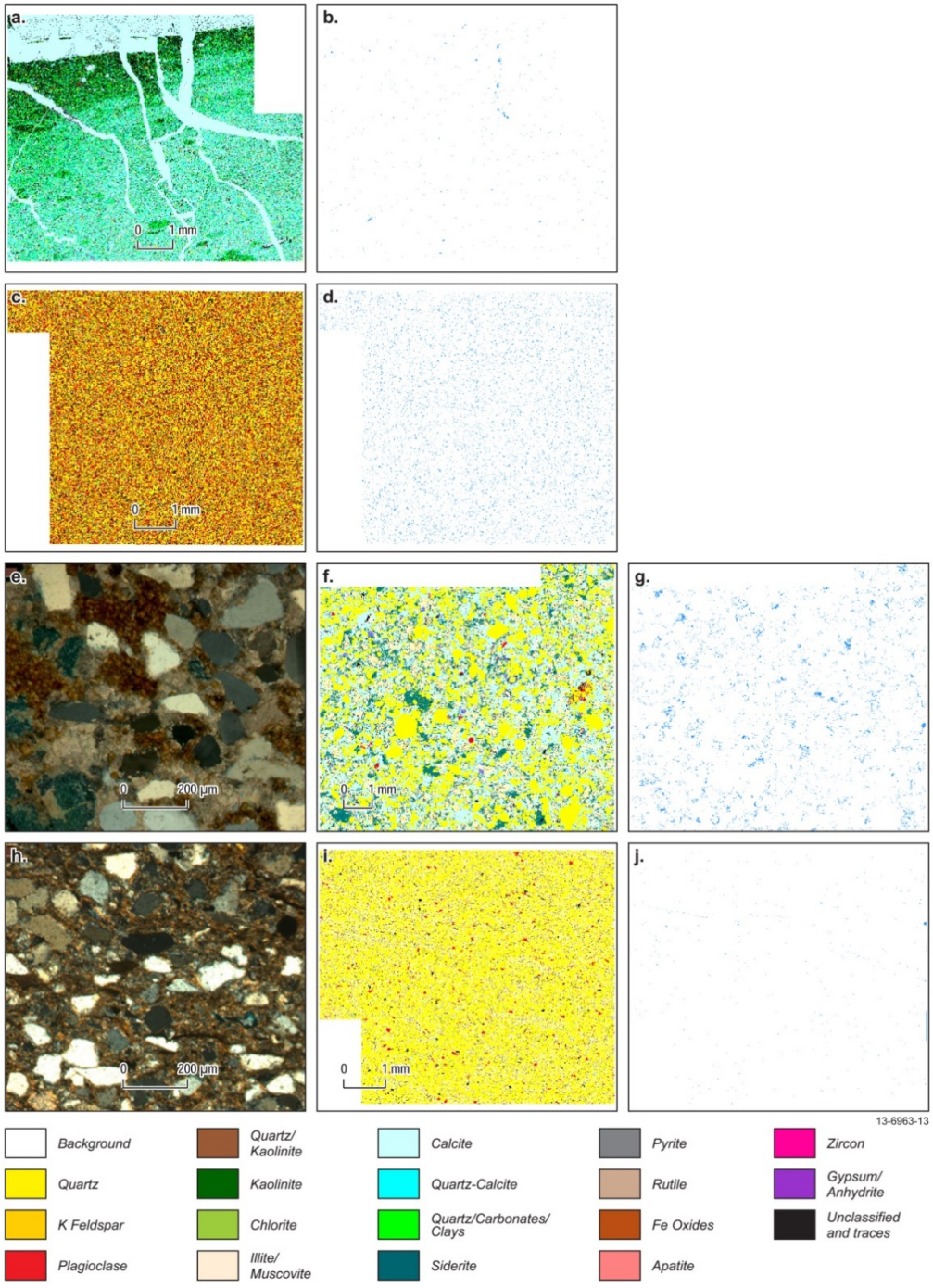

Figure 6.12 Photomicrographs and mineral and porosity maps for selected core samples of the Bathurst Island Group. (a-b) Wangarlu Formation, Petrel 1, 1603 m. (a) Mineral map. (b) Porosity maps, defined by regions with no minerals, blue equates to open pores (porosity). Mineral legend applies to (a). (c-d) Wangarlu Formation, Gull 1, 1536 m. (c) Mineral map. (d) Porosity map, defined by regions with no minerals, blue equates to open pores (porosity). Mineral legend applies to (c). (e-g). Darwin Formation, Jacaranda 1, 2868.6 m. (e) Thin section photomicrograph illustrating the occurrence of quartz and glauconite grains within carbonate cement and carbonate replacement of these grains, cross polarized light. (f) Mineral map. (g) Porosity maps, defined by regions with no minerals, blue equates to open pores (porosity). Mineral legend applies to (f). (h-j) Echuca Shoals Formation, Jacaranda 1, 2871.7 m. (h) Thin section photomicrograph illustrating the occurrence of quartz grains within clay and silt rich matrix, cross polarised light. (i) Mineral map. (j) Porosity maps, defined by regions with no minerals, blue equates to open pores (porosity). Mineral legend applies to (i). Note: scales in a, c, f and i, refer to images in b, d, g, and j, respectively. Thin sections taken from Appendix C and mineral maps are taken from Appendix E. Note: Mineral Maps defining quartz/kaolinite and unclassified and traces categories may include some smectitic components that are not resolvable.

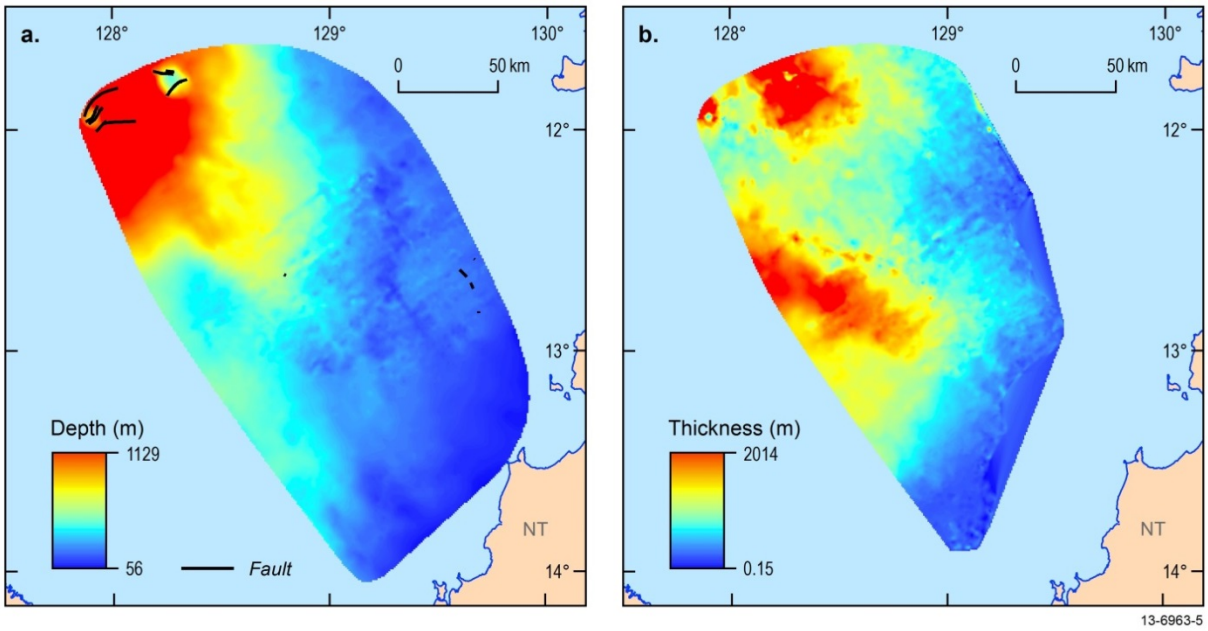

Figure 6.13 Depth (a) and thickness (b) maps of the Bathurst Island Group.

In total, 42 major faults that cut the Mesozoic–Cenozoic formations are mapped across the central and eastern flank of the sub-basin (Figure 2.4). These faults are grouped into five provinces based on comparable genesis, orientation and geographical location (Figure 6.14; Table 6.4), as follows:

1. Northwest-southeast trending normal conjugate faults (Province I).
2. South-eastern margin basin-bounding faults (Province II).
3. Eastern margin basin-bounding faults (Province III).
4. East-west trending normal conjugate faults (Province IV).
5. Salt diapir-related faults (Province V).

Geomechanical Analysis

The geomechanical analysis of these fault provinces aimed to constrain the in-situ stresses and rock strength and to evaluate the risk of fault reactivation and leakage. The stress regime of the Petrel Sub-basin is strike-slip based on well and earthquake data (Appendix I). The current regional maximum horizontal stress orientation is approximately in the northeast direction (54ºN; $S_{hmin}<Sv<S_{Hmax}$; Figure 6.15). In this stress regime, the fault reactivation risk was calculated using four scenarios with variable parameters. The four scenarios have variable S_{hmin} and S_{Hmax} ranging from minimal to maximum S_{Hmax} versus either lower bound or best-fit S_{hmin}. These broad ranges of scenarios would therefore probably incorporate the actual in-situ stress currently in the sub-basin (Figure 6.16; Table 6.5). Scenario one is viewed as the base case scenario and the results from that scenario will only be referenced.

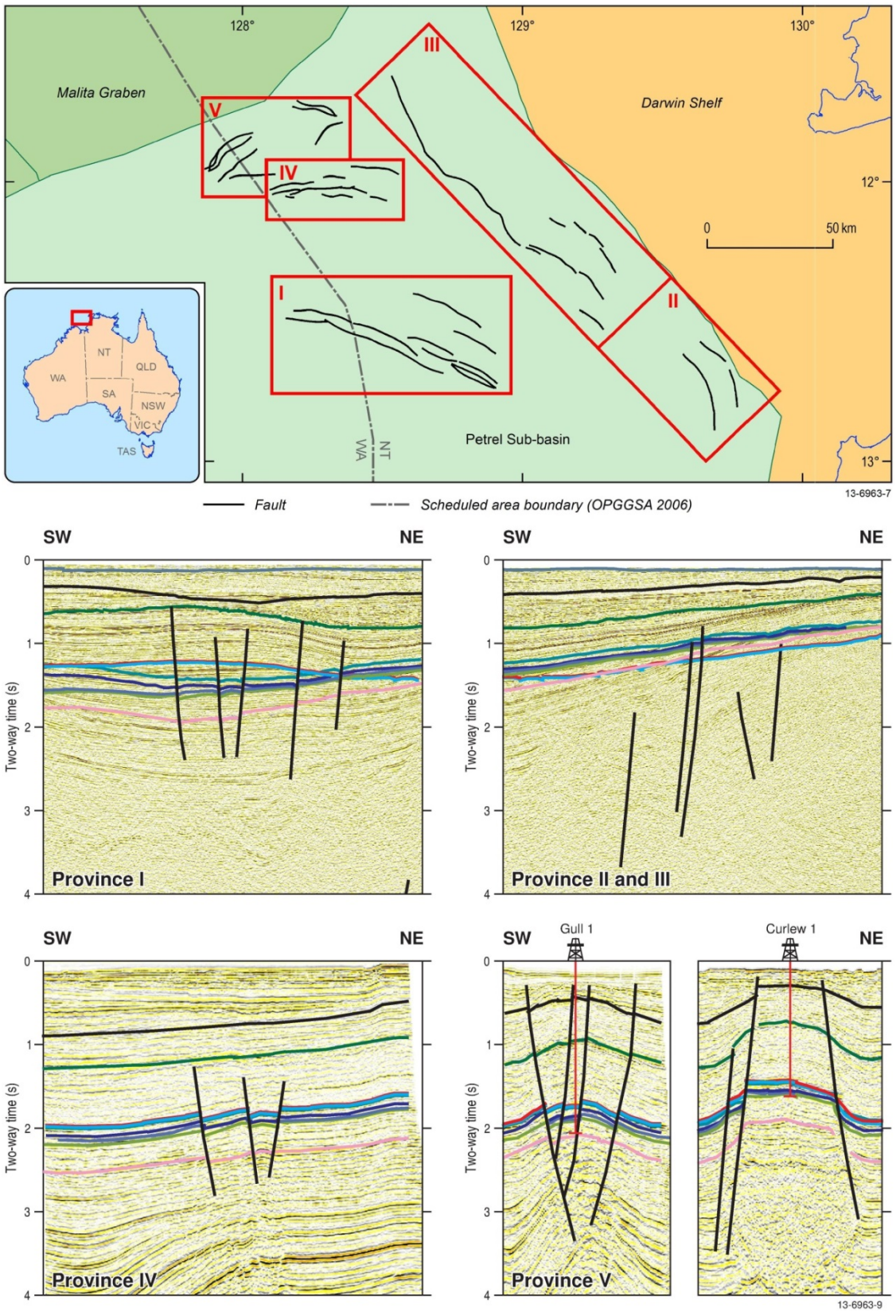

Figure 6.14 Structural provinces of this study. Province I, north trending conjugate, normal faults; Provinces II and III, basin-bounding faults on the eastern margin of the study area, Province IV, east trending conjugate, normal faults; Province V, salt-related faults.

Table 6.4 Fault summary for the Petrel Sub-basin.

Fault Province	Location	Genesis	Av. Orient.	Dip (°)	Max. Length (km)	Formation Age Intersection	Strat. growth	Throw Max. (m)
I	North and east of Petrel Gas Field	Normal; reactivated rift related	NW-SE	45-80	48	Triassic to Late Cretaceous	None	180
II	South-eastern margin	Normal; reactivated rift-related	NNW-SSE	30, 45, 60	45	Paleozoic to the Mesozoic	None	20
III	Eastern margin	Normal; reactivated rift-related	NNW-SSE	45 to 70	100	Paleozoic-Cretaceous	None	100
IV	Northern Petrel	Normal, unknown	E-W	50 to 70	20	Triassic to Early Cretaceous	None	120
V	Salt diapirs (Gull 1 and Curlew 1)	Normal; salt movement	E-W	50 to 70	23 (Gull 1) 16 (Curlew 1)	Carboniferous to ?Paleocene	None	300 (Gull 1) 660 (Curlew 1)

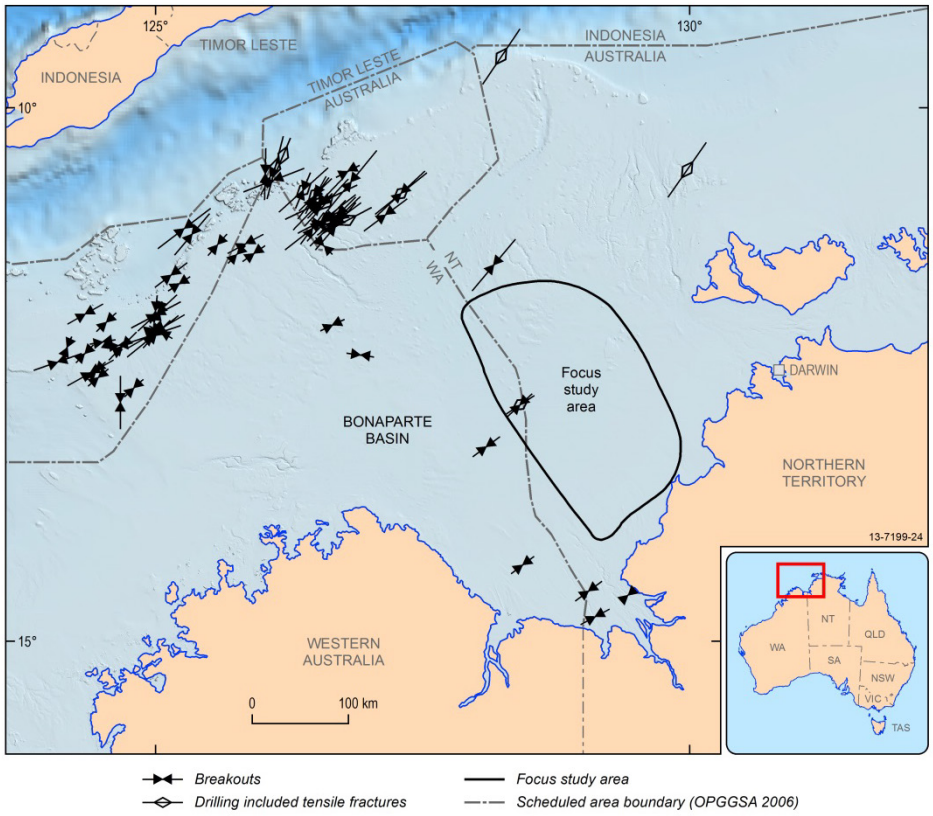

Figure 6.15 Stress orientations (SH_{max}) for the Timor Sea, from the Australasian Stress Map (modified after Hillis and Reynolds, 2000 and World Stress Map, 2008) Borehole breakout directions are very consistent through the Petrel Sub-basin, with an average trend 54°. Arrows are the maximum horizontal stress direction as measured by breakouts, from Figure 13 of Appendix I.

Table 6.5 Stress scenarios for the Petrel Sub-basin. Red values indicate difference from Scenario 1 (Base Case). Scenario 4 stress state is the only one which would be consistent with shale rock properties (from Appendix I).

Scenario:	1: min LOT, max SH	2: min LOT, min SH	3: fit LOT, max SH	4: fit LOT, min SH
Gradients (MPa/km) all through 0.6MPa at 60m (seabed)				
Pore-pressure gradient	9.93	9.93	9.93	9.93
Shmin gradient	14.89	14.89	17.40	17.40
SHmax gradient	24.67	21.00	32.70	21.00
Sv gradient	20.90	20.90	20.90	20.90
SHmax orientation	054	054	054	054
Rock properties				
Coeff. sliding friction	0.6	0.6	0.6	0.33
Coeff. internal friction	0.7	0.7	0.7	0.34
Cohesive strength MPa	5.00	5.00	5.00	2.75

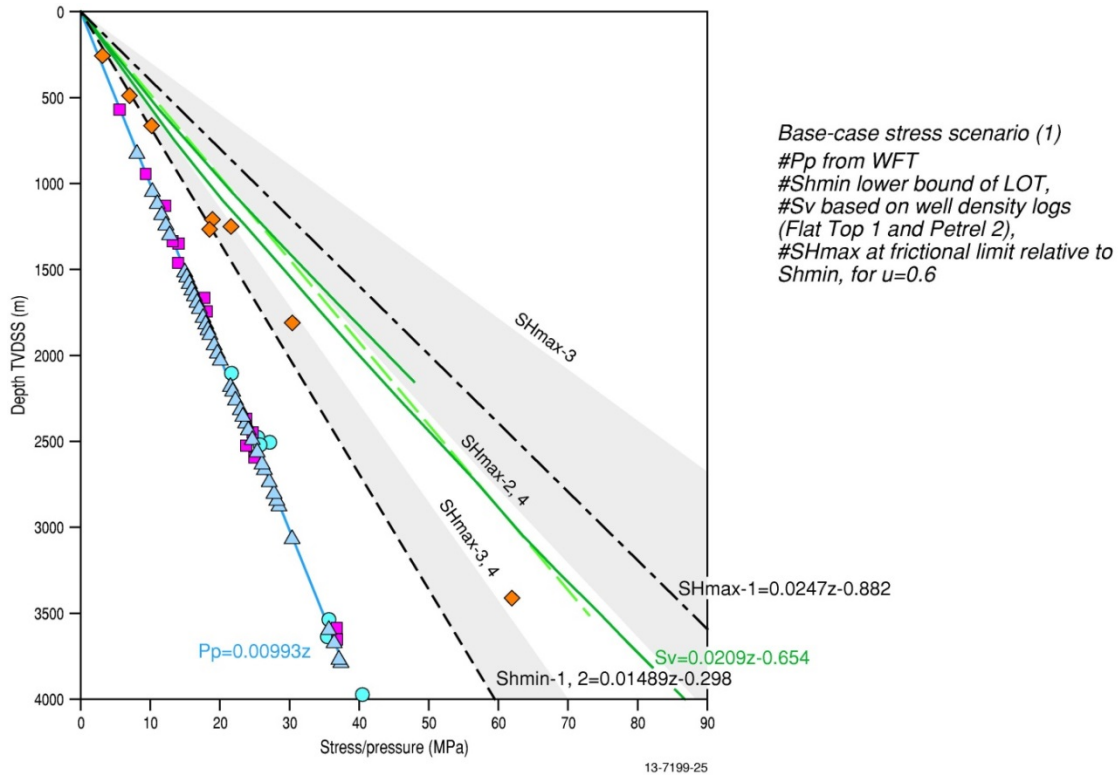

Figure 6.16 Petrel Sub-basin pressure and stress observations, and assumed gradients for the different model scenarios. Grey fields show the possible range for SHmax and Shmin parameters. In all cases, Sv is the intermediate stress indicating a strike slip regime for the sub-basin, from Appendix I.

Overall, the risk of reactivation was highest on faults orientated in an approximately east-west direction. Faults at most risk of slip (shear failure) are steeply dipping and striking 25-27° (north-northeast) and east-northeast (81-83°), which are symmetrically disposed about the SHmax orientation. These faults in the current stress regime are critically stressed and could become

preferential fluid pathways. Faults of this orientation include the faults of Provinces IV and V (Figure 6.14). Secondly, steeply dipping planes orientated in a northeast-southwest direction (perpendicular to Sh_{min}), such as the faults in Province V, would have a high dilational tendency that could result in the fracturing of high-cohesion (generally deeper) rocks. This also applied to faults at shallow depths with either low or high stresses, such as the faults in Provinces II and III.

For CO_2 geological storage, the effect of increasing pore pressure on the faults is an important risk assessment parameter. The slip and fracture stability can determine the maximum increase in pore pressure that a fault can sustain without deformation. It was determined that the amount of fracture is dependent on orientation. Overall stress and the rock strength both increase with depth, thus the slip and fracture stability also increases with depth. Therefore, a fault intersecting a shallow reservoir has a low stress state but requires a smaller increase in pore pressure to induce failure, including faults in Provinces II and III. In the deeper sections of the sub-basin, comprising faults in Provinces I and IV, the maximum pore pressure increase before fault failure was estimated to be greater than 5 MPa (based on slip stability); the fracture stability (hydraulic fracture) was even higher (Figure 6.17). Finally, local variations in the strike of large faults also influenced slip and fracture stability. For example, the geomechanical modelling of the faults revealed that east-west fault segments in the overall northwest trending faults of Province I and III have lower stability, which increases the deformation tendency on the faults at these segments.

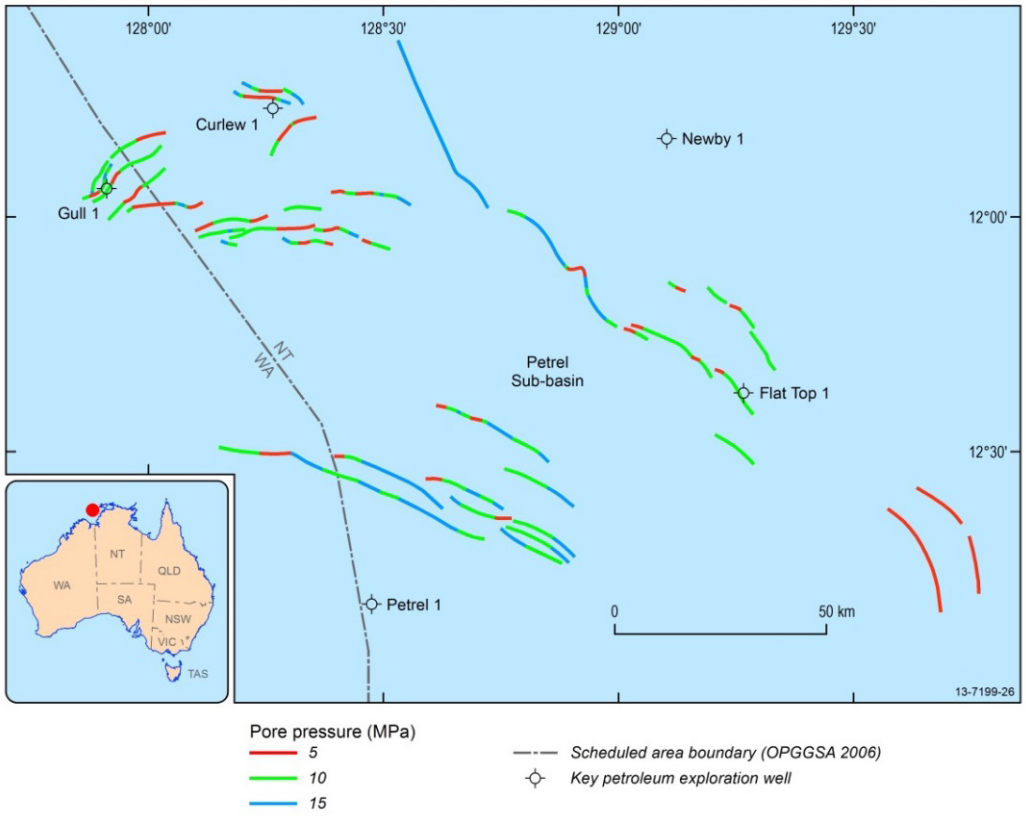

Figure 6.17 Simplified fault-trace map showing the theoretical pore pressure increase required for fault failure at reservoir levels (top Elang Formation, top upper Frigate Shale and top Sandpiper Sandstone). Fault segments coloured in red are most prone to reactivation if pressurised. Pore pressure is based on the minimum value of slip stability and fracture stability in Scenario 1, figure simplified from Figures 88-90 of Appendix I.

The geomechanical study also evaluated the reservoir juxtaposition and hydraulic properties of the faults. This study utilised the current seismic interpretation and conventional methods to determine the shale gouge ratio. The low stratigraphic throw on the majority of the faults has resulted in reservoir self-juxtaposition across the fault. With the current seismic interpretation, only two faults of Province V, within the Curlew 1 region, would have a juxtaposition connecting the Cretaceous reservoir and Jurassic reservoir. The geomechanical model of the faults indicates that the permeability in the fault planes varies widely, from 0.1 to 100 mD depending on the depth, orientation and methodology used to calculate permeability (Appendix I). In general, shallow clay-poor faults would have high permeability attributed to zones of disaggregation in the rock. This mostly corresponds to the faults on the eastern margin (Provinces II and III). The deeper clay-poor fault zones, generally attributed to fault Provinces I and IV, would preserve cemented cataclasites and thus have low permeability. Only through fault-rock permeability analysis of a cored section of a faulted interval could the large variation be better constrained and currently there are no core samples through a faulted zone. In summary, according to the base case Scenario One of the geomechanical study, fault Provinces II to V have some heightened potential for fault failure either due to orientation, dip, or depth. In terms of CO_2 geological storage, these areas of the Petrel Sub-basin are considered a low priority. In contrast, faults of Province I that have an overall low risk of deformation are also located in a region of high CO_2 geological storage potential.

Polygonal Fault Study

The presence of polygonal faults within the Bathurst Island Group has the potential to compromise the integrity of the lower portion of regional seal and therefore the overall CO_2 geological storage potential. As such, a detailed evaluation of their distribution and character was undertaken to assess their significance for the Petrel Sub-basin.

Polygonal faults form in a kinematically coherent manner with faulting and displacement occurring synchronously within the discrete layers. Faulting occurs typically within shallow burial depths (Gay et al., 2004; Berndt et al., 2012; Laurent et al., 2012). The actual catalyst for initial deformation is widely disputed with proposals ranging from overpressure, density inversion, and compaction and de-watering (Cartwright and Lonergan, 1996; Cartwright and Dewhurst, 1998; Lonergan et al., 1998; Watterson et al., 2000; Cartwright et al., 2003; Nicol et al., 2003; Cartwright, 2011). While details of these mechanisms vary between models, they all require the burial of fluid-saturated sediments rich in clay minerals. The ongoing deposition of very fine-grained sediments triggers polygonal faulting in the underlying (and previously undeformed) unit. The process repeats with the deposition of subsequent units. The new faults link to the lower units via relay faults and fractures.

The polygonal faults are distributed almost ubiquitously across the Petrel Sub-basin study area (Figure 1.4). The geometry, displacement patterns and stratigraphic-bound nature of the polygonal faults are comparable to polygonal faults seen elsewhere (Cartwright et al., 2003). The polygonal faults are planar or gently listric, with dips typically ranging from 30° to 70°, heights of <100 m, and typical lengths of less than 1500 m (Figure 6.18a, b). Individual faults have no defined orientation or trend, but intersect each other at high angles, with a central un-faulted horst of about 500-1500 m in diameter (Figure 6.18e-h).

The number of faults decreases near the base of the Bathurst Island Group where the grain size coarsens slightly, with only limited, inconclusive evidence on the seismic traces suggesting that faulting may extend into the underlying Sandpiper Sandstone. Polygonal faults are also not present in

the upper section of the Bathurst Island Group for the same reason, which is supported by the marine survey that found no link between the faulting and surface features, such as the pockmarks. Individual fault segments terminate at distinct layer boundaries to form a series of segmented, layer-bound arrays of normal faults over 10 stratigraphic intervals (Figure 6.18b). Due to the nature of layer-bound termination, no single polygonal fault forms a continuous trace through the entire sequence. Individual faults are possibly connected via relays forming a large, single linked fault system that spans the lower section of the Bathurst Island Group.

Fault intensity and displacement increases with depth and appears to be at its maximum within the Darwin Formation, dissipating rapidly into the Echuca Shoals Formation, near the base of the Bathurst Island Group (Figure 6.18c, d). The intensity of faulting in the Darwin Formation may either be related to the brittle nature of the carbonate-dominated formation, or an observational artefact caused by higher seismic amplitudes.

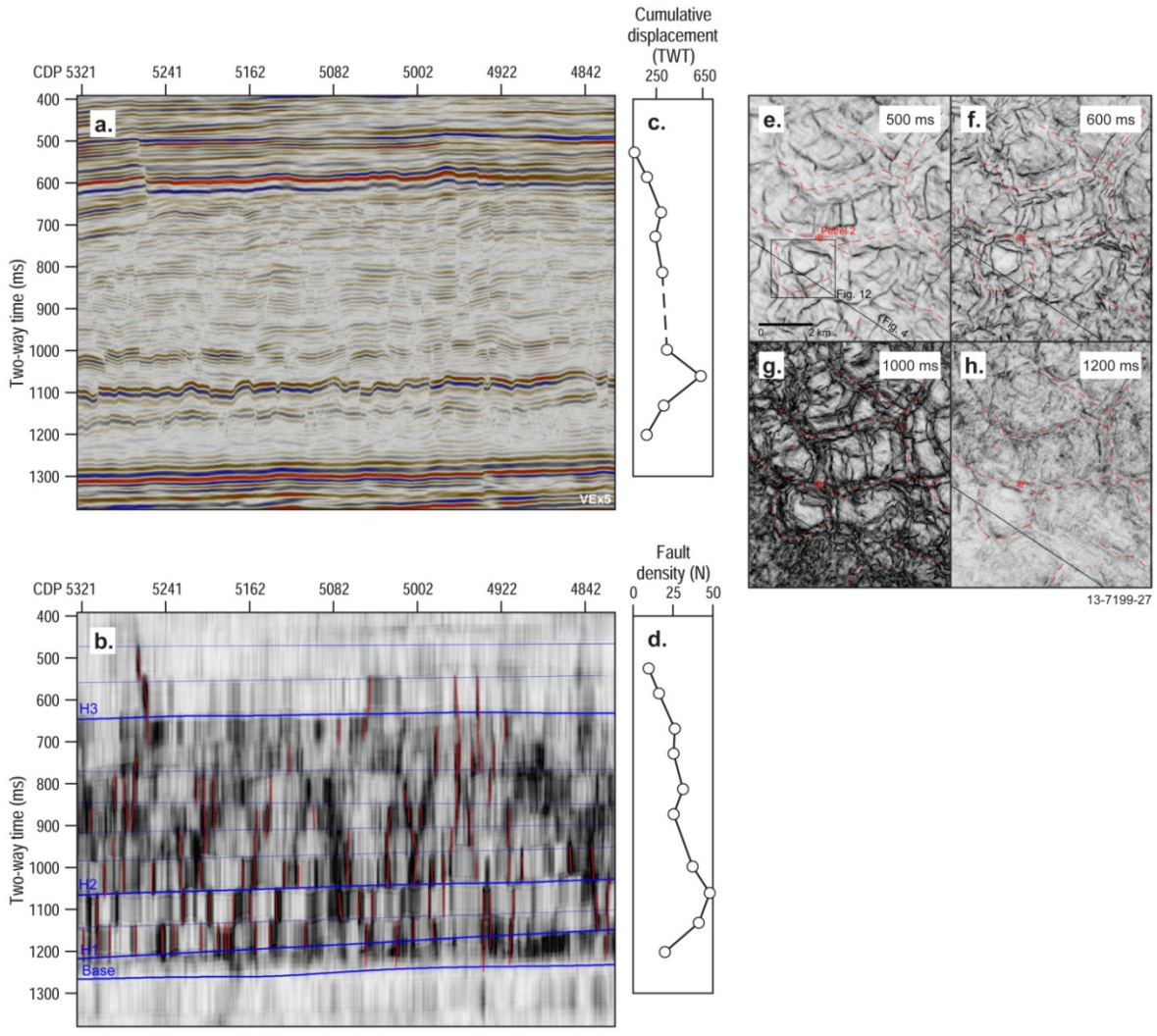

Figure 6.18 Selected seismic data from Petrel gas field 3D seismic survey showing evidence of polygonal faulting within the Bathurst Island Group. (a) Seismic reflection of Petrel 3D, a 12.5 km profile along Inline 1685 (See Figure 4.4 for survey location), and (b) corresponding interpreted coherency profile; coherency horizons (blue lines) and interpreted faults (red lines) show the layer bound nature of deformation. (c) Cumulative fault displacements for each coherency interval. (d) Density of faults for each coherency interval. (e)-(h) Polygonal fault geometry in plan view with coherency time slices within the Bathurst Island Group showing low coherence anomalies (black lineation) interpreted as polygonal faults. See Figure 4.4 for location of survey and Appendix N for full details.

6.3 Injection Simulation and Plume Migration

Static geological modelling, migration pathway analysis, and dynamic reservoir simulations are critical to evaluating the CO_2 geological storage potential of the two Mesozoic reservoir-seal pairs. This is because the CO_2 geological storage capacity, the injection rate potential and plume migration can only be realistically defined from these studies. The methodology to derive the models and results of the modelling are detailed in Appendix K (Static Model) and Appendix L (Numerical Reservoir Simulations).

Static Geological Model

Static geological models can improve the understanding of the evolution and depositional history of the Petrel Sub-basin (see Figure 4.6 for the geological model). Using geostatistical analysis, porosity values derived from petrophysical well log analysis were simulated throughout the model (Figure 6.19 and Figure 6.20; Appendix K). The porosity simulations were constrained within the major depositional regimes (e.g. lower shoreface) identified during the sedimentological and stratigraphical analysis (Appendix C). As a result, the porosity distribution of the geological model matched the facies distribution, as defined by the depositional models and observed stratigraphy (Appendices C and K).

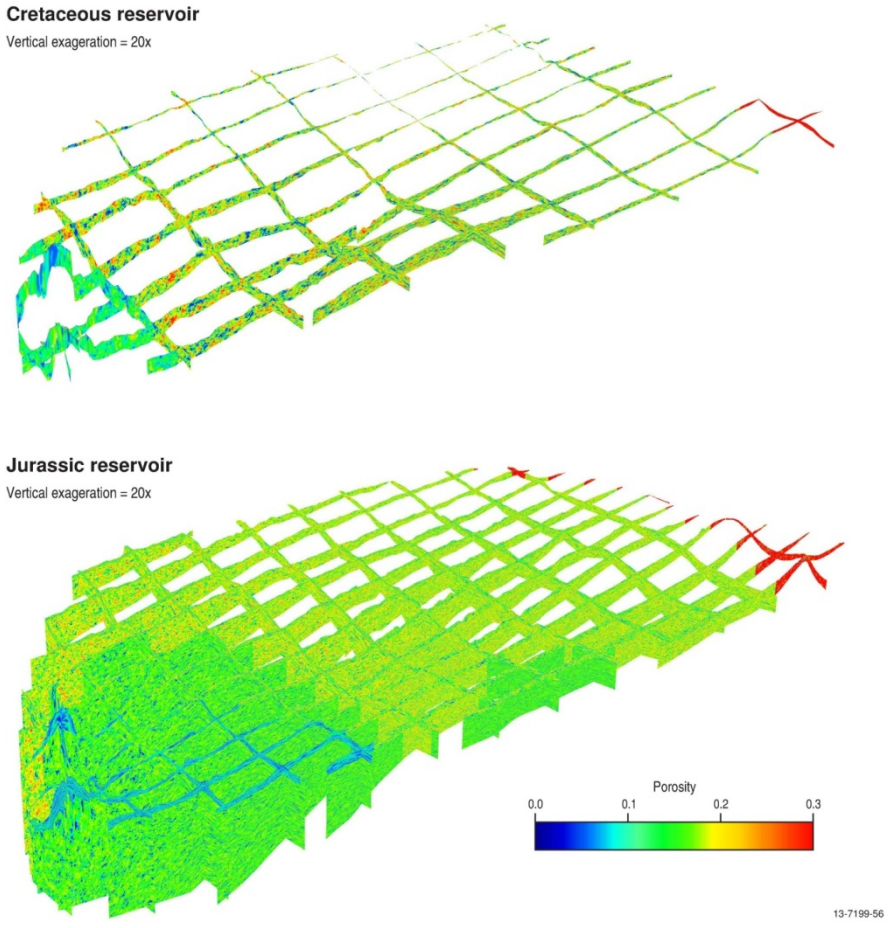

Figure 6.19 Fence diagrams from geological model showing simulated porosity distributions for the Cretaceous reservoir (top) and Jurassic reservoir (bottom). Diagrams are orientated with north to the left of the page and show the general deepening and thickening of the units to the northwest (bottom left corner) and the effects it has on porosity. See Figure 1.4 for location of the geological model and Appendix K for full details.

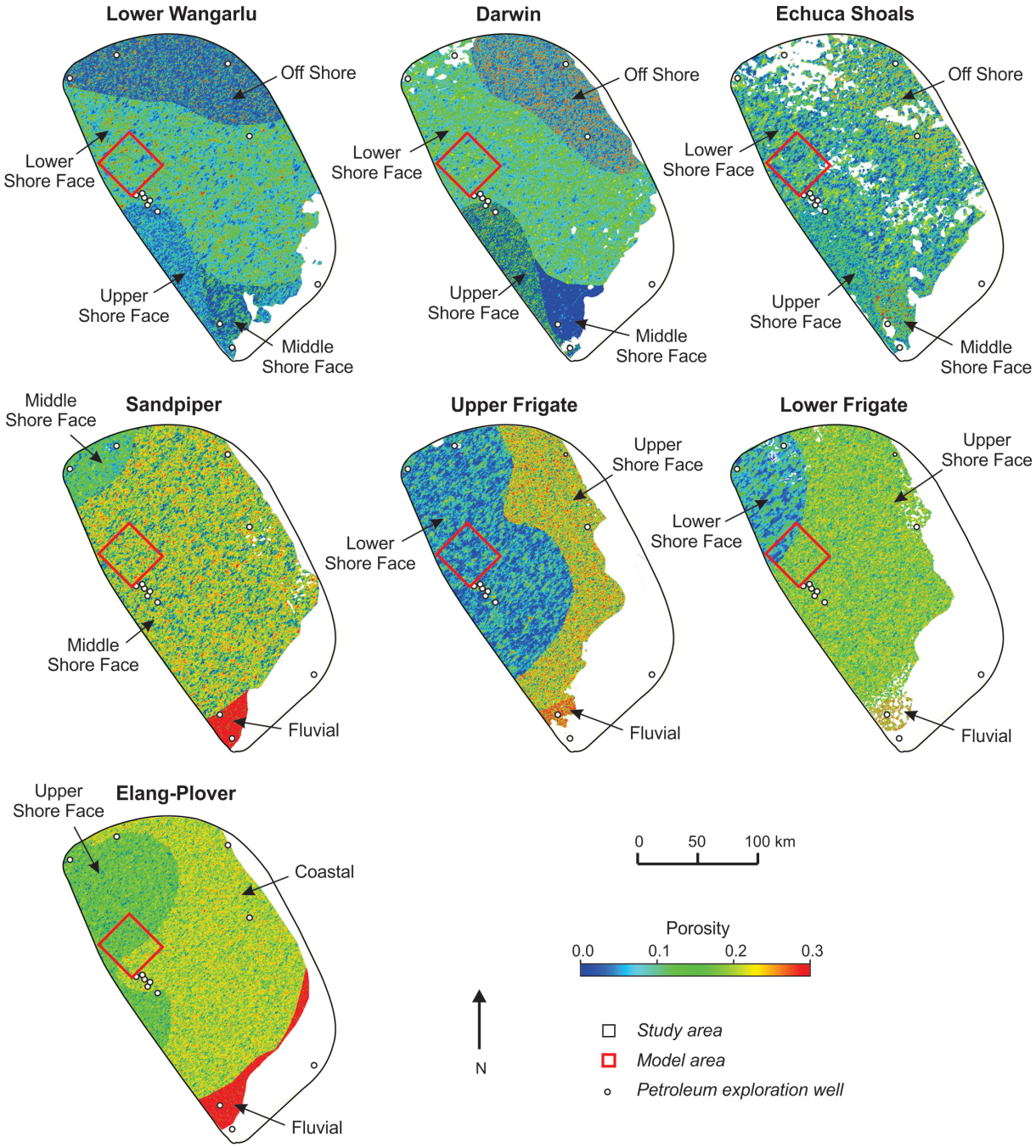

Figure 6.20 Maps showing simulated porosity values for the selected surfaces from the geological model. Abrupt changes in porosity patterns correspond to changes in depositional environment and sedimentary facies in the model unit. Depositional environments are labelled around the periphery. Top of page is north direction. See Figure 1.4 for location of the geological model. Red box outlines the location of the dynamic model. See Appendix K for full details.

Fill-Spill Analysis

Although not a reflection of CO_2 migration directly, the fill-spill analysis (see Section 4.2) revealed few structural closures throughout the study area, except for the salt diapirs of Gull 1 and Curlew 1. The analysis did reveal, however, that migration pathways predominantly were directed towards the shoreline (Figure 6.21; Appendix L), and lateral migration was almost directly east-southeast in the

northernmost region of the Petrel Sub-basin, becoming southeast in the south (Figure 6.21). This broadly follows the conclusions of the hydrodynamic study that showed a general flow from offshore to onshore (Appendix J).

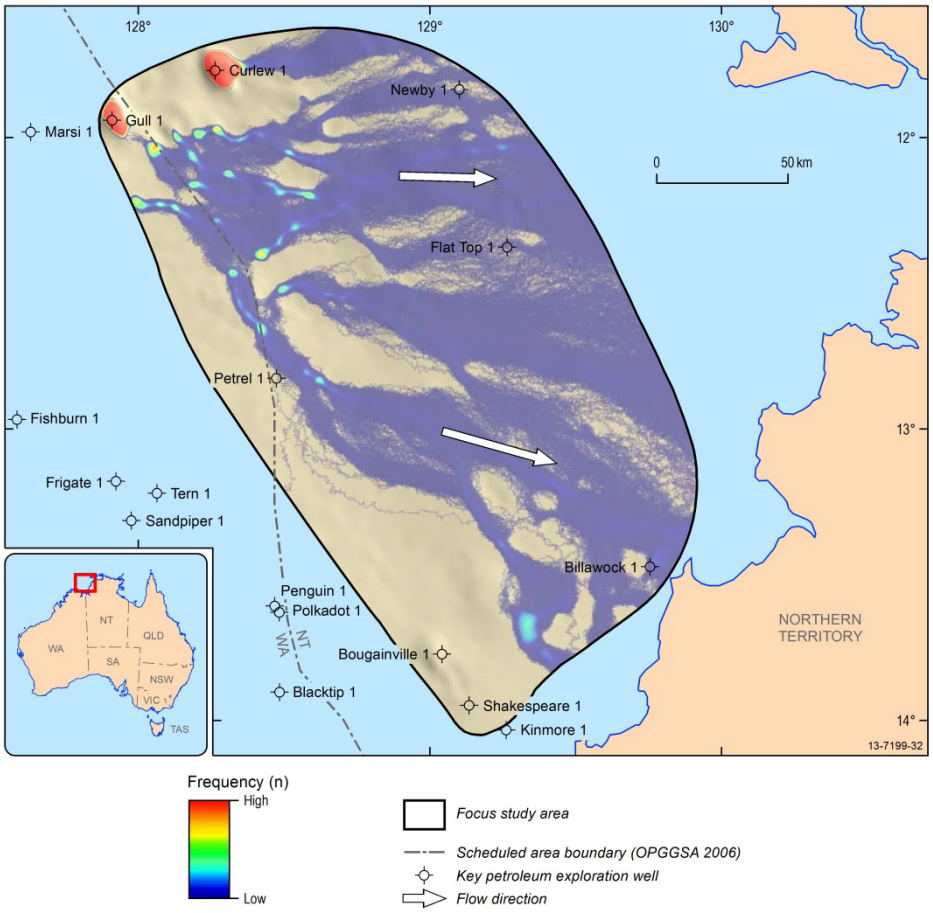

Figure 6.21 Fill-spill analysis of the top of the Elang Formation. Figure shows major structures along the base of the seal, including the salt diapirs at Bougainville 1, Gull 1 and Curlew 1, as well as the general trend of an easterly to south-easterly flow direction. Arrows indicate general flow direction. Note: This is not a flow simulation and prediction of CO_2 migration. See Appendix L for further information.

Dynamic Reservoir Simulations

The aim of the dynamic reservoir simulations was to simulate CO_2 injectivity, plume migration, CO_2 trapping phases and reservoir pressure behaviour in the Petrel Sub-basin. The likely injection region to the northeast of the Petrel gas field was chosen as the source of the CO_2 plume (Figure 1.4 and Figure 4.7).

The results of the dynamic reservoir simulations showed that 14 MTPA of CO_2 could be injected into the Jurassic-aged reservoir incorporating the Plover and Elang formations and lower Frigate Shale for a period of at least 30 years (Figure 6.22). This did not represent the maximum injection rate, but rather the estimated injection rate required to meet the predicted CO_2 emissions produced in the region over this time period (Carbon Storage Taskforce, 2009).

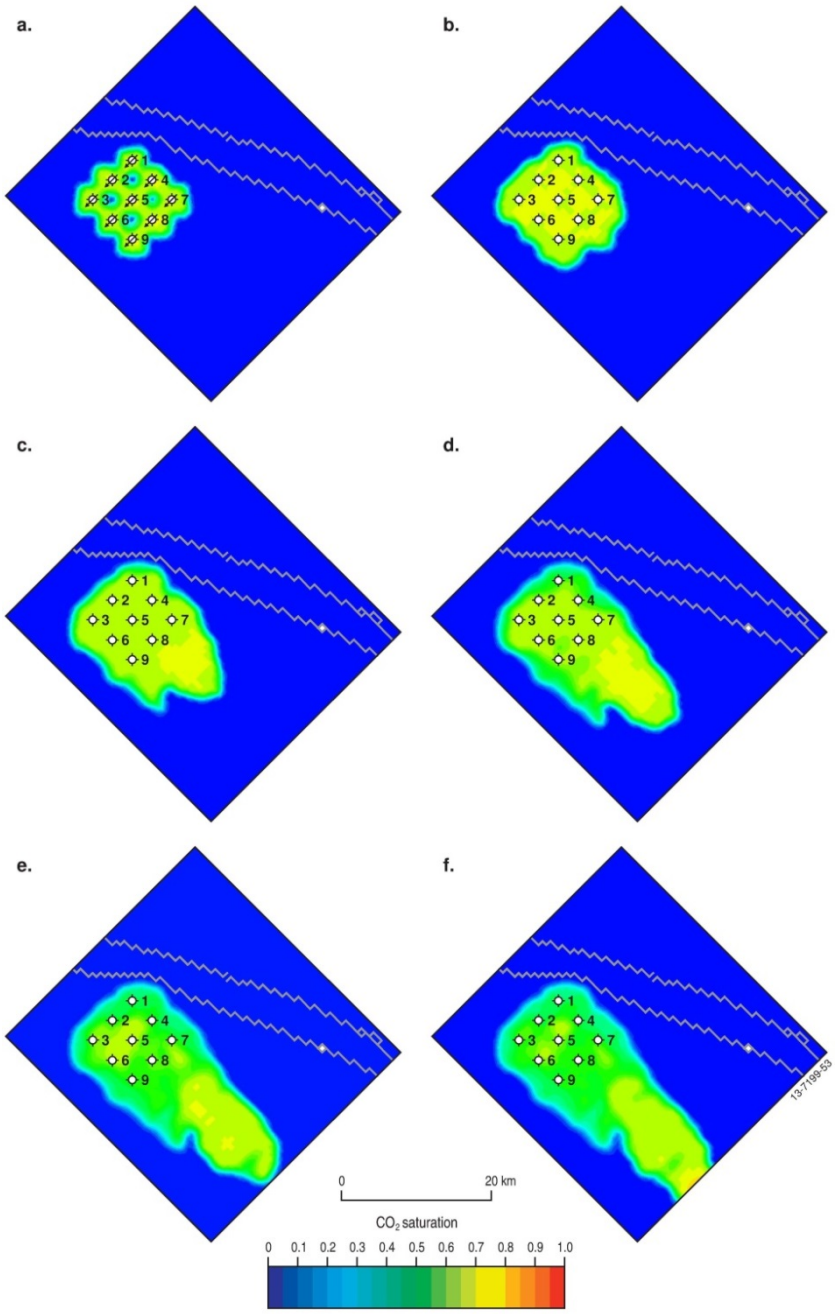

Figure 6.22 Plume migration simulation for Petrel North model area, showing CO_2 plume saturation after (a) 30 years (end of injection), (b) 100 years, (c) 500 years, (d) 1000 years, (e) 1700 years and (f) 2000 years. Jagged line objects are normal faults of Province I (see Figure 6.14). Top of page is north direction. See Figure 1.4 for location of the dynamic model and Appendix L for full details.

The dynamic reservoir simulations show that the vertical and lateral movement of the injected supercritical CO_2 did not extend laterally more than 5 km from each of the nine injection wells during the 30-year injection phase (Figure 6.22 and Figure 6.23). The maximum pressure increase at the wells did not exceed 3 MPa throughout. Over this period, CO_2-saline water dissolution was the dominant trapping mechanism, with the dissolved CO_2 concentrations increasing rapidly (Figure 6.24). At the end of the injection, a total of 420 MT had been injected into the Jurassic reservoir.

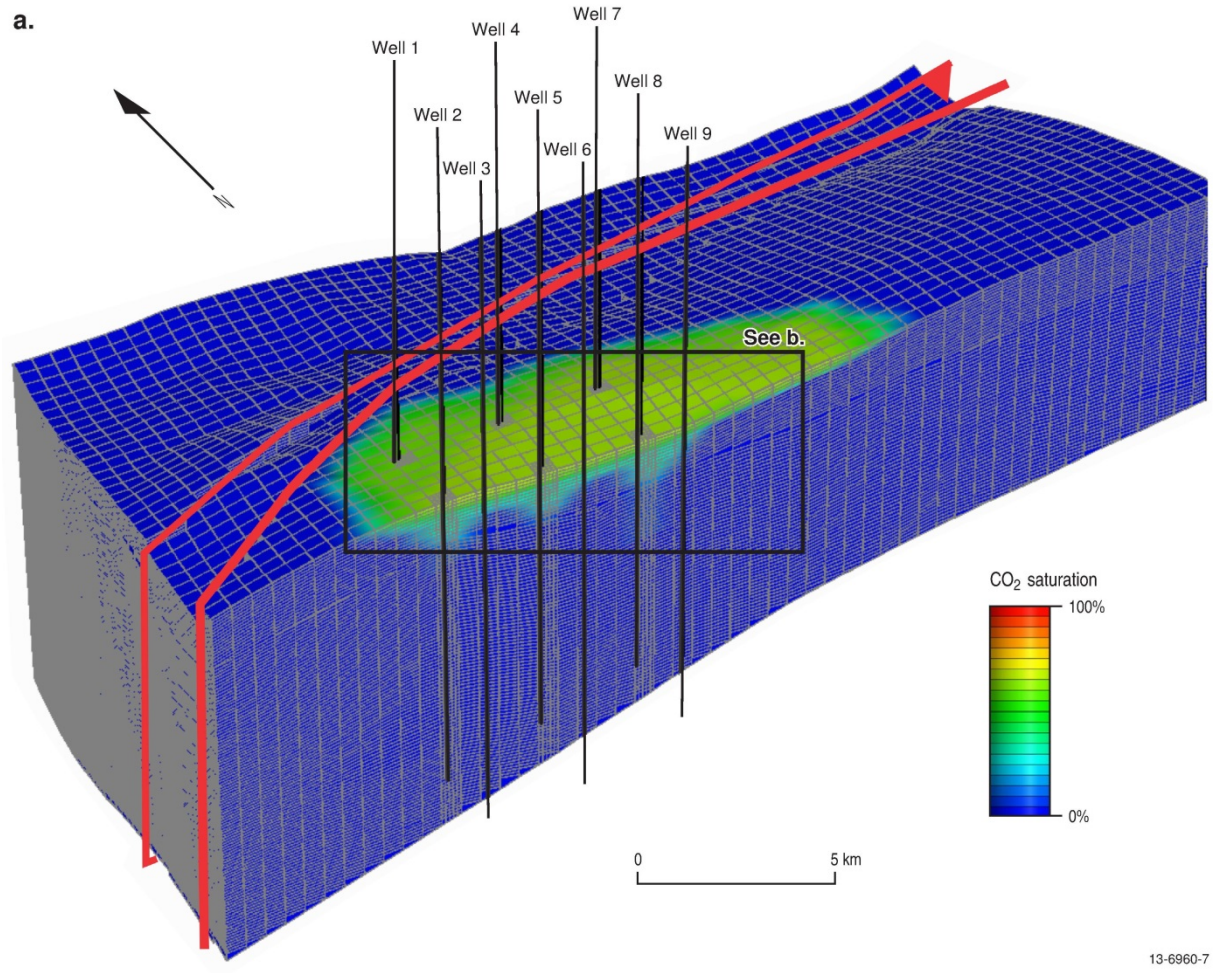

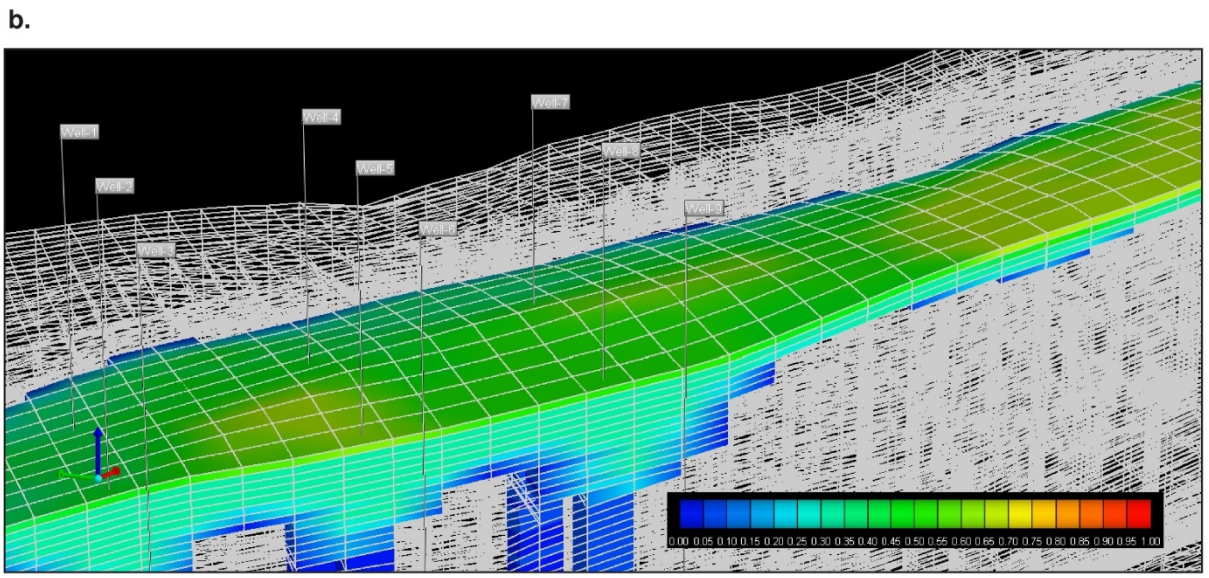

Figure 6.23 (a) CO_2 gas saturation distribution beneath the seal; red objects are the normal faults of Province I (see Figure 6.14); inset box (b). See Figure 1.4 for location of the simulation model and Appendix L for full details.

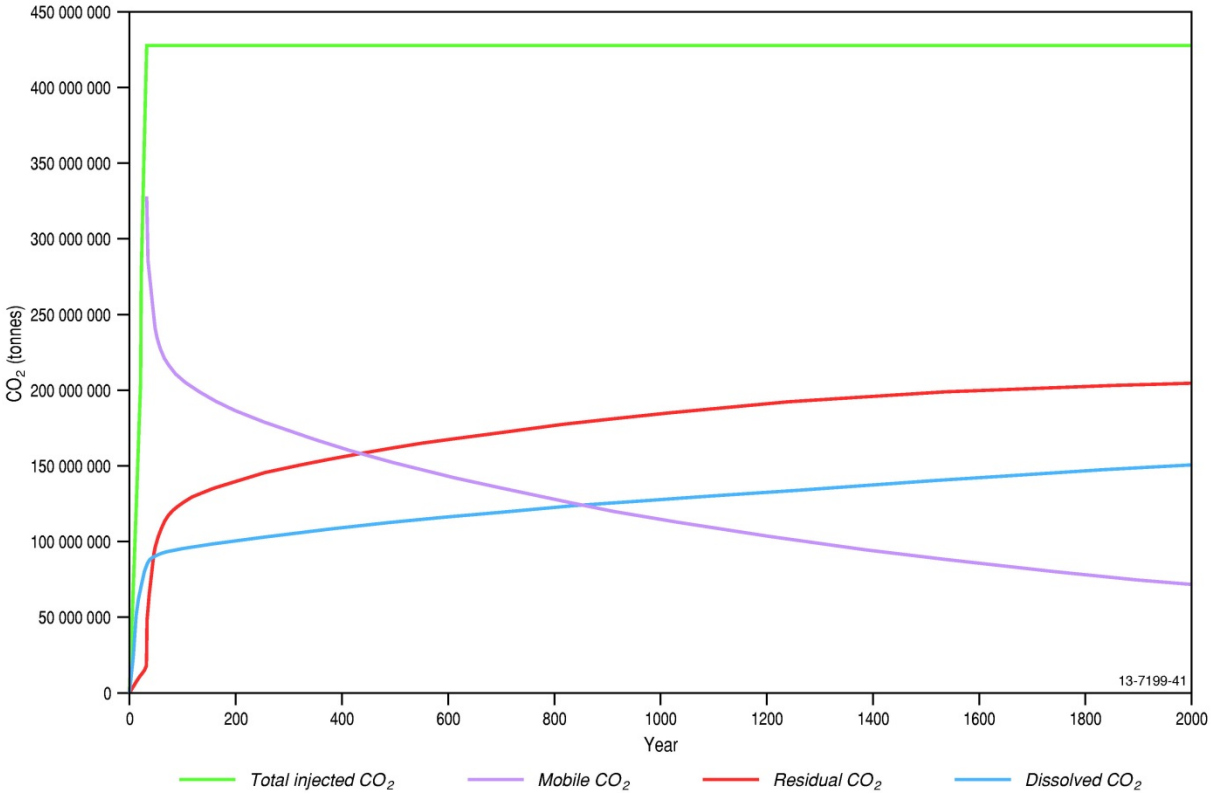

Figure 6.24 CO_2 residual and soluble trapping kept increasing and the amount of mobile (free) CO_2 decreasing as the CO_2 plume migrated until all CO_2 would be trapped. See Appendix L for full details.

Approximately 20% of the total injected CO_2 was trapped in solution and dissolution trapping slowed significantly after the end of the 30 year injection (Figure 6.24). The amount of CO_2 trapped as residual CO_2 rapidly increased over this same period as free CO_2 reached the seal and subsequently migrated slowly up dip (southeast). Once injection stopped, the reservoir pressure rapidly declined to its initial state.

After 100 years from the initial injection date, over 50% of the injected CO_2 was trapped in the reservoir. At this time, it was predicted that approximately 100 MT of CO_2 was trapped in solution and 125 MT of CO_2 was trapped as residual CO_2 (Figure 6.24). After 1,700 years, 250 MT or 83% of the total injected CO_2 was trapped; the remaining 17% remaining mobile supercritical CO_2 gas migrating up dip. Extrapolating the simulated CO_2 trapping and migration rate, the model predicted that it would take total 3200 years before 100% of the injected CO_2 would be permanently trapped, by which time the CO_2 plume would have migrated a total distance of 34 km up dip from the injection wells.

In a separate simulation, 5 MTPA of CO_2 could be injected into the Cretaceous reservoir over the 30 year injection period. Injection into the Cretaceous reservoir was limited by the thin reservoir thickness and shallow injection depth. This shallow, thinner reservoir resulted in shorter perforation intervals, lower injection pressure limits and lower CO_2 density, producing a lower total injection.

7 Capacity

The classification of capacity estimates is currently defined by the 'levels' of the CO_2 storage resource pyramid (Figure 7.1; CO2CRC, 2008; Carbon Sequestration Leadership Forum, 2011). In each step towards the apex, there is an increasing level of certainty in the storage space, increasing confidence of the reservoir and seal characterisation, increasing quality and resolution of data and finally, but not always, a decreasing estimated volume of the storage space available. In order to calculate the capacity at each of these steps there are a variety of methodologies of varying complexity and input requirements. Details of the various CO_2 storage classification pyramids, including the history of capacity methodologies in Australia, are provided by Bunch (2013).

In the present study, the effective storage capacity was defined at the formation level to improve the level of certainty and increase confidence over previous estimates. The effective storage capacity represents a fraction of the total rock volume capacity. It is obtained by applying a range of geological and engineering cut-off limits to this total potential storage volume. These cut-offs are employed through a simple volumetric calculation where the properties of the fluid and the reservoir are held constant. The volumetric calculation methodology utilised for this study follows Bradshaw et al. (2009), which was identified by Bunch (2013) as one of the most robust capacity methodologies published. Importantly, the static geological model and dynamic reservoir simulations were used to constrain the inputs into the calculation of CO_2 storage capacity. The variability of the inputs was evaluated using a Monte Carlo simulation, which addressed the uncertainty in the values and produced probabilistic effective storage capacity estimates for the Jurassic and Cretaceous reservoirs, as well as the reservoirs combined. Full details of the procedure used to calculate the CO_2 geological storage capacity for the Petrel Sub-basin are provided in Appendix O.

The total effective storage capacity for the study area is estimated to be 15,930 MT (P50 or best estimate; Table 7.1). The total effective storage capacity is the probabilistic sum of effective storage capacity of the Jurassic and Cretaceous reservoirs, and not simply the addition of the two. The regional effective storage capacity of the reservoirs, limited by their respective seals, is 6,480 MT (P50) for the Jurassic reservoir and is 9,310 MT (P50) for the Cretaceous reservoir.

The Jurassic reservoir has a lower capacity when compared to the Cretaceous reservoir due to the limited spatial extent of the upper Frigate Shale mudstone seal. Moreover, despite the Jurassic reservoir being thicker overall, migration-assisted trapping (the likely trapping mechanism for this play) will only utilise the upper tens of meters of the reservoir and hence not occupy the entire reservoir pore space (Figure 7.2). The calculation contained in Bradshaw et al. (2009) is one of only a few methodologies to not define the entire reservoir pore volume as storage space which is typical of most volume estimate methods for CO_2 storage capacity (Figure 6.23b).

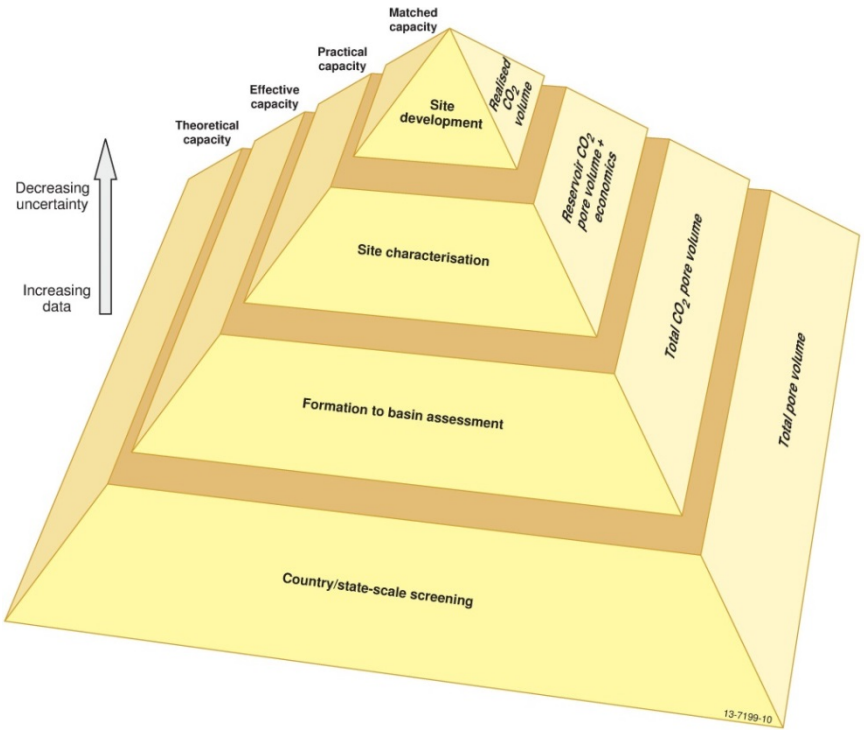

Figure 7.1 Pyramid of resources after Carbon Sequestration Leadership Forum (2011) and CO2CRC (2008).

Table 7.1 The effective storage capacities using Monte Carlo simulation. The Jurassic and Cretaceous reservoirs capacity estimates are independent in the simulation and the total reservoir capacity are the result of the probabilistic sum of both reservoirs in Monte Carlo simulation.

Monte Carlo simulation results (Gt)			
Percentiles	**Jurassic Reservoir**	**Cretaceous Reservoir**	**Total Reservoir**
P0	1.59	2.29	6.58
P10	4.66	6.30	12.29
P20	5.19	7.09	13.43
P30	5.63	7.83	14.33
P40	6.05	8.57	15.13
P50	6.48	9.31	15.93
P60	6.92	10.07	16.74
P70	7.39	10.87	17.61
P80	7.94	11.77	18.65
P90	8.67	12.99	20.02
P100	11.77	16.93	26.91

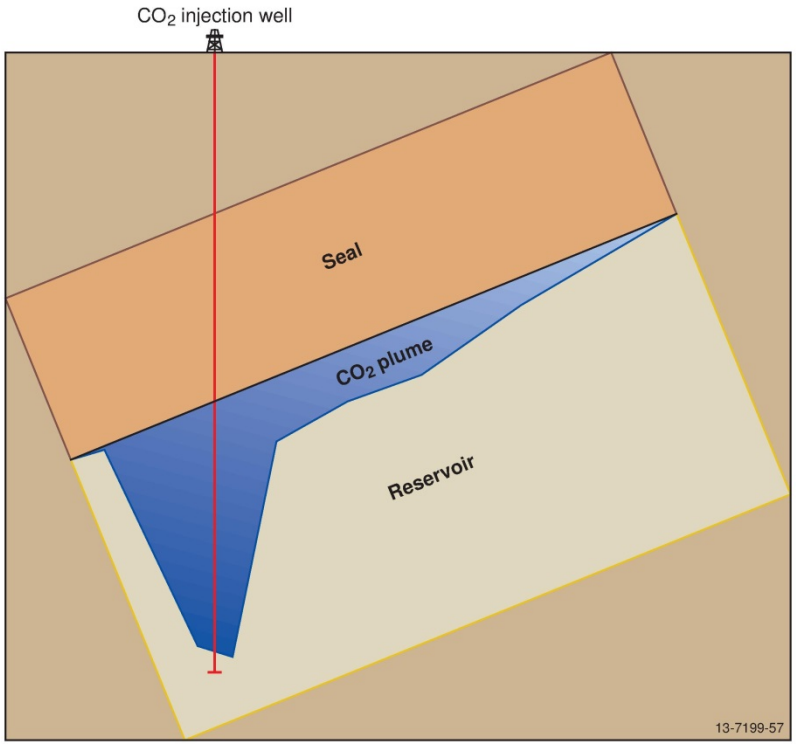

Figure 7.2 Simple schematic of a migration-assisted storage play in a theoretical CO_2 injection scenario. Away from the wells, the CO_2 plume only utilises the upper section of the reservoir immediately below the reservoir-seal boundary.

The logic behind this methodology is supported by the results of the dynamic reservoir simulations. The simulations predicted that, away from the wells, only the top tens of meters below the reservoir-seal boundary are utilised for CO_2 geological storage (see Figure 6.23b for an example). Therefore, due to the extensive nature of both the Cretaceous reservoir (Sandpiper Sandstone) and regional Cretaceous seal (Bathurst Island Group) this reservoir would have a higher effective storage capacity. This result is in contrast to the findings of the reservoir simulation results of the Cretaceous reservoir, which found that the overall injection rates need to be smaller due to pressure build-up in the Cretaceous reservoir. This contrast in findings highlights the complexity and the impact of the methodology used on capacity storage estimates. A regional-based dynamic reservoir simulation could provide a more robust capacity estimate but was beyond the scope and timeframe of this study, which would require a large-scale geological model (and supporting reservoir-seal characterisation analysis) and subsequent large computing power. Finally, the effective storage capacity calculations are highly dependent on the geological model, which as with all geological models has some degree of uncertainty.

In conclusion, the capacity values of 6,480 MT (P50) for the Jurassic reservoir and 9,310 MT for the Cretaceous reservoir above represent the best estimates available using the current datasets (Table 7.2). Static geological modelling and dynamic reservoir simulations are valuable tools supporting a robust calculation of the CO_2 geological storage capacity estimates. The static effective storage capacity estimates are important for CO_2 geological storage prospectivity study as they predict the total regional capacity and enable the capacity estimates to be compared to other basins for national prospectivity assessments. The dynamic reservoir simulations provide the injectivity potential of the reservoirs and refine the input data into the effective storage capacity calculations.

Table 7.2 Estimated potential storage and input data quality summary.

Effective Storage Capacity Estimation- Data Quality		**Comments**
Structural surface constraints	Good	Extrapolated from well data using 2D seismic surveys (average spacing 2-5 km), but sub-basin is structurally simple.
Reservoir thickness constraints	Good	As above; net reservoir isopachs derived from geological model.
Reservoir porosity constraints	Fair	Geological model-derived extrapolation of sparse well data; porosity values derived petrophysical analysis and rare core measurements.
Reservoir gas saturation constraints	Average	Maximum residual gas saturation used; derived from the petrophysical defined porosity of this study and the theoretical residual gas saturation correlation of Holtz (2002).
Carbon Dioxide Density Estimation- Data Quality		Comments
Temperature Profile Constraints	Probable	Well completion report data using Horner corrected temperatures.
Pressure Profile Constraints	Probable	Well Completion Reports (wireline and DST tools).
Estimated regional potential storage	15.93	Gigatonnes (effective storage capacity)
Estimated potential storage	300	TCF

8 CO_2 Geological Storage Potential of the Petrel Sub-basin

Migration-assisted storage (MAS) has been identified by migration pathway analysis on the eastern flank of the Petrel Sub-basin as the only potential CO_2 geological storage play in the Petrel Sub-basin. No large structural traps were identified away from the known halokinetic traps at Gull 1 and Curlew 1. The general migration of CO_2 was up dip (i.e., to the southeast, towards the margins) and controlled by the overall northwest dip of the sub-basin, as defined by the hydrodynamic analysis (Appendix J) and dynamic reservoir simulation (Appendix L).

Overall, the Petrel Sub-basin study area is evaluated as highly prospective for CO_2 geological storage based on geological evidence. The study area meets a standard set of criteria for regional CO_2 storage assessment, as follows:

1. Adequate seal:
   - Seal Quality: a seal with sufficient thickness and lateral extent to restrict CO_2 to the underlying reservoir over a large area.
   - Seal Capacity: an ability to withstand additional pressures from CO_2 buoyancy and injection.
   - Seal Integrity: an absence of faulting and / or the benign geomechanical response of the faults to the addition of CO_2.
2. Reservoir quality:
   - Reservoir Injectivity: sufficient extent, thickness and permeability for 100% injection.
   - Reservoir Capacity: sufficient volume of pore-space available.

Based on the above criteria and analysis of the geological and geophysical data, different regions of the Petrel Sub-basin are classified as Highly Suitable (28% of the total study area), Suitable (15%), Possible (20%), and Unlikely (37%) for CO_2 geological storage (Figure 8.1).

8.1 Highly Suitable

The centre of the Petrel Sub-basin, extending between 50-70 km to the north, east and south of the Petrel gas field, has the greatest potential for CO_2 geological storage and is therefore classified as Highly Suitable (Figure 8.1).

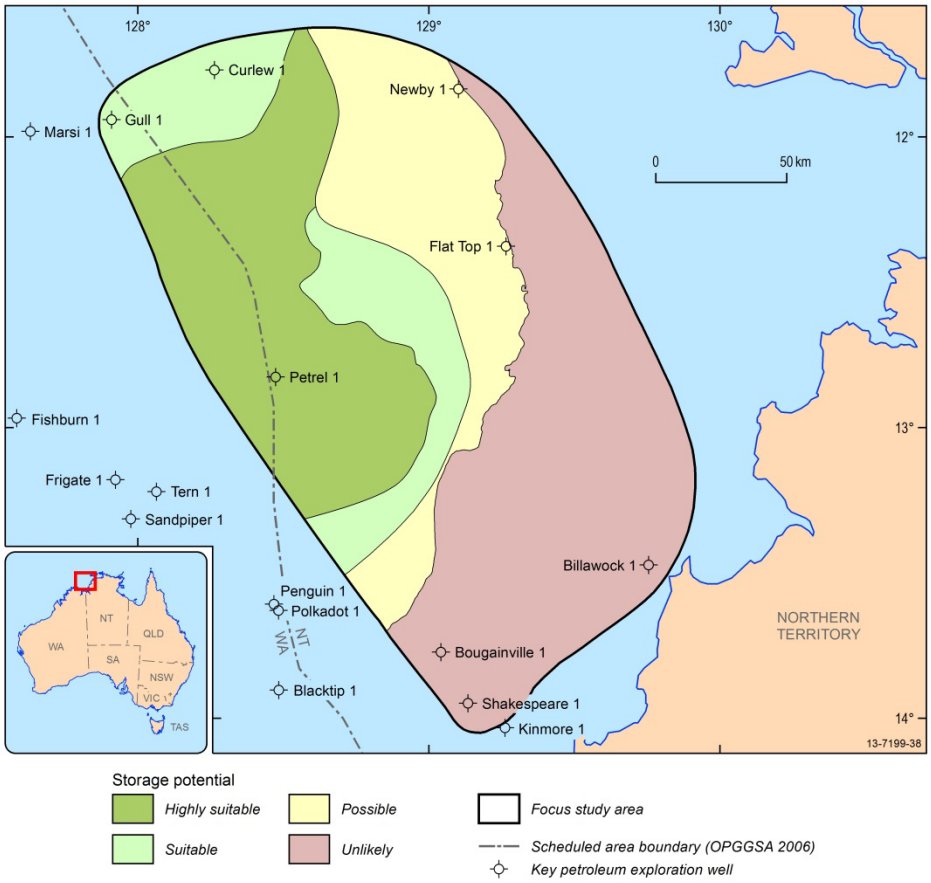

Figure 8.1 CO_2 storage potential of the study area.

In this area, the composite Jurassic reservoir comprises extensive, high quality sandstones with good connectivity. Thin, localised siltstones and mudstones within this reservoir act as potential baffles to vertical plume migration. This could increase the overall displacement of the CO_2 plume and increase the rate of solution and residual trapping. This composite reservoir is effectively sealed by the upper Frigate Shale. Well and seismic data, including seismic inversion analysis, indicate that the mudstone facies of the upper Frigate Shale covers the majority of the deeper Petrel Sub-basin. Geological modelling predicts that the seal capacity of the mudstone facies to be sufficient to contain the expected CO_2 column in the underlying reservoir. This is based on two factors: (1) the storage play for the Petrel Sub-basin is MAS and therefore a very high CO_2 column height will not be encountered. This is in contrast to the high CO_2 column heights which would be found in a structural storage play; and (2) the seal capacity measurement was taken from a sandier section of the Frigate Shale near the contact with the Sandpiper Sandstone and therefore it is conservative to predict higher threshold pressures in the mudstones in the lower section. Finally, simulation modelling predicts that an injection rate of 14 MTPA over 30 years (total 420 MT) could be achieved in the Jurassic reservoir and that the injected CO_2 plume would not migrate beyond the mapped extent of the mudstone facies of the upper Frigate Shale.

The Cretaceous Sandpiper Sandstone and Bathurst Island Group form the second reservoir-seal pair. The reservoir comprises extensive, porous and permeable sandstones but its shallow depth and relatively thin extent means that it can only accommodate lower injection rates of 5 MTPA of CO_2 for 30 years (for a total of 150 MT). The Bathurst Island Group is an effective seal for this reservoir. Seal

capacity measurements, determined from numerous threshold pressure tests, show CO_2 column retention heights ranging from 137 to 365 m, an averaging around 225 m (Figure 6.9). The thickness of the underlying reservoir in a MAS scenario would not be higher than the predicted CO_2 column retained. With respect to seal integrity, the seal contains only one set of faults that could affect the CO_2 geological storage potential. Geomechanical analysis indicates that the northwest-southeast striking faults of Province I have a low tendency for slip and dilation, with high fracture and seal stability. Fault stability decreases slightly up-section on faults present in the Bathurst Island Group, but any reservoir pressure changes associated with CO_2 storage are unlikely to affect these faults. This is supported by the dynamic reservoir simulations, which indicate that the predicted pore pressures changes required for fault reactivation would not be achieved even in the reservoirs.

8.2 Suitable

Two areas are identified as Suitable for CO_2 geological storage in the Petrel Sub-basin (Figure 8.1). The first is located to the east of the Petrel gas field and is defined by the transition zone from the upper Frigate Shale mudstone facies to the sandy facies. This transition zone is marked by the toe of the progrades of the upper Frigate Shale, representing the minimum mudstone extent. The top of the progrades was defined as the maximum probable extent (Figure 6.8). This seismic facies interpretation is supported by seismic inversion analysis (Figure 6.5). The second area is located to the north of the study area, centred on the salt diapirs, and comprises two reservoir-seal pairs. This area was classed as Suitable based on the findings of the geomechanical fault study which predicted that the faults have increased reactivation susceptibility in this area. Furthermore, well data indicate that the reservoir quality is diminished in the deeper parts of the Petrel Sub-basin due to burial and compaction. Despite this, the two reservoirs and seals in this area are deemed effective for CO_2 geological storage.

8.3 Possible

One area of the Petrel Sub-basin was classified as Possible for CO_2 geological storage (Figure 8.1). This area occurs only where a single reservoir-seal pair exists. Well and seismic data indicate that a single reservoir, from the lowermost Plover Formation through to the top of the Sandpiper Sandstone, exists in this area and is sealed by the overlying Bathurst Island Group. The geological model predicts that the reservoir quality is good to excellent for injection, based on the well data at Bougainville 1 and Flat Top 1. Seismic mapping shows the Bathurst Island Group is still present as a thick, continuous mudstone across this area. Therefore, given that this area comprises a good reservoir and effective seal, it is a plausible site for CO_2 geological storage despite consisting of a single reservoir-seal pair. In addition, much of the area classified as Possible for CO_2 geological storage is proximal to the supercritical CO_2 boundary depth of 800 m. This increases the likelihood that a CO_2 plume could migrate into shallow depths and the CO_2 could transform from a supercritical phase into a sub-critical phase. This reduces the overall storage efficiency for the reservoirs in this location.

8.4 Unlikely

The remainder of the Petrel Sub-basin reservoirs are shallower than the 800 m supercritical CO_2 depth and have been classified as Unlikely for CO_2 geological storage (Figure 8.1). However, CO_2 geological

storage is still technologically feasible above 800 m depth if the plume can be permanently trapped and does not migrate to the large basin-bounding faults where there is a higher risk of leakage.

8.5 Remaining Uncertainty

Although the polygonal faulting in the Bathurst Island Group has been studied in detail and the potential that the faults may compromise the regional seal integrity remains unresolved, it is concluded that the Bathurst Island is still an effective regional seal. This finding is based on the existing data coverage and current general knowledge of polygonal faults. As described in Appendix N, the evidence of polygonal faults extending into the Sandpiper Sandstone was inconclusive and the fault density distribution suggests faulting dissipates towards the critical reservoir-seal boundary. It should be noted that across the majority of the Petrel Sub-basin, the polygonal faulting only occurs in the lower section of the Bathurst Island Group and does not extend to the top of the formation. On the shallow margins, there is some evidence of polygonal faulting in the top section of the Bathurst Island Group, although further work is required to define the total extent. The marine surveys conducted as part of this study did not identify any evidence of fluid or hydrocarbon leakage from the deeper formations, which suggests that the Bathurst Island Group is an effective caprock for fluids in the Mesozoic sections.

9 Conclusions

The Petrel Sub-basin is suitable for the geological storage of CO_2. Acquisition of pre-competitive data and a comprehensive analysis of the sub-basin geology identified two Mesozoic reservoir-seal pairs over the central axis and eastern flank of the sub-basin as suitable for CO_2 geological storage. The oldest reservoir-seal pair is the Jurassic reservoir, comprising the Plover and Elang formations and the lower Frigate Shale, and the Jurassic seal comprising the upper Frigate Shale. The younger reservoir-seal pair comprises the Cretaceous Sandpiper Sandstone reservoir and the Cretaceous Bathurst Island Group regional seal. The reservoirs both have sufficient quality and are thick and laterally extensive enough to inject and store CO_2 at a large-scale (multiple MTPA). The Bathurst Island Group seal was determined to be an effective regional seal being both laterally extensive and able to hold back the expected CO_2 column height of the reservoirs below. This study has concluded that the upper Frigate Shale is an effective seal, despite some remaining unknowns regarding its quality and extent.

A geomechanical study of the major tectonic faults in the sub-basin reveals that, under the current stress regime, these do not compromise the integrity of the seals for CO_2 geological storage, with the higher risk faults located on the outer or marginal areas of the sub-basin. Importantly, very high pore pressures (greater than 5 MPa) are required to induce failure the in the faults in the most prospective parts of the sub-basin. Extensive polygonal faulting within the layers of the Bathurst Island Group may compromise the integrity of the lower section of the seal. However, further analysis is needed to fully understand their impact on the seal properties. No compelling link was found between faulting and geochemical or physical evidence of fluid migration or surface leakage, suggesting that the faults do not propagate through the Bathurst Island Group regional seal.

Dynamic reservoir simulations show that migration-assisted trapping is the dominant CO_2 trapping mechanism in both plays, with residual and dissolution trapping mechanisms the dominant process for permanent storage. CO_2 injection reservoir simulations predict that a total of 420 MT of CO_2 can be injected into Jurassic reservoir at a rate of 14 MTPA over 30 years, a rate commensurate with the predicted emissions from the Darwin LNG hub in 2020 by the Carbon Storage Taskforce (2009). A second simulation predicts that an additional total 150 MT of CO_2 can be injected into the Cretaceous reservoir. After 100 years over 50% of the CO_2 is permanently trapped through residual and dissolution processes, and after 1,700 years, over 83% of the total injected CO_2 is trapped. When taking into account the spatial and physical properties of the reservoirs and seals, the combined effective storage capacity of the two reservoirs, using the methodology of Bradshaw et al. (2009), was 15,930 MT (P50 or best estimate).

The combined results of this study were used to assess the reservoir and seal quality throughout the Petrel Sub-basin. This assessment identified an area Highly Suitable for CO_2 storage in the centre of the sub-basin, comprising around 27% of the study area and extending between 50-70 km to the north, east and south of the Petrel gas field. This study of the Petrel Sub-basin adds to the ongoing progress of understanding the CO_2 storage potential of Australia's sedimentary basins and to the development of the CCS industry.

10 Acknowledgements

Firstly, the authors thank Alfredo Chirinos who designed the initial study and for providing mentorship throughout the project. The authors thank Anne Fleming, Leonie Jones, Andrea Cortese, and Morgan Tully for assisting with planning the GA336 seismic survey and also processing of the data collected. Dr Riko Hashimoto, Dr Tony Nicholas, Dr Andrew Carroll are thanked for planning and undertaking the marine survey (SOL5463/GA335). The authors extend thanks to the collaborating researchers that contributed to this study: Jessica Byass, Steven Cadman, Helen Dulfer, Dr George Gibson, Dr Alexey Goncharov, Tim Jones, Jamie Lankford, Rowan Romeyn, Chris Southby, Dr Eric Tenthorey, Christian Thun, Jenny Totterdell, and Dr Liuqi Wang. We also thank Rob Kirk (Rob Kirk Consultants) for undertaking the sequence stratigraphic analysis and interpretation; and Dr Andrew Cavanagh (Statoil) for his assistance with Permedia training and modelling. The authors thank the Master and crew of the RV *Solander*, the scientific staff at AIMS, and the Master and crew of the MV *Duke* for their assistance in the data collection. The detailed reviews of Dr Andrew Heap, Dr Clinton Foster and Dr Andrew Jones improved an early version of the report. The compilation of the final product was made possible through the product design team at Geoscience Australia, specifically Silvio Mezzomo and David Arnold for graphic design and Murray Woods for GIS expertise.

Also, in recognition of their contributing reports, the authors acknowledge:

- Fluid Inclusion Technologies Inc., for the bulk volatile chemistry from fluid inclusions (FIS) studies (Appendix D).
- Dr Joseph Hamilton (Lithicon), for conducting mineral mapping and petrographic analysis (Appendix E).
- Dr Sasha Pontual (AusSpec International), for HyLogger interpretation (Appendix F).
- Dr Yildiray Cinar (University of New South Wales), for conducting core tests for porosity, permeability and seal capacity analysis (Appendix G).
- Dr Graham Yielding (Badley Geoscience Ltd) and Dr Pete Boult (Badley Geoscience Ltd and Gingko ENP GNG) for the fault seal and fault reactivation study (Appendix I).
- Alison Hortle (CSIRO), for the hydrodynamic study (Appendix J).
- Gardline CGG Pte Ltd for the acquisition of GA336, Fugro Seismic Imaging Pty for processing, depth-conversion and post-migration processing (Appendix M) and Jahan Zeb Ahmed (Jason, a CGG company) for 2D simultaneous inversion (Appendix M).
- Dr Andy Nicol and Hannu Seebeck (GNS Science), for completing the polygonal fault study (Appendix N).

11 References

Australian Geological Survey Organisation (AGSO) North West Shelf Study Group, 1994. Deep reflections on the North West Shelf: Changing perceptions of basin formation. In: Purcell, P.G. and Purcell, R.R. (Editors), The sedimentary basins of Western Australia 2: Proceedings of the Petroleum Exploration Society of Australia Symposium, Perth, 63-76.

Bachu, S., Bonijoly, D., Bradshaw, J., Burruss, R., Holloway, S., Christensen, N.P. and Mathiassen, O.M., 2007. CO_2 storage capacity estimation: Methodology and gaps. International Journal of Greenhouse Gas Control, 1(4), 430-443.

Baldwin, S., White, N. and Mueller, R.D., 2003. Resolving multiple rift phases by strain-rate inversion in the Petrel Sub-basin, northwest Australia. Geological Society of America, Special Paper 372, 245-263.

Ballie, P.W., Powell, C.M., LI, Z.X. and Ryall, A.M., 1994. The tectonic framework of western Australia's Neoproterozoic to Recent sedimentary basins. In: Purcell, P.G. and Purcell, R.R. (Editors), The Sedimentary Basins of Western Australia 2: Proceedings of the Petroleum Exploration Society of Australia Symposium, Perth, 45–62.

Barrett, A.G., Hinde, A.L. and Kennard, J.M., 2003. Undiscovered resource assessment methodologies and application to the Bonaparte Basin. In: Ellis, G.K., Baillie, P.W. and Munson, T.J. (Editors), Timor Sea Petroleum Geoscience, Proceedings of the Timor Sea Symposium, Darwin. Northern Territory Geological Survey, Special Publication 1, 353–372.

Berndt, C., Jacobs, C., Evans, A., Gay, A., Elliot, G., Long, D. and Hitchen, K., 2012. Kilometre-scale polygonal seabed depressions in the Hatton Basin, NE Atlantic Ocean: constraints on the origin of polygonal faulting. Marine Geology, 332-334, 126-133.

Blevin, J.E., Colwell, J.B., Kennard, J.M., Edwards, D.S., Jones, P.J. and Nicoll, R.S., 1996a. Definition of basin phases in the Petrel Sub-basin (Australia); implications for the development of Palaeozoic petroleum systems. Annual Meeting Abstracts - American Association of Petroleum Geologists and Society of Economic Paleontologists and Mineralogists, 5, 16.

Blevin, J.E., Colwell, J.B., Edwards, D.S., Foster, C.B., Jones, P.J., Kennard, J.M., Nicoll, R.S., O'Brien, G.W., Shergold, J.H., Summons, R.E. and Wilson, D.J., 1996b. Integrated studies of the Petrel Sub-basin (Bonaparte Basin), defining the Palaeozoic foundations of the North West Shelf. Abstracts - Geological Society of Australia, 41, 39.

Borel, G.D. and Stampfli, G.M., 2002. Geohistory of the North West Shelf: a tool to assess the Palaeozoic and Mesozoic motion of the Australian Plate. In: Keep, M. and Moss, S. (Editors), The Sedimentary Basins of Western Australia 3: Proceedings of the Petroleum Exploration Society of Australia Symposium, Perth, 119-128.

Bourget, J., Ainsworth, R.B., Backé, G. and Keep, M., 2012. Tectonic evolution of the northern Bonaparte Basin: impact on continental shelf architecture and sediment distribution during the Pleistocene. Australian Journal of Earth Sciences, 59(6), 877-897.

Bradshaw, B.E., Spencer, L.K., Lahtinen, A.C., Khider, K., Ryan, D.J., Colwell, J.B., Chirinos, A. and Bradshaw, J., 2009. Queensland carbon dioxide geological storage atlas. Report by Greenhouse Gas Storage Solutions on behalf of Queensland Department of Employment, Economic Development and Innovation, 311 pp.

Bradshaw, J., Bradshaw, B.E., Spencer, L. and Mackie, V., 2000. GEODISC: Project 1—Regional Analysis Stage 2 Basins, Version 2.02., Australian Geological Survey Organisation (AGSO), Department of Industry, Science and Resources, Canberra.

Bradshaw, J. and Rigg, A., 2001. The GEODISC Program: Research into Geological Sequestration of CO_2 in Australia. Environmental Geosciences, 8(3), 166-176.

Bradshaw, J., Sayers, J., Bradshaw, M., Kneale, R., Ford, C., Spencer, L. and Lisk, M., 1998. Palaeogeography and its impact on the petroleum systems of the North West Shelf, Australia. In: Purcell, P.G. and Purcell, R.R. (Editors), The Sedimentary Basins of Western Australia 2: Proceedings of the Petroleum Exploration Society of Australia Symposium, Perth, 95-121.

Bunch, M.A., 2013. Gauging geological characterisation for CO_2 storage: the Australasian experience so far…. Australian Journal of Earth Sciences, 60, 5-21.

Burbidge, D.R. (Editor), 2012. The 2012 Australian Earthquake Hazard Map. Geoscience Australia Record 2012/71. Geoscience Australia, Canberra.

Cadman, S.J. and Temple, P.R., 2004. Bonaparte Basin, NT, WA, AC and JPDA, Australian Petroleum Accumulations Report 5, 2nd Edition, Geoscience Australia, Canberra.

Carbon Sequestration Leadership Forum, 2011. Carbon Sequestration Leadership Forum Technology Roadmap, 2011, 115 pp.

Carbon Storage Taskforce, 2009. National Carbon Mapping and Infrastructure Plan – Australia: Full Report, Department of Resources, Energy and Tourism, Canberra.

Carroll, A.G., Jorgensen, D.C., Siwabessy, P.J.W., Jones, L.E.A., Sexton, M.J., Tran, M., Nicholas, W.A., Radke, L.C., Carey, M.P., Howard, F.J.F., Stowar, M.J., Heyward, A.J., Potter, A. and Shipboard Party, 2012. Seabed environments and shallow geology of the Petrel Sub-Basin, northern Australia: SOL5463 (GA0335) - post survey report, Geoscience Australia Record 2012/66, Canberra.

Cartwright, J., 2011. Diagenetically induced shear failure of fine-grained sediments and the development of polygonal fault systems. Marine and Petroleum Geology, 28(9), 1593-1610.

Cartwright, J.A. and Dewhurst, D.N., 1998. Layer-bound compaction faults in fine-grained sediments. Geological Society of America Bulletin, 110(10), 1242-1257.

Cartwright, J.A., James, D. and Bolton, A., 2003. The genesis of polygonal fault systems. In: P. Van Rensbergen, R.R. Hillis, A.J. Maltman and C.K. Morley (Editors), Subsurface sediment mobilization. Geological Society of London, Special Publications, 216, 223-243.

Cartwright, J.A. and Lonergan, L., 1996. Volumetric contraction during the compaction of mudrocks: A mechanism for the development of regional scale polygonal fault systems. Basin Research, 8, 183-193.

Clark, D., McPherson, A. and Collins, C.D.N. 2011. Australia's seismogenic neotectonic record: a case for heterogeneous intraplate deformation. Geoscience Australia Record 2011/11, Canberra.

CO2CRC, 2008. Storage capacity estimation, site selection and characterization for CO_2 storage projects. Cooperative Research Centre for Greenhouse Gas Technologies (CO2CRC), CO2CRC Report RPT08-1001, CO2CRC, Canberra.

Colwell, J.B. and Kennard, J.M. (Compilers), 1996. Petrel Sub-basin Study 1995-1996: Summary Report. Australian Geological Survey Organisation Record 1996/40, Canberra, 122 pp.

Cook, P. J. 2012. Clean Energy, Climate and Carbon. CSIRO Publishing, Melbourne, Australia, 215 pp.

Cook, P.J., Rigg, A. and Bradshaw, J., 2000. Putting it back where it came from; is geological disposal of carbon dioxide an option for Australia? The APPEA Journal, 40(1), 654-666.

Department of Energy (DOE), 2007. Appendix A: Methodology for development of carbon sequestration capacity estimates, Carbon Sequestration Atlas of the United States and Canada. U.S. Department of Energy, National Energy Technology Laboratory, 71-86.

Frankowicz, E. and McClay, K.R., 2010. Extenional fault segmentation and linkages, Bonaparte Basin outer North West Shelf Australia. AAPG Bulletin, 94(7), 977-1010.

Gay, A., Lopez, M., Cochonat, P. and Sermondadaz, G., 2004. Polygonal faults-furrows system related to early stages of compaction - upper Miocene to recent sediments of the Lower Congo Basin. Basin Research, 16, 101-116.

Gibson-Poole, C.M., 2009. Site Characterisation for Geological Storage of Carbon Dioxide: Examples of Potential Sites from the North West Shelf, Australia, PhD Thesis, University of Adelaide, Adelaide, Australia.

Gibson-Poole, C.M., Lang, S.C., Streit, J.E., Kraishan, G.M. and Hillis, R.R., 2002. Assessing a basin's potential for geological sequestration of carbon dioxide; an example from the Mesozoic of the Petrel Sub-basin, NW Australia. In: Keep, M. and Moss, S. (Editors), The Sedimentary Basins of Western Australia 3: Proceedings of the Petroleum Exploration Society of Australia Symposium, Perth, 439-463.

Global CCS Institute, 2013. The Global Status of CCS: 2013, Melbourne, Australia.

Goncharov, A.G., Collins, C.D.N., Petkovic, P. and Fomin, T.N., 1999. Seismic velocities in the Petrel Sub-basin from the ocean-bottom seismograph studies: implications for crustal structure and petroleum prospecting. The APPEA Journal, 39(1), 729-730.

Gorter, J.D., Nicoll, R.S., Metcalfe, I., Willink, R.J. and Ferdinando, D., 2009. The Permian–Triassic boundary in Western Australia: evidence from the Bonaparte and northern Perth basins: exploration implications. The APPEA Journal, 49, 311–336.

Gorter, J.D.1998. Revised Upper Permian stratigraphy of the Bonaparte basin. In: Purcell, P.G. and Purcell, R.R. (Editors), The Sedimentary Basins of Western Australia 2: Proceedings of the Petroleum Exploration Society of Australia Symposium, Perth, 213–228

Gradstein, F.M., Ogg, J.G., Schmitz, M.D. and Ogg, G.M.e., 2012. The Geologic Time Scale 2012, 1 and 2, 1144 pp.

Gunn, P., 1988. Bonaparte rift basin: effects of axial doming and crustal spreading. Exploration Geophysics, 19(2), 83-87.

Heidbach, O., Tingay, M., Barth, A., Reinecker, J., Kurfeß, D. and Müller, B., 2009. The World Stress Map based on the database release 2008, equatorial scale 1:46,000,000, Commission for the Geological Map of the World, Paris, doi:10.1594/GFZ.WSM.Map2009.

Hillis, R.R. and Reynolds, S.D., 2000. The Australian stress map. Journal of Geological Society of London, 157(5), 915-921.

Holloway, S., 2007. Carbon dioxide capture and geological storage. Philosophical Transactions of the Royal Society A: Mathematical, Physical and Engineering Sciences, 365(1853), 1095-1107.

Holtz, H.M., 2002. Residual Gas Saturation to Aquifer Influx: A Calculation Method for 3-D Computer Reservoir Model Construction. Paper SPE 75502, presented at SPE Gas Technology Symposium, Calgary, Canada.

IPCC, 2005. IPCC Special Report on Carbon Dioxide Capture and Storage. Prepared by Working Group III of the Intergovernmental Panel on Climate Change [Metz, B., O. Davidson, H. C. de Coninck, M. Loos, and L. A. Meyer (eds.)]. Cambridge University Press, Cambridge, United Kingdom and New York, NY, USA, 442 pp.

Johnston, S. and Goncharov, A., 2012. Velocity Analysis and Depth Conversion in the Offshore Northern Perth Basin, Australia. Geoscience Australia Record, 2012/33, Geoscience Australia, Canberra.

Kaldi, J., Daniel, R., Tenthorey, E., Michael, K., Schacht, U., Nicol, A., Underschultz, J. and Backe, G., 2013. Containment of CO_2 in CCS: Role of Caprocks and Faults. Energy Procedia, 37, 5403-5410.

Keep, M., Clough, M. and Lenghi, L., 2002. Neogene tectonic and structural evolution of the Timor Sea region, NW Australia. In: Keep, M. and Moss, S. (Editors), The Sedimentary Basins of Western Australia 3: Proceedings of the Petroleum Exploration Society of Australia Symposium, Perth, 341-353.

Kennard, J.M., Deighton, I., Edwards, D.S., Boreham, C.J. and Barrett, A.G., 2002. Subsidence and thermal history modeling: new insights into hydrocarbon expulsion from multiple petroleum systems in the Petrel Sub-basin, Bonaparte Basin. In: Keep, M. and Moss, S. (Editors), The Sedimentary Basins of Western Australia 3: Proceedings of the Petroleum Exploration Society of Australia Symposium, Perth, 409-437.

Lang, S.C. and Gibson-Poole, C.M., 2001. Geological Model – Petrel Sub-basin, North West Australia. GEODISC Project, Site Specific Studies for Geological Disposal of Carbon Dioxide. GEODISC2-2001-001, National Centre for Petroleum Geology and Geophysics (NCPGG) and Australian Petroleum Cooperative Research Centre (APCRC), University of Adelaide, Adelaide, Australia.

Laurent, D., Gay, A., Baudon, C., Berndt, C., Soliva, R., Planke, S., Mourgues, R., Lacaze, S., Pauget, F., Mangue, M. and Lopez, M., 2012. High-resolution architecture of a polygonal fault interval inferred from geomodel applied to 3D seismic data from the Gjallar Ridge, Voring Basin, Offshore Norway. Marine Geology, 332-334, 134-151.

Lee, R. and Gunn, P., 1988. Bonaparte Basin. Petroleum in Australia: The First Century. The APEA Journal, 28(1), 252–269.

Lemon, N.M. and Barnes, C.R., 1997. Salt migration and subtle structures: modelling of the Petrel Sub-basin, northwest Australia. The APPEA Journal, 37(1), 245-258.

Lonergan, L., Cartwright, J. and Jolly, R., 1998. The geometry of polygonal fault systems in Tertiary mudrocks of the North Sea. Journal of Structural Geology, 20(5), 529-548.

Longley, I.M., Buessenschuett, C., Clydsdale, L., Cubitt, C.J., Davis, R.C., Johnson, M.K., Marshall, N.M., Murray, A.P., Somerville, R. and Spry, T.B., 2002. The North West shelf of Australia–a Woodside perspective. In: Keep, M. and Moss, S. (Editors), The Sedimentary Basins of Western Australia 3: Proceedings of the Petroleum Exploration Society of Australia Symposium, Perth, 27-88.

Loutit, T.S., Summons, R.E., Bradshaw, M.T. and Bradshaw, J., 1996. Petroleum systems of the North West Shelf, Australia – how many are there?, Establishing Indonesia's Sustainable Growth in the Energy Industry: Proceedings of the Indonesian Petroleum Association's Twenty-fifth Silver Anniversary Convention, Jakarta, Indonesia, 437-452.

McConachie, B.A., Bradshaw, M.T. and Bradshaw, J., 1996. Petroleum systems of the Petrel Sub-basin; an integrated approach to basin analysis and identification of hydrocarbon exploration opportunities. The APPEA Journal, 36(1), 248-268.

Messent, B.E.J., Goody, A.K., Collins, E. and Tobias, S., 1994. Sequence stratigraphy of the Flamingo Group, southern Bonaparte Basin. In: Purcell, P.G. and Purcell, R.R. (Editors), The Sedimentary Basins of Western Australia 2: Proceedings of the Petroleum Exploration Society of Australia Symposium, Perth, 243-257.

Mildren, S.D., Hillis, R.R. and Jones, R.M., 2000. Contemporary stress orientation and structural permeability in the Petrel Sub-basin. AAPG Bulletin, 84(9), 1465.

Miyazaki, S., 1997. Australia's southeastern Bonaparte Basin has plenty of potential. Oil and Gas Journal, 95(16), 78-81.

Mory, A. J., 1988. Regional geology of the offshore Bonaparte Basin. In: Purcell, P.G. and Purcell, R.R. (Editors), The North West Shelf Australia: Proceedings of the Petroleum Exploration Society of Australia Symposium, Perth, p. 287-309.

Mory, A.J., 1990. Bonaparte Basin. In: Geology and mineral resources of Western Australia. Geological Survey of Western Australia, Memoir 3, Western Australia, p. 380-415.

Mory, A.J., 1991. Geology of the offshore Bonaparte Basin, northwestern Australia. Geological Survey of Western Australia, Report 29, 47 pp.

Mory, A. and Beere, G.M., 1988. Geology of the onshore Bonaparte and Ord Basins. Geological Survey of Western Australia Bulletin, 134 pp.

Nicol, A., Walsh, J.J., Watterson, J., Nell, P.A.R. and Bretan, P., 2003. The geometry, growth and linkage of faults within a polygonal fault system from South Australia. Geological Society, London, Special Publications, 216(1), 245-261.

Nicoll, R.S., Kennard, J.M., Laurie, J.R., Kelman, A.P., Mantle, D.J. and Edwards, D.S., 2009. Bonaparte Basin Biozonation and Stratigraphy: Chart 33, Geoscience Australia, Canberra.

O'Brien, G.W., 1993. Some ideas on the rifting history of the Timor Sea from the integration of deep crustal seismic and other data. The PESA Journal, 21, 95-113.

O'Brien, G.W., Blevin, J., Gunn, P., Romine, K., Scott, D.L., Willcox, J.B. and Baldwin, S., 1995. The Petrel sub-basin system, Timor Sea, Australia; rift architecture and its control on structuring within the Mesozoic and Tertiary sequence, Timor Sea. Annual Meeting Abstracts - American Association of Petroleum Geologists and Society of Economic Paleontologists and Mineralogists, 4, 72.

Pattilo, J. and Nicholls, P.J., 1990. A tectonostratigraphic framework for the Vulcan Graben, Timor Sea region. The APEA Journal, 30(1), 27-51.

Rigg, A.J., Allinson, G., Bradshaw, J., Ennis-King, J., Gibson-Poole, C.M., Hillis, R.R., Lang, S.C. and Streit, J.E., 2001. The search for sites for geological sequestration of CO_2 in Australia; a progress report on GEODISC. The APPEA Journal, 41(1), 711-725.

Szulczewski, M.L., MacMinn, C.W., Herzog, H.J. and Juanes, R., 2012. Lifetime of carbon capture and storage as a climate-change mitigation technology. Proceedings of the National Academy of Sciences, 109(14), 5185-5189.

Veevers, J.J., 1988. Morphotectonics of Australia's Northwestern margin - a review. In: Purcell, P.G. and Purcell, R.R. (Editors), The North West Shelf Australia: Proceedings of the Petroleum Exploration Society of Australia Symposium, Perth, 19–27

Watterson, J., Walsh, J., Nicol, A., Nell, P.A.R. and Bretan, P.G., 2000. Geometry and origin of a polygonal fault system. Journal of the Geological Society, 157(1), 151-162.

Whittam, D.B., Norvick, M.S. and Mcintyre, C.L., 1996. Mesozoic and Cenozoic tectonostratigraphy of western ZOCA and adjacent areas. The APPEA Journal, 36(1), 209-231.

Zhixin, W., Guanghui, Z., Lin'an, P. and Wenlian, T., 2012. An oil and gas resource reassessment of the Bonaparte Basin, northwest shelf of Australia. Bulletin of Canadian Petroleum Geology, 60(3), 218-226.

The following appendices and supplementary report are available on the Geoscience Australia website at: http://www.ga.gov.au/metadata-gateway/metadata/record/76510

- **Appendix A** Seismic and well interpretation of the Petrel Sub-basin
- **Appendix B** Petrophysical analysis of potential Mesozoic-Cenozoic CO_2 storage reservoirs of the Petrel Sub-basin
- **Appendix C** Mesozoic-Cenozoic sedimentology, stratigraphy and depositional environments of the Petrel Sub-basin
- **Appendix D** Stratigraphic reconstruction of bulk volatile chemistry from fluid inclusions in Bougainville 1, Penguin 1, Flat Top 1, Newby 1
- **Appendix E** Automated mineral analysis by SEM/EDS of sixty samples supplied from Geoscience Australia
- **Appendix F** Interpretation and analysis of HyLogging data from Gull 1 and Petrel 1
- **Appendix G** Core analysis results of Petrel 1, Jacaranda 1, Gull 1 and Tern 1, Petrel Sub-basin
- **Appendix H** Mesozoic–Cenozoic structural geology of the Petrel Sub-basin
- **Appendix I** Fault-seal risk, Petrel Sub-basin
- **Appendix J** Petrel Sub-basin hydrodynamic assessment
- **Appendix K** 3D static geological modelling of the Petrel Sub-basin
- **Appendix L** Numerical reservoir simulation of geological storage of CO_2 in the Petrel Sub-basin
- **Appendix M** GA336 seismic survey reports including acquisition, processing, post-stack depth migration and simultaneous inversion reports
- **Appendix N** Polygonal faulting in the Bonaparte Basin: Implications for seal integrity and subsurface storage of carbon dioxide
- **Appendix O** CO_2 geological storage capacity and injectivity in the Petrel Sub-basin
- **Supplementary Report 1** Petrel Sub-basin well composite and well correlations folio